6-30-2016

Numerical Modeling Of Heat Transfer And Material Flow During Friction Extrusion Process

Hongsheng Zhang
University of South Carolina

NUMERICAL MODELING OF HEAT TRANSFER AND MATERIAL FLOW DURING FRICTION EXTRUSION PROCESS

by

Hongsheng Zhang

Bachelor of Science
Wuhan University of Technology, 2007

Master of Science
Wuhan University of Technology, 2010

Submitted in Partial Fulfillment of the Requirements

For the Degree of Doctor of Philosophy in

Mechanical Engineering

College of Engineering and Computing

University of South Carolina

2016

Accepted by:

Xiaomin Deng, Major Professor

Anthony P. Reynolds, Committee Member

Michael A. Sutton, Committee Member

Enrica Viparelli, Committee Member

Lacy Ford, Senior Vice Provost and Dean of Graduate Studies

ACKNOWLEDGEMENTS

I would like to express my deepest gratitude to my advisor, Prof. Xiaomin Deng, for his guidance, support, encouragement, and patience throughout my study at the University of South Carolina. I am very grateful to Prof. Michael Sutton for his valuable suggestions and comments. I would also like to thank Prof. Tony Reynolds for helpful discussions and suggestions, and Prof. Enrica Viparelli for her interest and comments.

Special thanks to Prof. Zhangmu Miao, my advisor for my master's degree, who encouraged me to pursue the Ph.D. degree.

I am thankful to Dr. Wei Tang, Mr. Xiao Li, and Mr. Dan Wilhelm for providing experimental data to me and for their discussions about the experiments. I would like to thank Mr. Xiaochang Leng and Mr. Nasser Abbas for discussions and comments. I also thank many other friends at the University of South Carolina for their friendship.

Many thanks to my parents and my sister for their support and love.

I gratefully acknowledge the financial support provided in part by NSF (NSF-CMMI-1266043), by NASA (Consortium Agreement NNX10AN36A), and by a SPARC Graduate Fellowship from the Office of the Vice President for Research at the University of South Carolina.

ABSTRACT

Friction extrusion process is a novel manufacturing process that converts low-cost metal precursors (e.g. powders and machining chips) into high-value wires with potential applications in 3D printing of metallic products. However, there is little existing scientific literature involving friction extrusion process until recently. The present work is to study the heat transfer and material flow phenomena during the friction extrusion process on aluminum alloy 6061 through numerical models validated by experimental measurements.

The first part is a study of a simplified process in which flow of a transparent Newtonian fluid in a cylindrical chamber caused by frictional contact with a rotating die is considered but extrusion is omitted. This simplified process facilitates an analytical solution of the flow field and experimental visualization and measurements of the flow field in the chamber. The fluid choice and rotation speed are chosen so that the Reynolds number of the flow is approximately the same as that in the friction extrusion process of an aluminum alloy and that the resulting fluid flow is a laminar flow. An analytical solution for the velocity field of the fluid flow has been obtained, and the process has also been simulated using fluid dynamics. The analytical solution, the numerical predictions, and experimental measurements have been compared and good agreements can be observed.

Second, a pure thermal model has been developed to investigate the heat transfer during the friction extrusion process. A volume heating model is proposed to approximate the heat generation. A layer under the interface between the die and the aluminum alloy sample is chosen as the heat source zone. The distribution of the heat generation rate is

assumed linear along both vertical and radial directions. The total power input into the system is related to the mechanical power recorded in the friction extrusion experiment. Only heat transfer is considered in this model and the material flow is neglected. The temperature predictions have a good agreement with experimental measurements, indicating that the proposed model can capture the heat transfer phenomenon.

A three-dimensional thermo-fluid model also has been developed to provide a comprehensive understanding of the friction extrusion process. Both heat transfer and material flow are simulated. The volume heat model in the pure thermal model is utilized for the heat generation. The predicted temperature results show that the material flow has limited influence on heat transfer. The sample is treated as a non-Newtonian fluid whose viscosity is temperature and strain rate dependent. Massless solid particles are used in the fluid as tracers to study the material flow patterns. The predicted distribution of the particles on extruded wire cross sections compare qualitatively with experimental measurements, suggesting that the material flow can be captured by the thermo-fluid model. The model provides predictions, such as the fields of velocity, strain rate, and viscosity which are not available from experimental measurements. The particle path lines also show how the material flows to form the wire.

TABLE OF CONTENTS

LIST OF FIGURES

CHAPTER 1 INTRODUCTION

1.1 Background

There are many manufacturing processes and the main ones include casting, molding, forming, machining, joining, additive manufacturing, and others. Usually many processes are used to produce parts and shapes. Of these processes, machining is used very frequently because of irregular shapes of parts. Nowadays, there is no doubt that the use of metals is wide and the amount is increasing, especially in aerospace and shipbuilding industries, as well as in the automobile industry, because of the excellent mechanical performance of metals. At the same time, the amount of metal wastes left during manufacturing processes, such as machining chips, scraps, and small blocks, is substantially huge. For some industries, such as the aerospace industry, load-bearing structures have always been fabricated from high performance materials because of the requirement of high quality and reliability. As we know, higher performance often means more costs. Since high performance materials are expensive, those manufacturing processes that produce less metal wastes or that can convert metal wastes into useful products become crucial to many industries. As is known, in the manufacturing industry, people have never stopped exploring new manufacturing methods to produce high performance products with lower costs at the same time. Friction extrusion process is such a novel manufacturing process that can convert low-cost metal precursors (e.g. powders and machining chips) into high-value wires which have many applications. It has great potential to meet the needs for low costs and high performance for the aerospace industry.

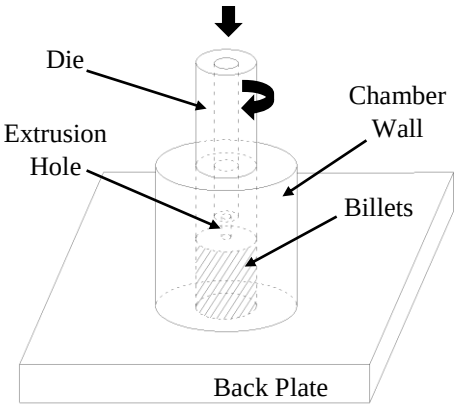

Figure 1.1 A schematic diagram of the friction extrusion process.

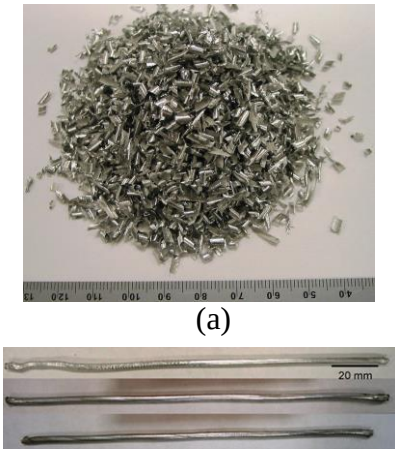

(a)

(b)

Figure 1.2 (a) Milled Chips, (b) Wires [3].

Friction extrusion process was invented and patented at the Welding Institute (Cambridge, UK) in the 1993 [1] and but the patent lapsed in 2002 [2]. So far, it hasn't been well studied. A schematic diagram of the friction extrusion process is shown in Figure 1.1. Friction extrusion process uses low-cost precursors, such as machining chips, or metal powders to produce wires. The precursor material is installed in a cylindrical chamber which is put on a back plate. The chamber is a hollow cylinder made with a tool steel. Since the precursor is loose it needs to be compressed first. A die with a small hole in the center moves down and exerts a vertical force to compress the precursor material in the chamber. Then the die begins to rotate to stir the precursor material, and heat will be generated by the friction between the die and the precursor at the die-precursor interface. The continued frictional heat generation will cause temperature rise in the precursor material. As a result, the precursor material first becomes softened. Under high pressure in the chamber caused by the vertical load from the die and strong stirring motion due to rotation of the die, the softened material, i.e. the precursor material near the die-precursor interface, experiences

severe deformation and finally flows out through the extrusion hole to form a solid wire. Figure 1.2 shows aluminum alloy 6061 machining chips and extruded wires [3].

During the friction extrusion process, the precursor material is converted into a wire or rod without melting. Thus friction extrusion is a friction based process and the friction induces heat generation. In the friction extrusion process, heat generation comes from two parts. One is from the frictional heating at the die-precursor interface. When the die rotates, heat will be generated from the friction between the die and the precursor at the die-precursor interface. The continued frictional heat generation will result in an increasing amount of heat which is absorbed by the precursor material and the die, causing temperature rise and subsequently decrease of the material's flow stress. At first, since heat generation occurs at the die-precursor interface, the temperature near that interface is high and heat transfers outward. Because of the increasing temperature, the precursor material gets softened and becomes easy to flow. On the one hand, some material sticks to the die interface and rotates with the die. Part of the softened material under the die-precursor interface flows out from the extrusion hole to form a wire. Thus, severe plastic deformation occurs in the precursor material and at the same time, heat will be generated due to plastic dissipation. This is the other heat generation source. Before being extruded out to form a wire, the precursor material in the chamber experiences strong distortions and high temperature.

The friction extrusion process represents a step forward in recycling of metal wastes, such as metal chips, scraps, and small blocks produced during manufacturing. In general, there are two types of recycling methods for metal wastes, which are conventional recycling and direct recycling. Conventional recycling methods have several steps and

involve melting to recover the metal. In contrast, direct recycling do not involve melting of metal. In comparison, direct recycling methods have some advantages, such as less material loss due to absence of melting, lower energy consumption and thus more environmentally friendly, and considerable labor savings. Taking aluminum alloy recycling for example, direct recycling can save about 40% of material, 26-31% of energy consumption, and 16-60% of labor costs [4]. The friction extrusion process falls into the category of direct recycling methods and it has all the advantages.

Figure 1.3 Parts produced by the wire and arc additive manufacturing process [5].

Another potential of the friction extrusion process is its possible contribution to additive manufacturing. The friction extrusion process has a great potential to provide high value wire feedstock at lower costs for a breakthrough technology in recent years, the additive manufacturing. Additive manufacturing is an innovative method to produce parts in a fast, flexible and cost-efficient way from 3D CAD data. The material supply is usually powder or wire [5]. There are additive manufacturing processes that uses wire feedstock, such as the Electron Beam Free Fabrication (EBF3) and Wire and Arc Additive Manufacturing (WAAM). The EBF3 is being used to manufacture titanium parts for F-35 Joint Strike Fighter [6]. Figure 1.3 shows some parts produced by the wire and arc additive manufacturing process [5]. Both of them have shown promising potentials in the aerospace

industry. The additive manufacturing processes consume substantial amount of wires to build parts and thus the costs of the wire becomes crucial. As such, the availability of low-cost wires with custom composition becomes critical. Friction extrusion process can meet this need as an innovative and economical material processing method as it directly converts metal wastes to wires without an intervening melting step and it can produce wires with custom composition.

Compared with the traditional extrusion manufacturing, the friction extrusion process has some outstanding advantages. First, the material used for friction extrusion process can be metal blocks and metal wastes or metal powders. So the wires produced by friction extrusion have lower costs for raw materials. Second, since heat is generated during friction extrusion, pre-heating is not necessary and it makes friction extrusion process more environmentally friendly. Third, the force needed in the friction extrusion process is not as high, and the equipment needed is not as complicated.

1.2 Research Objectives

The current dissertation is focused on investigating the friction extrusion process by developing numerical models to understand the heat transfer and material flow phenomena during the process. The study includes mainly three parts, the visualization study, the heat transfer simulation, and the thermo-fluid modeling of friction extrusion process. The numerical models are validated by comparing numerical predictions with experimental measurements.

Since there is little existing scientific literature involving the friction extrusion process, this work is trying to gain some understanding of the physical phenomena involved during the friction extrusion process. The purpose of the visualization study is to

use transparent tools and a transparent fluid to allow visualization of material flow. Analytical solutions and numerical solutions are developed for a simplified model which include a rotating die and a Newton fluid in a chamber. The analytical solution and the numerical predictions are validated by comparisons with experimental measurements.

Next the heat transfer phenomenon in friction extrusion is studied by a pure thermal model. A volume heating model has been proposed to approximate the heat generation and a layer under the interface between the die and the sample is chosen as the heat source zone. This model is to predict the temperature field within the process chamber that is not available from experimental measurements and to provide a thermal model for more complicated process models, such as the subsequent thermo-fluid model. This model is also utilized to determine the proper thermal boundary conditions.

In order to provide a comprehensive understanding of the friction extrusion process, a three-dimensional thermo-fluid model has been proposed. The thermo-fluid model includes both heat transfer and material flow. The volume heating model is used for the heat transfer and the precursor is treated as a highly viscous non-Newtonian fluid. This model is to verify that the assumption made in the pure thermal model, namely that material flow has limited influence on heat transfer by comparing the temperature predictions with those from the pure thermal model. The thermo-fluid model provides an understanding of the flow fields, such as the velocity field, the strain rate field, and the viscosity field, which are not available from the experimental studies. It also provides an understanding of the material flow pattern and how the material flows out of the extrusion hole to form an extruded wire.

1.3 Outline of the Dissertation

There are seven chapters in the present dissertation. The remaining chapters are arranged as follows.

Chapter 2 describes the friction extrusion experimental procedure and the tools used. Data from a series of experiments are available but only the ones that show good quality wires are used to provide the experimental data for numerical modeling in the current work.

Chapter 3 reviews numerical methods that can be employed to simulate manufacturing processes involving large material deformation under high temperature, such as metal forming, friction stir welding, and friction extrusion. The commonly used numerical methods in manufacturing processes include finite element methods and computational fluid dynamics.

Chapter 4 presents a simplified process model by using a Newton fluid to mimic the material flow during the friction extrusion process. An analytical solution has been developed due to the regularity of the problem. The problem has also been solved numerically by using the CFD method. The analytical solution and the numerical predictions are compared, and their predictions are also compared with velocity measurements from visualization experiments in which transparent process chamber and fluid are used

Chapter 5 develops a pure thermal model to study the heat transfer during friction extrusion. A volume heating model is proposed based on experimental observations and simplifications to approximate the heat generation. The numerical predictions are compared with experimental measurements. Then the temperature field is discussed.

Chapter 6 studies the material flow during the friction extrusion process by using a thermo-fluid model, which includes both heat transfer and material flow. The volume heating model in the pure thermal model is adopted. The aluminum alloy sample is treated as a fluid whose viscosity is strain rate and temperature dependent. Some massless solid particles are used in the fluid as marker to study the material flow patterns. The findings are then presented.

Chapter 7 summarizes the present dissertation, and some recommendations for further study on friction extrusion process are given.

CHAPTER 2 EXPERIMENTAL PROCEDURE

Friction extrusion experiments were conducted at the University of South Carolina. Machining chips and metal blocks of aluminum were tried as precursor material. Experiment parameters include the vertical force applied on the die and the rotation speed of the die. Several combinations of these two parameters were tried and the properties of extruded wires were measured. In this work, for the convenience of comparing experimental measurements with numerical predictions, the friction extrusion experiment with aluminum alloy 6061 block is focused. The following sections will introduce the friction extrusion experiment. The experiments were conducted by my co-worker Mr. Xiao Li.

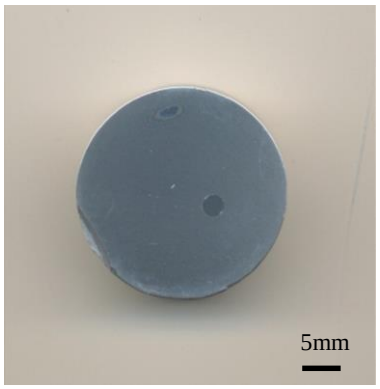

Figure 2.1 An AA 6061 cylinder sample with an AA 2195 wire inserted at 1/3 radius from the center.

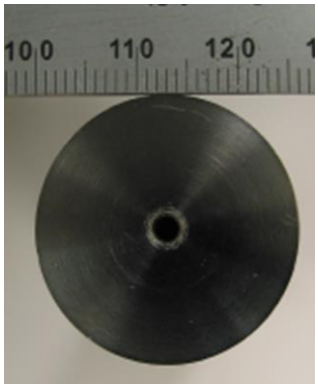

Figure 2.2 A friction extrusion die with a flat tip.

2.1 Extrusion Material and Device

In this work, a cylinder of aluminum alloy 6061 (AA6061) was adopted as the extrusion billet charge. The diameter is 25.5 mm and the length is 19.0 mm. To help with visualizing material flow patterns in friction extrusion process (FEP), a wire of aluminum alloy 2195 (AA2195) with a diameter of 2.54 mm was inserted into the billet charge cylinder as a marker material. The insert was made by drilling a Φ2.54 mm hole through the AA 6061 cylinder at 1/3 radius from the center. A top view of the cylinder is shown in Figure 2.1. Since thermal properties of the two alloys are very similar to each other and the volume fraction of the marker material is small compared to other part of the cylinder, it is believed that inserting the AA 2195 wire into the AA 6061 cylinder will not greatly affect the heat transfer or flow characteristics during friction extrusion.

Figure 2.3 The billet chamber.

The FEP device used in this experiment is composed of the following four parts: a cylindrical die with a flat tip (see Figure 2.2 for a bottom view of the die, where the central hole is the extrusion exit hole), a chamber, a back plate, and a friction stir welding (FSW)

machine used to control the FEP. The dimensions of the extrusion die with a flat tip are Φ25.5 mm × 114.3 mm with a Φ2.54 mm through hole at the center.

The inner and outer diameters of the stationary chamber as shown in Figure 2.3 are 26.4 mm and 54.6 mm, respectively, and the height of the chamber is 29.2 mm. The chamber also has a 70.0 mm diameter shoulder with two semicircle breaches for convenience of clamping and location. The die and chamber are made of H13 and O1 tool steels respectively.

The FSW process development system (PDS) at the University of South Carolina was used to control the die movement in the extrusion process, and the Z-axis load control mode was adopted in the operation. At the initial stage, the entire extrusion process occurred under a constant Z-axis load but the extrusion rate and die advancing rate varied during the process. A stainless steel plate was used as the back plate to support the chamber and the cylinder sample. In order to prevent slipping between the back plate and the billet charge, a 4 mm-height small pin was set on the back plate inside the chamber area as shown in Figure 2.4.

2.2 Thermocouple Locations and Temperature Measurement

To provide experimental measurements for numerical simulations, measurements of temperature variations with time were made at representative points during friction extrusion. K-type thermocouples were used at eight locations on the die and in the chamber wall and back plate. It is noted that placement of thermocouples inside the chamber is not possible since it will interfere the friction extrusion process and damage the thermocouples.

The locations of the thermocouples are shown in Figure 2.4. In particular, two thermocouples were placed on the tool die. One was attached on the outside wall of middle

part of the die (point 1), 54.7 mm away from the die extruding surface (the die tip surface). The other one was embedded inside the die which was at 1.27mm away from the die extruding surface (point 2). Three thermocouples were placed on the outer surface of the chamber wall. They were located at the top of the chamber, the corner of the chamber shoulder and the bottom of the chamber, respectively (points 3, 4, and 5). Close to the chamber inner wall, two thermocouples were placed at 18 mm (point 6) and 15.5 mm (point 7) away from the back plate, respectively. Corresponding to the center of the extrusion chamber, a thermocouple was put in the back plate and at 2.35 mm away from the top surface (point 8). Temperatures at points 1 and 2 were recorded using a HOBOware Data logger with a 1 Hz collecting rate, and temperatures at the rest of the locations were recorded using the Labview software on a PC with 2.4 Hz frequency.

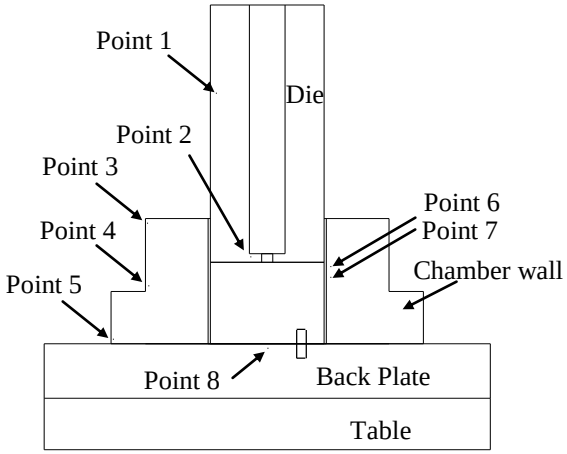

Figure 2.4 Thermocouple locations.

2.3 Experimental Procedure

The extrusion process was carried out as follows. First the die was moved above the chamber which contained the aluminum alloy sample. The Z-axis of the machine was coincident with the extrusion axis, so that the Z-force is the extrusion force. Then the die

was moved downward until its tip was in contact with the sample. Then the Z-force was increased to about 2,225 N to ensure full contact between the die tip and the sample. After that, the die was let to rotate until it reached a desired speed of 300 rpm; synchronously, the Z-force was increased to 44,500 N.

The heat generated by the friction between the die and sample caused the temperature increased immediately. As a result, the sample material close to the die tip became softened. At first, with the downward pressure and frictional heating, the softened sample material flowed into the small gap (~0.5 mm) between the sample and the chamber wall. In the current die design, due to the length of die and hence of the extrusion hole, when the extruded material filled the entire hole and reached the confined chuck, the friction extrusion process ended and an aluminum wire of about 160 mm in length was produced.

During the entire friction extrusion process, several process variables, including the rotation speed, die position, Z-force (extrusion force), rotating torque and power, were recorded by the FSW system control computer with a 10 Hz sampling rate. These data will provide boundary conditions for the die and power input for the thermal model.

For material flow analysis, the extruded wire and the remnant in the chamber were sectioned, ground, polished, and etched, and metallurgical inspections of the sectional surfaces were made using an optical microscope, so that the positions of the inserted marker material could be revealed and measured due to the different microscopic features of the sample and marker materials.

CHAPTER 3 LITERATURE REVIEW ON THE APPLICATIONS OF NUMERICAL METHODS

3.1 Numerical Methods on Metal Forming

Metal forming is a process of converting raw materials into products with custom shapes and mechanical properties through mechanical deformation. The forming of industrial products can be achieved by many different processes, such as extrusion, drawing, rolling, forging, stamping, and so on. During metal forming processes, the process materials usually experience large and permanent deformations with or without high temperature which is below melting temperatures of the materials. One attractive advantage of metal forming is that the workpiece is reshaped without adding or removing material and its material mass remains unchanged [7]. By the definition, friction extrusion process can be classified as a type of metal forming.

The development of metal forming before the invention of computational tools and numerical techniques was mainly based on trial and error method and empirical analysis. After 1980's, the metal forming industries advanced very fast with the exponentially developing computational capabilities and numerical simulation methods. Specially, the fast developing finite element methods made it possible to simulate the metal forming processes for design purposes. The benefits of numerical simulations are obvious. First, with the help of numerical simulations, the cycle of metal forming processes development can be largely reduced, because metal forming simulations can run different conditions

with easy and much shorter time is needed than conducting experiments. Secondly, design costs can be saved a lot. The simulations also can predict possible defects and potential operating problems and thus reduce physical prototyping and testing. They are also a good tool to help optimize designs and to reduce material usage.

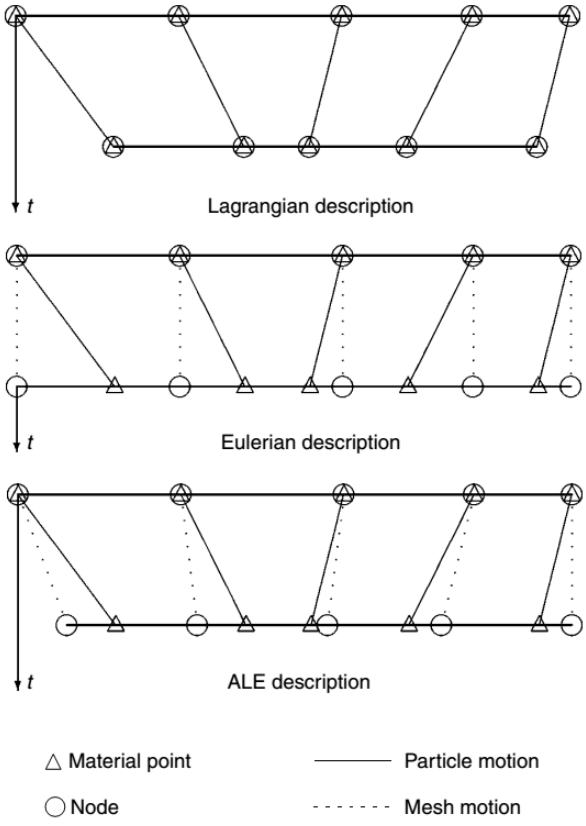

Figure 3.1 One-dimensional example of Lagrangian, Eulerian and ALE mesh and particle motion [62].

Before to review the numerical simulations on metal forming process, it is necessary to talk about the descriptions of motion. The numerical simulation of multidimensional problems in fluid dynamics and nonlinear solid mechanics usually make use of two classical descriptions of motion: the Lagrangin description and the Eulerian

description [8]. The arbitrary Lagrangian - Eulerian (ALE) description was developed to combine the advantages of the classical descriptions. A schematic of the descriptions is shown in Figure 3.1. In Lagrangian formulations, each individual node of the computational mesh sticks to the associated material particle motion. Since there is no relative velocity between mesh and material, no convection term needs to be taken care in the governing equations. In the Eulerian formulation, the computational mesh is fixed in the space and the material flows through the grid. Apparently, there is relative velocity between mesh and material and the convection between them shows up. In the ALE description, the computational mesh nodes can be moved totally with the associated material particles like in Lagrangin formulation, or be fixed as in Eulerian description, or, as shown in Figure 3.1, be moved in a custom way to avoid excessive mesh distortion and deformation.

It is not easy to implement metal forming numerical simulation since metal forming is a class of highly nonlinear continuum mechanics problems. It involves large deformations which cause geometric nonlinearity, material nonlinearity (plastic deformation), and nonlinear boundary conditions [9]. The finite element formulation for large displacement and large strain problems was first proposed by Hibbitt et al. [10] to address the elastic-plastic behavior in metals. It is known as Total Lagrangian formulation in which the initial configuration is used as reference for the description of the motion. McMeeking and Rice [11] later on developed the Updated Lagrangian formulation, which uses the current configuration as reference, based on previous work for the same problems of large elastic-plastic flow. Theoretically, the above two formulations are the same and same results can be obtained [12]. Both Total Lagrangian and Updated Lagrangian

formulations use the Lagrangian description so they are Lagrangian formulations. Bathe gave a consistent summary of finite element incremental formulations for nonlinear static and dynamic analysis in both Total Lagrangian and Updated Lagrangian forms with detailed derivations [13]. These finite element methods were developed and widely adopted by other researchers for numerous different applications including metal forming.

Due to limited computing capabilities, most of early applications of finite element methods to metal forming processes focused analysis of plane strain or axisymmetric problems, such as disk forging of cylindrical fasteners and extrusion, because they can be solved in two dimensions. An incremental variational finite element formulation was employed to study stretch-forming and deep drawing problems with consideration of contact at blank holder, die, die profile, and punch head by Wifi [14]. Lee et al [15] presented a complete stress and deformation analysis for plane strain and axisymmetric extrusion which had not previously been obtained for general two and three dimensional problems in steady state. Wall ironing was analyzed by Odell [16] using an elastic-plastic finite element technique to study the effects of the ironing ring semi-cone angle and friction on the maximum reduction ratio. Wang and Budiansky [17] applied finite element modeling to stamping of sheet metal by arbitrarily shaped punches and dies based on nonlinear theory of membrane shells. Coulumb friction was adopted between sheet metal and tools and the predictions were compared with experimental data. The metal sheet forming were intensively studied by others [18-20]. Upsetting problems were investigated by Yamada et al [21], Nagtegaal and De Jong [22], and Kudo and Matsubara [23]. Other researchers [24-30] also successfully solved forming processes by using finite element formulations.

Various finite element approaches for metal forming simulation are dependent upon material's constitutive equations [31]. In addition to the above reviewed work in which elastoplastic analysis was focused in the Lagrangian frame, two major other material behaviors were introduced for the simulation of metal forming processes. One is the rigid-plastic finite element formulation which assumed that elastic deformation is negligible compared with plastic deformation in metal forming processes. The simplification allows larger increments of deformation and thus saves computational cost with reasonable accuracy. The incompressibility constraint can be removed by introducing either the Lagrangian multiplier [32] or a penalty function [33]. Lung and Mahrenholtz [34] applied the upper bound theorem of plasticity to rigid-plastic finite element formulation. Strain hardening and wall friction were taken into account by iterative treatment and sheet drawing with the formulation was analyzed. Kobayashi and Shiro [35] summarized the solutions of simple compression, heading, drawing, and extrusion. Chen and Kobayashi [36] obtained a complete solution of ring compression. Oh and Kobayashi [19] compared the solutions from rigid-plastic finite element formulation and elastoplastic finite element formulation with simulations on sheet bending problems and observed a good agreement between them. Gotoh and Ishise [37, 38] studied the flange deformation in deep drawing based a fourth-degree yield function. Mori et al [39] investigated steady and non-steady state strip rolling. The implicit scheme to solve the rigid-plastic finite element equations to determine the incremental displacement field was introduced by Kim and Yang [40] and Yoon and Yang [41]. This scheme was developed by other researchers to deal with rigid-plastic finite element simulations for metal forming processes [42-44].

Another finite element formulation is for viscoplastic materials. Zienkiewicz and his colleagues [45-48] first developed the finite element formulation for large deformation processes involving plastic or viscoplastic materials in the Eulerian frame. It is assumed that the elastic deformation can be considered as negligible compared with plastic deformation. The constitutive relations can be expressed in an Eulerian form linking the stresses and current strain rates in the form of a viscous flow relation, equivalent to the flow of a viscous, non-Newtonian, incompressible fluid. This finite element formulation uses the Eulerian description of motion so it can deal with extremely large deformation and distortion of material and so good quality mesh can be retained. But the disadvantage is that it is hard to predict the motion free surfaces. In reference [46], extrusion simulations with such viscoplastic finite element formulation were conducted and the results were compared with the known slip line solutions. Zienkiewicz et al [47] explored the application to steady state flow in extrusion, drawing and rolling processes. Transient free surface solutions were also demonstrated for stretch forming and deep drawing. It was concluded that the formulation is capable of dealing with boundary friction and strain hardening. Zienkiewicz and Cormeau [45] presented a unified numerical solution approach for this type of formulation and introduced certain numerical information on solution stability. Later, Zienkiewicz et al [48] developed a finite element formulation algorithm for solving the coupled thermal viscoplatic flow so the a simultaneous solution for velocities and temperatures can be obtained. Examples of simulations on steady state extrusion and rolling problems showed the applicability of the method. Dawson [49] presented a method to determine the strain history throughout a body in the Eulerian frame and extended a viscoplastic finite element formulation to include strain history independence. The method

was used to analyze slab rolling and axisymmetric extrusion. The Eulerian finite element formulation was also used to simulate other processes, such as metal cutting , which predicted the chip geometry, the tool-chip contact length, flow field, stress and strain rate distributions. Finite element formulations for viscoplastic material were also developed and applied to analysis of metal forming processes [50-52].

For the Lagrangian finite element formulations, the mesh sticks the material and the large deformation and distortion of the body cause bad quality mesh. With the error accumulation due to bad mesh, the computational errors become unacceptable and the computation may abort. Methods for remeshing during computation were developed to solve the difficulties caused by large deformation and distortion of the material. Cheng [53] and Kikuchi proposed a mesh re-zoning scheme based on some fundamental properties of finite element approximations for finite element simulations of metal forming processes. Later, Cheng [54] developed an automatic remeshing scheme that enables finite element simulation of complicated metal forming processes. This technique can avoid the tedious procedures of interrupting the analysis, performing remeshing, mapping and preparing new boundary conditions during the analysis. Petersen and Martins [55] presented an automatic finite element remeshing system for quadrilateral elements. PavanaChand and KrishnaKumar [56] discussed the issues involved in data transfer during remeshing for large deformation elastoplastic analysis using the Updated Lagrangian finite element formulation. Hattangady et al. [57] discussed the issues to deal with automation of the 3D modeling of forming processes and developed procedures to simulate forging processes. Hamel et al [58] used remeshing techniques in finite element analysis of clinch processes.

Other [59-61] researchers also studied the remeshing algorithms and applied them to modeling of metal forming processes.

To deal with the large deformation and distortion during simulation of metal forming processes, the Arbitrary Lagrangian Eulerian finite element formulations were also developed and showed great potentials. The ALE description combines the advantages of both Lagranian and Eulerian descriptions, while minimizing their drawbacks as far as possible. The difference between ALE formulations and other approaches is that the mesh is allowed to move independently with material in order to maintain the mesh quality during the computation. The ALE method can avoid excessive element deformation and distortion, which are the disadvantages of Lagrangian formulations, and capture the free surface motion as well, which is the weakness of Eulerian formulation. Compared with remeshing techniques, the ALE approach has more attractive advantages. The ALE formulations optimize the computational mesh to achieve an improved accuracy with low computing cost and thus it is more efficient, because the total number of the elements and the element connectivity in a mesh remains unchanged during the computation due to unchanged mesh topology [62].

The concept of ALE was first proposed to solve hydrodynamic problems with a moving fluid boundary using a finite difference scheme [63]. Due to its attractive merits, the ALE method was studied widely in fluid-structure interaction area [64-67]. The ALE formulation was later extended to nonlinear solid and structural mechanics. Haber [68] presented the ALE finite element formulation on large deformation frictional contact and fracture mechanics. Liu et al. [69] formulated an ALE finite element method for path-dependent material suitable for both geometrical and material nonlinearities. Schreurs [70]

described a procedure for automatic mesh adaption and applied the ALE finite element to modeling of axisymmetric forming processes. Ghosh and KiKuchi [71] performed analysis of large deformation of elastic-viscoplastic materials using the ALE finite element method. Benson [72] presented the operator-split ALE method which makes the ALE implementation easy. It was stated that the ALE can be finished by two steps --- the Lagrangian step that the mesh moves with the material, and the Eulerian step in which the mesh moves to maintain good mesh quality. This technique can extend Lagrangian formulations to ALE formulations easily and so was used widely later by researchers since it is easier to implement based on current Lagrangian formulation codes. Gadala and his coworkers [73-76] developed a coupled implicit ALE formulation which differs from the operator-split technique. The mesh motion and material deformation are solved at the same time rather sequentially. This formulation has more clear physical meaning but it is not as computationally convenient as the uncoupled formulation.

ALE formulations has been used to analyze metal forming processes widely due to its abilities. Couch et al. [77] evaluated the utility of the ALE method in simulating large deformation metal forming processes, such as casting, forging and extrusion. Pros and cons for this approach were discussed. Gadala and Wang [78, 79] applied the ALE approach to simulation of punch indentation, metal extrusion and compression between wedge-shaped dies and found that the load fluctuation which is normally associated with updated Lagrangian formulations is eliminated by using ALE. Olovsson et al. [80] used the ALE method to simulate metal cutting operations and concluded that the ALE formulation shows promising results and seems numerically robust. Aymone et al. [81] proposed two mesh node point relocation techniques to improve the mesh during computation and applied them

to metal forming processes. Boman et al. [82] simulated the steady state of a 3D U-shaped cold roll forming process using the ALE method and obtained more accurate contact prediction and better representation of the sheet. Davey and Ward [83, 84] employed the ALE formulation combined with a flow formulation and an iterative solution scheme to simulate the ring-rolling process and there is friction at a mandrel interface.

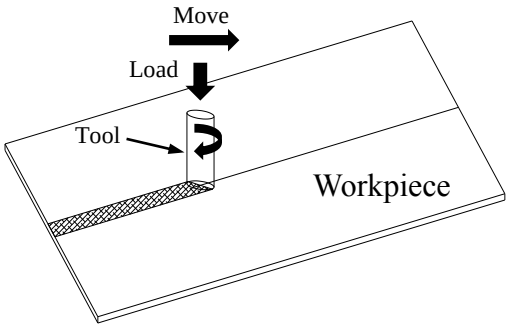

Figure 3.2 A schematic diagram of friction stir welding.

3.2 Numerical Methods on Friction Stir Welding

A similar material process to the friction extrusion process has been studied widely and applied to industries for years. It is the friction stir welding process, as shown in Figure 3.2, also a friction based process. In friction stir welding, a rotating tool is used to generate frictional heat in the workpieces and to create material flow and mixing in the workpieces, leading to the formation of a solid-state weld joint. A key similarity of friction extrusion and friction stir welding is that the heat source comes from severe plastic deformation in the metal and from the friction between the tool and metal. Another similarity is that the products, i.e. the welded joint and the extruded wire, have a similar thermal–mechanical history and experience an analogous stirring process, which largely affects the mechanical properties of the products. Due to the similarities between friction extrusion and friction

stir welding and the lack of numerical studies of the friction extrusion process in the literature, it is also useful to consider the approaches applied to the friction stir welding which can be applicable for friction extrusion process.

One of the important aspects that have been studied numerically well in the friction stir welding is the heat transfer phenomenon. As in friction extrusion, heat generation comes from the friction between tool and workpiece and plastic deformation. Many thermal models have been developed to approximate the heat generation during the friction stir welding. Could and Feng [85] presented an analytical solution to predict the temperature field by using simplified assumptions based on the point heat source concept. A drawback of this model is that the point heat source cannot represent the heat generation during the friction stir welding well since the area of the friction between the tool and workpiece is not small. Frigaard et al.[86] developed a three-dimensional heat flow model. Sliding friction was assumed and Coulomb's law was used to calculate the shear stress. The frictional coefficient was adjusted at elevated temperature by not allowing the temperature beneath the tool shoulder to exceed a chosen temperature. Khandkar et al. [87, 88] proposed a pure thermal model, in which the moving heat source is correlated with the actual machine power input on the interfaces between the tools and workpiece, to predict the temperature distribution and a good agreement between predictions and experimental measurements was obtained. Chao and Qi [89] developed a thermal model that used trial and error to find the total heat input rate. Only the frictional heat between tool shoulder and workpiece was considered and the heat generation rate on the tool should is linearly distributed along radial direction. Later, Chao et al. [90] estimated the total heat flows into the workpiece and tool based on the model in [89] and concluded that the majority of heat

generated from friction, about 95%, is transferred into the workpiece. Song and Kovacevic [91] presented a thermal model to model the heat transfer in friction stir welding. It was assumed that there was no sticking between the tool shoulder and workpiece and thus the Coulomb friction was used to approximate the frictional heat generation between the tool shoulder and workpiece. Sticking was assumed on the pin surface so the average shear stress was used to estimate the heat generation at the pin surface. Schmidt et al. [92] presented analytical estimation of the heat generation based on assumptions for different contact conditions at the tool/workpiece interface in friction stir welding. For sliding condition, the Coulomb's law was used to calculate the contact shear stress and then the heat generation on the interface. For sticking condition, the yield shear stress at certain temperature was used to approximate the heat generation. The combination of the above methods was used for partial sliding/sticking condition. Schmidt and his coworkers [93, 94] developed thermal modeling on friction stir welding based on the analytical estimation of heat generation. All the above thermal models assume that the plastic deformation in the volume is either negligible or seemed in a thin layer near the tool. On the contrary, the plastic deformation as the sole heat generation was also used to predict the temperature distribution through the computational fluid dynamics (CFD) approach [95-97]. In these models, it was assumed that the fluid on the tool/workpiece interfaces stuck totally or partially on the tool and the frictional heat was not computed. The combination of these two forms of heat generation, i.e. frictional heat generation and plastic dissipation, is also adopted in the heat transfer modeling [98].

Another important phenomenon during friction stir welding that also has been studied by many researchers is material flow. Since the material near the tool experiences

large distortion, the regular Lagrangian finite element formulations have difficulties to simulate this process when handling excessive mesh entanglement. In addition, the extreme deformation only happens along the joint line where the tool pass and other surfaces almost remain unchanged. Considering these two characteristics, the Eulerian formulations are more appropriate to simulate friction stir welding process because the mesh distortion can be easily avoided and no free surface motion needs to be captured. Studies on friction stir welding using CFD modeling can be found in a considerable body of literature.

With Eulerian formulations, the processing metals are seemed as a fluid whose viscosity, correlated with flow stress, may depend on strain rate and temperature. The constitutive model introduced by Sheppard and Wright [99] using the Zener-Hollomon parameter [100] has been intensively used in the simulation of friction stir welding and extrusion. By using this model, the viscosity of metals is a function of temperature and strain rate. Ulysse [95] presented a three dimensional CFD model to study the effect of tool speeds on temperature. The heat generation due to plastic deformation was used in the simulation and it was assumed that 90% was converted into heat. Forces acting on the tool were computed for various welding and rotational speeds. It was found that pin forces increase with increasing welding speeds but decrease with increasing rotational speeds. Seidel and Reynolds [101] developed a two-dimensional friction stir welding model to investigate the material flow. It is also fully thermo-fluid coupled model that heat generation comes from plastic deformation. The predicted flow field agreed very well with material flow visualization experiments. Colegrove and Shercliff [102] conducted a series of friction stir welding experiments to provide validation data for a CFD model. They found that the type of tool material affected temperature profiles and the peak temperature which

was near solidus temperature limited heat generation. At last they found a way to estimate the power input and it was verified by the CFD model. Later, Colegrove and Shercliff [96] applied CFD approach to model the metal flow in friction stir welding. The models used a threaded took raked 2.5° away from the direction of travel and different conditions, such as unthreaded tool and isothermal condition, were tried. It was found that the temperature over-prediction and lower predicted force could be addressed by either using a slip model or adjusting the viscosity when close to solidus temperature. The vector plots of velocity showed that at the boundary between the rotating and stationary flow regions the strain rate was 2/s. Colegrove and Shercliff [103] continued to explore the friction stir welding with CFD modeling. Heat flow and the material flow near the tool were discussed.

Since the constitutive models are equations fitted by experimental data, some material behaviors may not be described properly under some extreme conditions, such as at very high strain rates and temperature near solidus temperature. As a result, the material constitutive relations must be adjusted in order to avoid unreasonable predictions in the numerical simulations. Long and Reynolds [104] did a series of parametric studies of friction stir welding by a two-dimensional CFD model. They tested the effects of viscosity, thermal diffusivity, and process parameters. They concluded that the reduced viscosity results in relative lower peak temperature and that there is a minimum in x-axis force at intermediate rotation rate and it is related to a non-linear flow stress decline.

All of these studies used viscous dissipation or plastic deformation as the heat generation source. As mentioned above, some other heat transfer models also were used. Nandan et al. [105-107] conducted numerical simulations with CFD models on different metals, i.e. aluminum alloy 6061, 304 stainless steel, and mild steel. Temperature fields

and material flow were modeled to help understand the mechanisms during friction stir welding. The heat source was estimated by the material shearing near the tool surface. It was found that significant asymmetry of heat and mass flow, which increased with welding speed and rotational speed, was observed on aluminum alloy 6061. Compared with the experimentally determined thermo-mechanically affected zone geometry, the cutoff viscosity above which no significant material flow occurs was found to be 5×10^6 Pa-s during friction stir welding of aluminum alloy 6061 [105].

Atharifar et al. [108] used a combination of viscous dissipation and frictional heating between the tool and workpiece as the heat generation source and a different material constitutive model in a three-dimensional CFD model of friction stir welding on aluminum alloy 6061. It was concluded that including the sliding/sticking behavior promotes the accuracy of numerical results and the Carreau viscosity model can properly simulate the viscosity field. Chase et al. [109] simulated the control of the temperature of a friction stir welding tool using a CFD model. The axial force during the friction stir welding process was examined when the tool was maintained at an elevated temperature and the tool temperature was optimized to reduce the axial force. Aljoaba et al. [110] studied the effects of coolants used during friction stir welding to the resulting grain size. Two three-dimensional CFD models were developed, one with coolant and the other one without coolant. The grain size after recrystallization was predicted by correlating to the Zener-Holloman parameter and temperature. Different stirring conditions also were tested to investigate the material flow and microstructural modification. Hasan et al. [111] compared the flow behavior in friction stir welding using unworn and worn tool geometries by numerical models. A validated model of the friction stir welding process was first

generated using CFD software FLUENT and then it was used to compare the differences in the flow behavior, mechanically affected zone size, and strain rate distribution around the tool for both unworn and worn tool geometries. The results show that a low stirring action for the worn tool, particularly near the weld root, potentially leading to defective weld joints. Su et al.[112] also studied the influence of too/pin shapes on the thermal and material flow behaviors in friction stir welding through CFD modeling. Two different pin shapes, axisymmetric conical tool and asymmetrical triflat tool, were used and a partial sticking/sliding contact condition was set at the tool-workpiece interface. The found that the deformation zone caused by triflat tool is larger than that by conical tool.

As discussed above in section 3.1, due to its ability to handle excessive element distortion and large deformation, the ALE finite element formulations also have been used for modeling friction stir welding. Deng et al. [113, 114] were the first to use the ALE method to study the material flow. A two-dimensional model with temperature field incorporated was developed to investigate the material flow [114]. Two different contact conditions were tested. One is partial slipping/sliding in which the material at the workpiece/tool interface rotates with an angular velocity smaller than tool rotating speed. The other one is friction contact condition that is described by a modified Coulomb friction law, which doesn't let the frictional stress beyond the material shear yielding. Material flow pattern predictions were found to compare favorably with experimental observations. Schmidt and Hattel [115] presented a fully coupled thermo-mechanical three-dimensional finite element model using ALE formulation. The model allows separation between the workpiece and the tool and thus can observe the void formation. It was reported that the heat generation was primarily caused by plastic dissipation since the sticking condition was

present at the majority of the contact interface. Assidi et al. [116] conducted numerical simulations based on ALE formulation and used experiments with unthreaded concave tool at different welding speeds for to do calibration. Different frictional coefficients were tried and the best calibration was obtained for the Coulomb law using the frictional coefficient 0.3 which is the value used widely in the literature. van der Stelt et al. [117] simulated the material flow around the pin during friction stir welding using a two-dimensional plane strain model. ALE method and adaptive smoothed finite element method were implemented and compared with an analytical model. It was reported that the both methods can accurately predict the stress distribution and the ALE method is preferred since it is more accurate. The plunge stage of friction stir welding for joining dissimilar aluminum alloy 6061 to steel was simulated by a coupled thermo-mechanical model [118]. The axial welding force was predicted reasonably compared with experimental measurement although deviations were observed at later plunge stage. Studies of friction stir welding by using the ALE approach also were conducted by others [119-121].

Other numerical methods, such as smoothed particle hydrodynamic method [122] and coupled Eulerian/Lagrangian method [123], were used to simulate the friction stir welding process. Detailed reviews on numerical modeling of friction stir welding also reported [124, 125].

CHAPTER 4 FLOW VISUALIZATION STUDY

During friction extrusion process experiments, since the tools are not transparent and the process mainly happens in the chamber, the precursor is invisible. Although some experimental measurements can be made during experiments, such as temperature variations at some points, it is very difficult to measure the material transport and flow variations by experimental means or only limited information can be obtained experimentally. However, to study the material flow in the chamber is a crucial part of our studies and it helps understand the complicated physical mechanisms in friction extrusion process. To overcome this difficulty, a visualization study with transparent tools and fluid has been conducted to improve our qualitative understanding of the friction extrusion process.

A physical model has been developed to implement the visualization study on friction extrusion process. The purpose of the model is to use transparent tools, including a chamber wall, a die, a back plate, and a transparent viscous fluid to mimic the same process of friction extrusion process. Because everything is transparent in the system, it is very convenient to make some experimental measurements and easy to observe the material flow. It is a simplified model that doesn't have extrusion process but only stirring. The die only rotates along its axis to stir the fluid in the chamber and no extrusion happens.

The current work focuses on numerical and analytical studies on the flow visualization model. Since the shapes of the geometry and boundary conditions are regular

for the simplified model, an analytical solution can be achieved. In the subsections, the model is described in detail and analytical solutions and numerical predictions are presented. The analytical solutions and predicted results are then compared with experimental measurements.

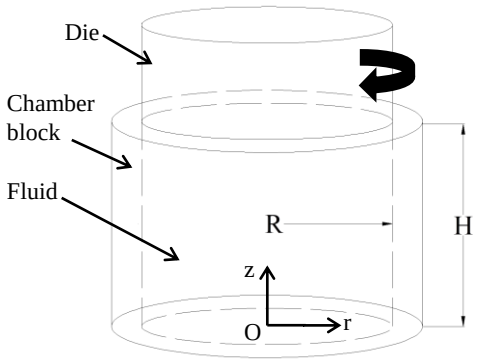

Figure 4.1 The simplified process.

4.1 Model Introduction and Experimental Procedure

It is a simplified model for friction extrusion process. A schematic diagram for this model is shown in Figure 4.1. A cylindrical hollow chamber made with transparent resin, with a height of H and an internal radius of R, is filled with a very viscous model fluid. A cylindrical die comes into contact at the top surface of the fluid. When the die rotates at an angular speed of ω, the liquid at the contact interface will rotate at the same angular speed due to the viscous nature of the fluid, thus providing a no-slip contact boundary condition for the fluid volume at the contact interface. Compared with the friction extrusion process, the simplified process considers the fluid motion due to the die rotation but not due to extrusion, so that an analytical solution can be obtained to provide verification for the numerical simulation prediction.

The model fluid used in this simplified process is an incompressible and highly viscous Newtonian fluid (instead of a non-Newtonian fluid) with a constant viscosity μ, which also enables the availability of an analytical solution. Syrup is chosen for the fluid as it is both clear and very viscous. The viscosity is about 2.5 Pas-s.

Besides the no-slip boundary condition at the die-fluid interface, the other boundary surfaces (the vertical cylindrical surface and the bottom surface) of the process chamber are also taken to have the no-slip boundary condition. As such, at the die-fluid interface, the velocity boundary condition is that the velocity at a distance of r to the center point has a magnitude of ωr and is along the angular (tangential) direction consistent with the rotation of the die, and at all other surfaces all normal and tangential velocity components are zero.

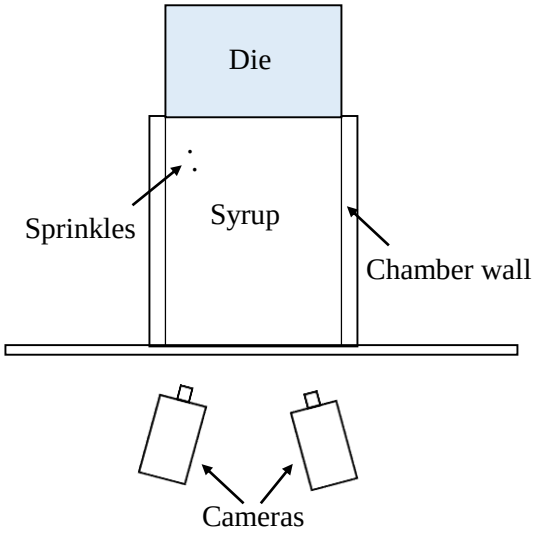

Figure 4.2 Experiment setup.

A schematic diagram of the experimental setup for the simplified model is shown in Figure 4.2. As introduced, all the tools and the fluid are transparent so that it is very convenient for observation and measurements. The chamber has an internal diameter of 19

mm and the height is 44 mm. Some small round particles, i.e. sprinkles, were used to insert into the fluid at different heights and radii. The density of the particles is about the same with the fluid, so the particles can suspend in the fluid and also can move with the near fluid without relative velocity given that the fluid velocity is small. A DIC (digital image correlation) system was used to track the motion of the particles in the fluid.

In order to correlate the model with friction extrusion process experiments, the rotation speed of the die is determined by keeping the Reynolds number the same. In a cylindrical vessel stirred by a central rotating agitator, the Reynolds number [126] is $Re = \frac{\rho \omega D^2}{\mu}$, where ρ is density, ω is rotation speed, D is the diameter of the agitator, and μ is the viscosity of the fluid. The rotation speed in the friction extrusion experiment used in this work is 300 rpm. The viscosity of the precursor in friction extrusion process is estimated as 1×10^3 Pa-s at high temperature. Based on these, the rotation speed was taken as 0.5 rpm. The calculated Reynolds number is very small, less than 1, indicating this is a laminar flow.

4.2 Analytical Solution

Since the problem has regular geometry and boundary conditions, an analytical solution can be achieved. Only the steady state flow is considered here. The flow is laminar due to small Reynolds number. Heat transfer is not included due to the fact that the amount of heat generated by viscous dissipation is negligible. The focus of interest of this analytical solution is the velocity field in the process chamber under the action of the rotating die at the die-fluid interface.

To take advantage of the cylindrical geometry of the fluid volume, a cylindrical coordinate system (r, θ, z) is employed as shown in Figure 4.1 where the angular position θ is not shown but its positive direction forms a right-hand coordinate system with the

positive directions of r and z. For easy observation, normalized values, such as normalized radius $\bar{r}$, the normalized distance from the top surface, i.e.,1-$\bar{z}$, and normalized velocity $\bar{v}$ are used in the solution development and discussion of simplified process.

Before making use of any symmetry the governing equations for incompressible steady state flow in a cylindrical coordinate system are given below.

Continuity equation:

$$\frac{\partial v_r}{\partial r} + \frac{v_r}{r} + \frac{1}{r}\frac{\partial v_\theta}{\partial \theta} + \frac{\partial v_z}{\partial z} = 0 \tag{4.1}$$

and Navier – Stokes equations:

$$\begin{aligned} &\rho\left(v_r \frac{\partial v_r}{\partial r} + \frac{v_\theta}{r}\frac{\partial v_r}{\partial \theta} - \frac{v_\theta^2}{r} + \frac{v_z \partial v_r}{\partial z}\right) \\ &= -\frac{\partial P}{\partial r} + \mu\left(\frac{\partial^2 v_r}{\partial r^2} + \frac{1}{r}\frac{\partial v_r}{\partial r} - \frac{v_r}{r^2} + \frac{1}{r^2}\frac{\partial^2 v_r}{\partial \theta^2} - \frac{2}{r^2}\frac{\partial v_\theta}{\partial \theta} + \frac{\partial^2 v_r}{\partial z^2}\right) + F_r \end{aligned} \tag{4.2a}$$

$$\begin{aligned} &\rho\left(v_r \frac{\partial v_\theta}{\partial r} + \frac{v_\theta}{r}\frac{\partial v_\theta}{\partial \theta} + \frac{v_r v_\theta}{r} + v_z \frac{\partial v_r}{\partial z}\right) \\ &= -\frac{1}{r}\frac{\partial P}{\partial \theta} + \mu\left(\frac{\partial^2 v_\theta}{\partial r^2} + \frac{1}{r}\frac{\partial v_\theta}{\partial r} - \frac{v_\theta}{r^2} + \frac{1}{r^2}\frac{\partial^2 v_\theta}{\partial \theta^2} + \frac{2}{r^2}\frac{\partial v_r}{\partial \theta} + \frac{\partial^2 v_\theta}{\partial z^2}\right) + F_\theta \end{aligned} \tag{4.2b}$$

$$\rho\left(v_r \frac{\partial v_z}{\partial r} + \frac{v_\theta}{r}\frac{\partial v_z}{\partial \theta} + v_z \frac{\partial v_r}{\partial z}\right) = -\frac{\partial P}{\partial z} + \mu\left(\frac{\partial^2 v_z}{\partial r^2} + \frac{1}{r}\frac{\partial v_z}{\partial r} + \frac{1}{r^2}\frac{\partial^2 v_z}{\partial \theta^2} + \frac{\partial^2 v_z}{\partial z^2}\right) + F_z \tag{4.2c}$$

where P is the pressure field, v_r, v_z, v_θ are the radial, axial and angular (tangential) velocity components, ρ is the mass density, μ is the viscosity and F_r, F_θ, F_z are body forces per unit volume.

With considerations of the particular geometry and boundary conditions, the following simplifications can be made: (a) the velocity and pressure fields do not have any θ dependence and (b) the radial and axial velocity components are zero everywhere. Hence,

$$v_z = 0;\ v_r = 0;\ \frac{\partial P}{\partial \theta} = 0 \tag{4.3}$$

$$\frac{\partial v_\theta}{\partial \theta} = 0 \tag{4.4}$$

For body forces, only the axial force is non-zero and others are zero:

$$F_r = 0;\ F_\theta = 0;\ F_z = -\rho g \tag{4.5}$$

Substituting (4.3), (4.4), and (4.5) into (4.2), the governing equations are reduced to

$$\rho\left(-\frac{{v_\theta}^2}{r}\right) = -\frac{\partial P}{\partial r} \tag{4.6}$$

$$\frac{\partial^2 v_\theta}{\partial r^2} + \frac{1}{r}\frac{\partial v_\theta}{\partial r} - \frac{v_\theta}{r^2} + \frac{\partial^2 v_\theta}{\partial z^2} = 0 \tag{4.7}$$

$$-\frac{\partial P}{\partial z} + F_z = 0 \tag{4.8}$$

It is worth noting that viscosity does not enter into the above governing equations. Hence, the resulting solutions are independent of the viscosity for this special case.

Since v_θ is a function of *r* and *z*, the method of separation of variables can be used to get:

$$v_\theta = U(r)W(z) \tag{4.9}$$

where $U(r)$ and $W(z)$ are functions to be determined. Substituting (4.9) into (4.7) and re-arrange it to get

$$\frac{\frac{d^2U}{dr^2}+\frac{1}{r}\frac{dU}{dr}-\frac{U}{r^2}}{U} = -\frac{\frac{d^2W}{dz^2}}{W} = -\lambda^2 \tag{4.10}$$

where λ is a constant.

Now introducing the following non-dimensional quantities:

$$\bar{\mathrm{r}} = \frac{r}{R}, u = \frac{U}{R\omega}, \bar{v}_\theta = uW,\ \bar{z} = \frac{z}{H}, \bar{\lambda} = \lambda R \tag{4.11}$$

where R is the radius of the process chamber, ω is the angular speed, and H is the height of the chamber. Two equations below can be derived from (4.10) after these quantities are substituted into equation (4.10)

$$\frac{\mathrm{d}^2W}{d\bar{z}^2} - \left(\frac{H}{R}\right)^2 \bar{\lambda}^2 W = 0 \tag{4.12}$$

$$\bar{r}^2\frac{d^2u}{d\bar{r}^2} + \frac{\bar{r}du}{d\bar{r}} + \left(\bar{\lambda}^2\bar{r}^2 - 1\right)u = 0 \tag{4.13}$$

The equation (4.12) is a second time differential equation and its general solution is

$$W(\bar{z}) = c_1 \exp(\frac{H\bar{\lambda}}{R}\bar{z}) + c_2 \exp(-\frac{H\bar{\lambda}}{R}\bar{z}) \tag{4.14}$$

where c_1 and c_2 are constants.

Equation (4.13) is a first-order Bessel equation and its general solution is

$$u(\bar{r}) = c_3 J_1(\bar{\lambda}\bar{r}) + c_4 Y_1(\bar{\lambda}\bar{r}) \tag{4.15}$$

where c_3 and c_4 are constants and $J_1(x)$ and $Y_1(x)$ are first-order Bessel functions of first kind and second kind, respectively. The general solutions for the Bessel functions of first kind can be expressed as

$$J_\upsilon(x) = \sum_{m=0}^{\infty} \frac{(-1)^m}{m!(m+\upsilon)!} (x/2)^{2m+\upsilon} \tag{4.16}$$

where υ is a real value, meaning the order of the Bessel function, and m and k are integers. The general solutions for the second kind,

$$Y_1(x) = \frac{2}{\pi} J_1(x) \left(\frac{\ln x}{2} + 0.5772\right) - \frac{1}{\pi} \sum_{m=0}^{\infty} \frac{(-1)^m \left(\frac{x}{2}\right)^{2m}}{m!(m+1)!} \left(\sum_{k=0}^{m} \frac{1}{k+1} + \sum_{k=0}^{m-1} \frac{1}{k+1}\right) \tag{4.17}$$

Then the general solution for the tangential velocity $\bar{v}_\theta$ can be written as

$$\bar{v}_\theta = W(\bar{z})u(\bar{r}) = (c_1 \exp(\frac{H\bar{\lambda}}{R}\bar{z}) + c_2 \exp(-\frac{H\bar{\lambda}}{R}\bar{z}))(c_3 J_1(\bar{\lambda}\bar{r}) + c_4 Y_1(\bar{\lambda}\bar{r}) \tag{4.18}$$

As described before, the contact between the fluid and chamber internal wall is non slip. So the boundary conditions for the normalized quantities are

$$\bar{r} = 0, \bar{v}_\theta = 0 \tag{4.19a}$$

$$\bar{r} = 1, \bar{v}_\theta = 0 \tag{4.19b}$$

$$\bar{z} = 0, \bar{v}_\theta = 0 \tag{4.19c}$$

$$\bar{z} = 1, \bar{v}_\theta = \bar{r} \tag{4.19d}$$

Imposing condition (4.19a) to (4.18),

$$\bar{r} = 0, \bar{v}_\theta = W(\bar{z})U(0) = 0 \tag{4.20}$$

If (4.20) is true for any $\bar{z}$, then $u(0)$ must be zero, namely

$$c_3 J_1(0) + c_4 Y_1(0) = c_3 * 0 + c_4 * (-\infty) = 0 \tag{4.21}$$

Solve (4.21),

$$c_4 = 0 \tag{4.22}$$

Similarly, from (4.19b),

$$c_3 J_1(\bar{\lambda}) = 0 \tag{4.23}$$

So the value of $\bar{\lambda}$ can be determined. There are infinite number of zero roots for $\bar{\lambda}$.

Then $u(\bar{r})$ can be written as

$$u(\bar{r}) = c_3 J_1(\bar{\lambda}\bar{r}) \tag{4.24}$$

From (4.19c), we can get

$$W(0) = c_1 + c_2 = 0 \tag{4.25}$$

Let $c_1 = -c_2 = c_5$ then

$$W(\bar{z}) = c_5 \sinh(\frac{H\bar{\lambda}}{R}\bar{z}) \tag{4.26}$$

Let $c = c_3 c_5$ and rewrite (4.18)

$$\bar{v}_\theta = c \sinh\left(\frac{H\bar{\lambda}}{R}\bar{z}\right) J_1(\bar{\lambda}\bar{r}) \tag{4.27}$$

Since there are an infinite number of eigenvalues $\bar{\lambda}$, $\bar{v}_\theta$ can be written as

$$\bar{v}_\theta = \sum_{n=1}^{\infty} c_n \sinh\left(\frac{H\bar{\lambda}_n}{R}\bar{z}\right) J_1(\bar{\lambda}_n\bar{r}) \tag{4.28}$$

Apply boundary condition (4.19d) to (4.28),

$$\bar{r} = \sum_{n=1}^{\infty} c_n \sinh\left(\frac{H\bar{\lambda}_n}{R}\bar{z}\right) J_1(\bar{\lambda}_n\bar{r}) \tag{4.29}$$

The Bessel function has one of orthogonality properties as follows [127]

$$\int_0^1 \bar{r} J_1\left(\bar{\lambda}_j\bar{r}\right) J_1\left(\bar{\lambda}_k\bar{r}\right) d\bar{r} = \begin{cases} 0, j \neq \mathrm{k} \\ \frac{1}{2}\left[\frac{dJ_1(x)}{dx}\right]^2_{x=\bar{\lambda}_k}, \ j = k \end{cases} \tag{4.30}$$

The solved constants are

$$\mathrm{c_m} = \frac{2}{\bar{\lambda}_m \sinh\left(\frac{H\bar{\lambda}_m}{R}\right) J_2(\bar{\lambda}_m)} \tag{4.31}$$

The final solution for the normalized tangential velocity is

$$\bar{v}_\theta = \sum_{n=1}^{\infty} \frac{2\sinh\left(\frac{H\bar{\lambda}_n}{R}\bar{z}\right) J_1(\bar{\lambda}_n \bar{r})}{\bar{\lambda}_n \sinh\left(\frac{H\bar{\lambda}_n}{R}\right) J_2(\bar{\lambda}_n)} \tag{4.32}$$

It is seen that the analytical solution is expressed in terms of a series of infinite number of terms. A convergence analysis of the series has shown that a converged value can be achieved very quickly except right on the rotating surface. In subsequent sections, the analytical solution is calculated using the first fifty terms to ensure a good convergence.

$$\int_0^1 \bar{r} J_1\left(\bar{\lambda}_j \bar{r}\right) J_1\left(\bar{\lambda}_k \bar{r}\right) d\bar{r} = \begin{cases} 0, j \neq \mathrm{k} \\ \frac{1}{2}\left[\frac{dJ_1(x)}{dx}\right]^2_{x=\bar{\lambda}_k}, \ j = k \end{cases} \tag{4.30}$$

The solved constants are

$$\mathrm{c_m} = \frac{2}{\bar{\lambda}_m \sinh\left(\frac{H\bar{\lambda}_m}{R}\right) J_2(\bar{\lambda}_m)} \tag{4.31}$$

The final solution for the normalized tangential velocity is

$$\bar{v}_\theta = \sum_{n=1}^{\infty} \frac{2\sinh\left(\frac{H\bar{\lambda}_n}{R}\bar{z}\right) J_1(\bar{\lambda}_n \bar{r})}{\bar{\lambda}_n \sinh\left(\frac{H\bar{\lambda}_n}{R}\right) J_2(\bar{\lambda}_n)} \tag{4.32}$$

It is seen that the analytical solution is expressed in terms of a series of infinite number of terms. A convergence analysis of the series has shown that a converged value can be achieved very quickly except right on the rotating surface. In subsequent sections, the analytical solution is calculated using the first fifty terms to ensure a good convergence.

4.3 Numerical Modeling

A three-dimensional CFD simulation of the simplified process was carried out without using the simplifications taken explicitly in obtaining the analytical solution. The simulation is performed in a rectangular Cartesian coordinate system with the same origin as the cylindrical coordinate system for the analytical solution.

Using the indicial notation, in which Latin indexes have ranges of 1, 2 and 3, the rectangular Cartesian coordinates are represented by x_i and the velocity components are represented by v_i. Now the governing equations, namely the continuity equation and the Navier-Stokes equations, for incompressible steady state flow are given in Cartesian coordinates by, respectively,

$$\frac{\partial v_i}{\partial x_i} = 0 \tag{4.33}$$

$$\rho v_i \frac{\partial v_j}{\partial x_i} = -\frac{\partial P}{\partial x_j} + \mu\left(\frac{\partial^2 v_i}{\partial x_i \partial x_j}\right) + F_j \tag{4.34}$$

The boundary conditions, namely that the top surface rotates at the angular speed ω and the other surfaces are stationary, are the same as for the analytical solution.

The CFD simulation was carried out only considering the fluid part with the following specific parameter values: ω=0.5 rpm, μ=2.5 Pa-s, R=19 mm and H=44 mm, which are the same as those used in experiment. Figure 4.3 shows the converged computation grid. It was found that a high mesh density close to the rotating surface, i.e. the die-fluid interface, is necessary to capture the high velocity gradients. Also, for the regions close to the other walls, finer mesh is needed. Boundary layer mesh which is finer is shown in Figure 4.3 (b). A numerical convergence analysis of the simulation solution was conducted. Based on original mesh, every cell was refined in three directions, i.e. split into eight cells. Then the numerical predictions using the refined mesh was compared with

that using original mesh. If the relative different is less 5%, both mesh grids can be considered converged mesh. In fact, right now the PC is powerful and able to handle considerable number of cells with ease. The CFD simulation predictions discussed below, which are presented together with the analytical solution for comparison purposes, are from the converged simulation solution.

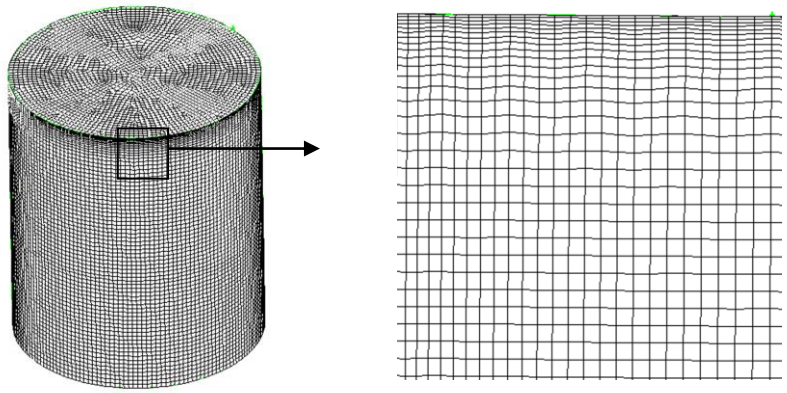

(a) (b)

Figure 4.3 (a) Mesh, (b) details for mesh boundary layer.

Finite control volume method was used to discretize the computational domain and ANSYS FLUENT was used to solve the governing equations. A second order discretization scheme was chosen for the pressure and a second order upwind scheme for the momentum equations. The SIMPLE algorithm was used for the pressure-velocity coupling [128]. A convergence could be reached easily for this problem.

4.4 Comparisons and Discussions

Converged simulation predictions are now presented together with the analytical solution for comparison purposes. The comparisons of CFD simulation predictions and the analytical solution of the tangential velocity along both axial and radial directions are shown in Figure 4.4. All values in the figures are normalized, including the geometric

dimensions and velocity values for a better understanding. It is seen that the two types of solutions almost overlap each other. Comparisons show that the differences between the two solutions are below 2 percent, indicating a good match. This good agreement between the analytical solution and the CFD simulation prediction confirms the validity of the simplifications made for the analytical solutions, i.e. the flow field is axisymmetric and the vertical velocity component is zero everywhere, and verifies the accuracy and reliability of the CFD simulation.

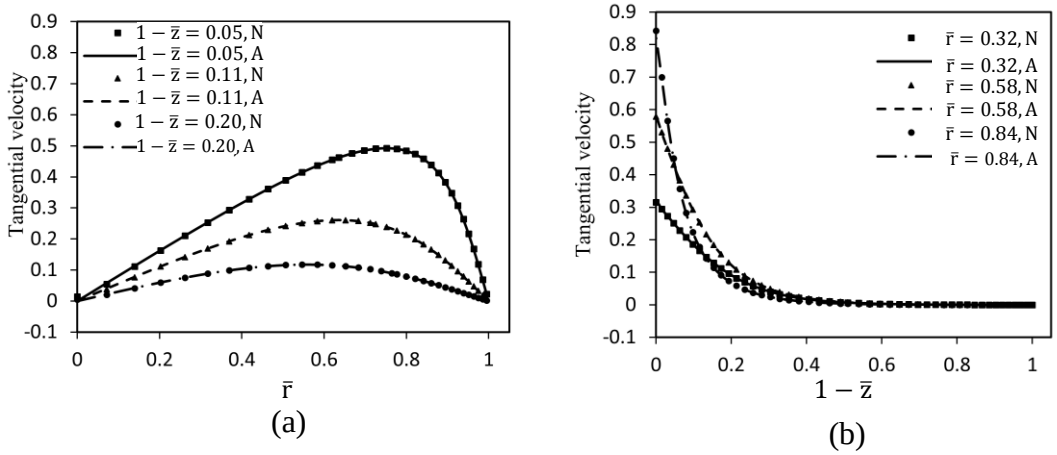

Figure 4.4 Comparison of CFD simulation prediction and analytical solution of the normalized tangential velocity variation: (a) along the axial direction with a normalized radius $\bar{r}$ = 0.32, 0.58 and 0.84; (b) along the radial direction at a normalized distance 1- $\bar{z}$ =0.05, 0.11 and 0.20 from the rotating surface, respectively. (N: numerical solution; A: analytical solution).

More specifically, Figure 4.4 (a) shows the normalized tangential velocity variations along the axial direction at a normalized radius $\bar{r}$ = 0.32, 0.58, and 0.84, respectively. The tangential velocity decreases away from the top surface and quickly drops to near zero at half way toward the bottom surface. Figure 4.4 (b) shows the normalized tangential velocity variation along the radial direction at a normalized distance 1- $\bar{z}$ = 0.05,

0.11 and 0.20, respectively, from the rotating surface. It is seen that the tangential velocity is largest at an intermediate radius toward the cylindrical wall of the process chamber.

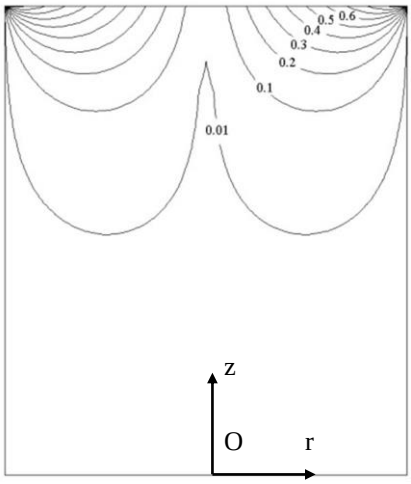

Figure 4.5 A contour plot of the tangential velocity.

A full view of the velocity field variation can be seen clearly from the contour plot of the tangential velocity on the Zr plane in Figure 4.5, in which normalized contour values are shown on a full rectangular cross-section of the process chamber. It is obvious that the velocity has the largest values in the upper left and upper right regions (these two regions are symmetric about the vertical centerline, which is the axis of the cylindrical chamber). These two regions, which are bounded from below by the 0.10 contour, occupy about 20% of the whole flow domain. In these two regions, the normalized velocity magnitude ranges mainly from 0.1 to 1, and in the rest of the chamber, the velocity magnitude is below 0.1. In other words, the dominant material flow activity occurs in a small region of the chamber, while in the rest of the chamber material flow is very limited. Also the velocity magnitude is relatively small along the cylindrical axis.

Generally speaking, the distribution of the velocity field is expected to be affected by the viscosity of the fluid. However, from the analytical solution, it is seen that the velocity field is independent of viscosity. This independence is a consequence of the use of a Newtonian fluid, which has a constant viscosity. For non-Newtonian fluids, the viscosity is not a constant (e.g. with dependence on temperature and strain rate) and is expected to affect the velocity distribution.

Since the CFD simulation predictions have been shown earlier to be almost the same as the analytical solution for the modified process, and the analytical solution provides more mathematical convenience, experimental validation of the analytical solution and CFD simulation predictions is performed below in the form of comparisons between the analytical solution and experimental measurements.

The comparisons between analytical solution and experiment measurements are shown in Figure 4.6. The analytical solution is derived from equation (4.32) by using the measured ($\bar{r}$, 1- $\bar{z}$) coordinates of the marker particles since these two coordinates for a given particle are found to change with time in the experiment. It is noted that, in the perfect world of the analytical solution, the particles are required to keep these two coordinates constant. This is believed to be the main reason for the differences between the analytical solution and the experimental measurements.

In Figure 4.6, the experimental measurements are from six marker particles (#1~#6 in the figures) that were tracked during the experiment. The positions of the particles were recorded every 10 seconds. The measured velocity varied with time due to the fact that during the experiment the particles oscillated not only up and down, but also along the

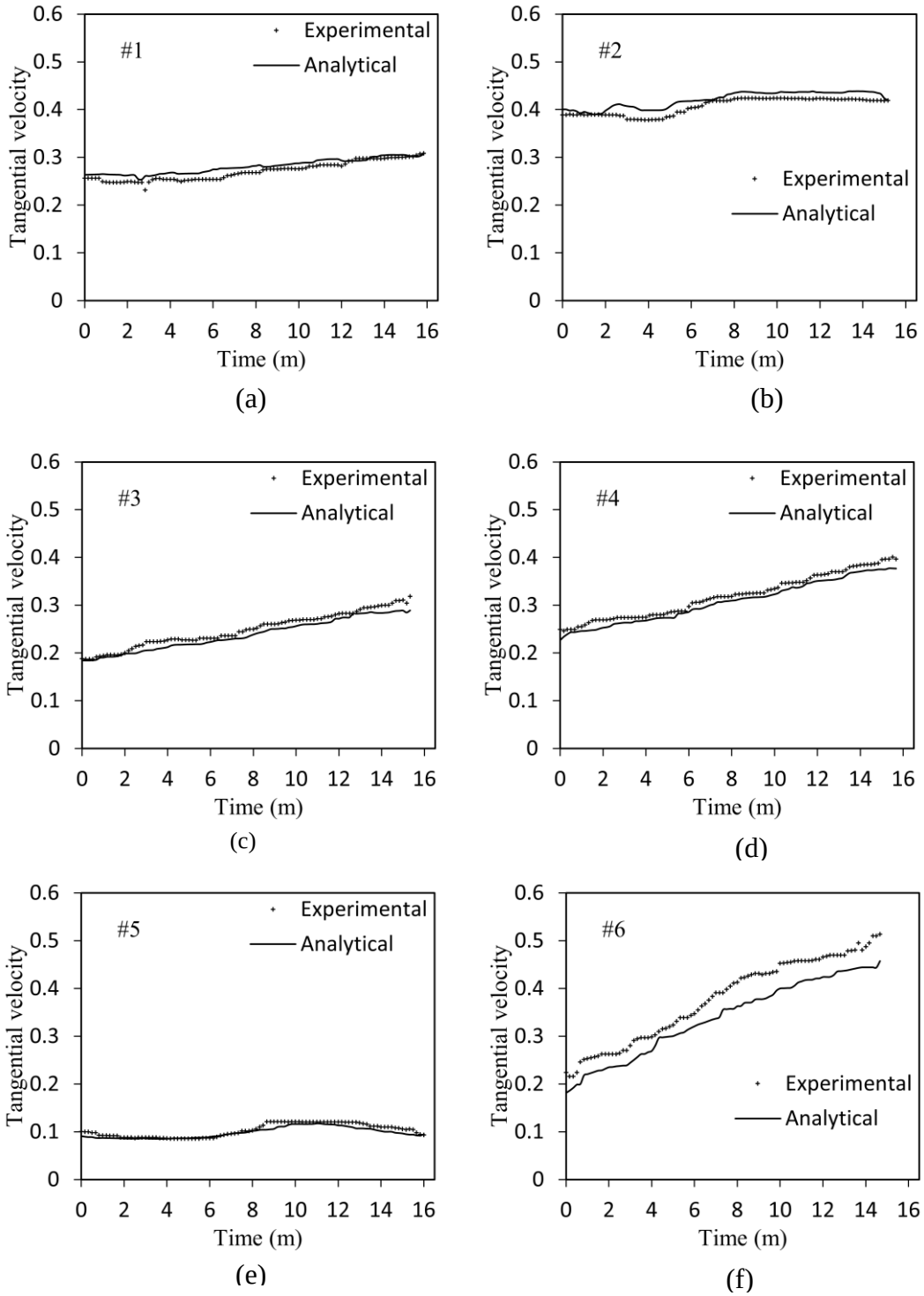

Figure 4.6 Comparisons of the analytical solution and experimental measurements of the normalized tangential velocity variation with time for (a) marker particle #1, (b) marker particle #2, (c) marker particle #3, (d) marker particle #4, (e) marker particle #5, and (f) marker particle #6, respectively.

radial direction. That is, as noted earlier, the ($\bar{r}$, 1- $\bar{z}$) coordinates of the particles changed with time, as shown in Figure 4.7.

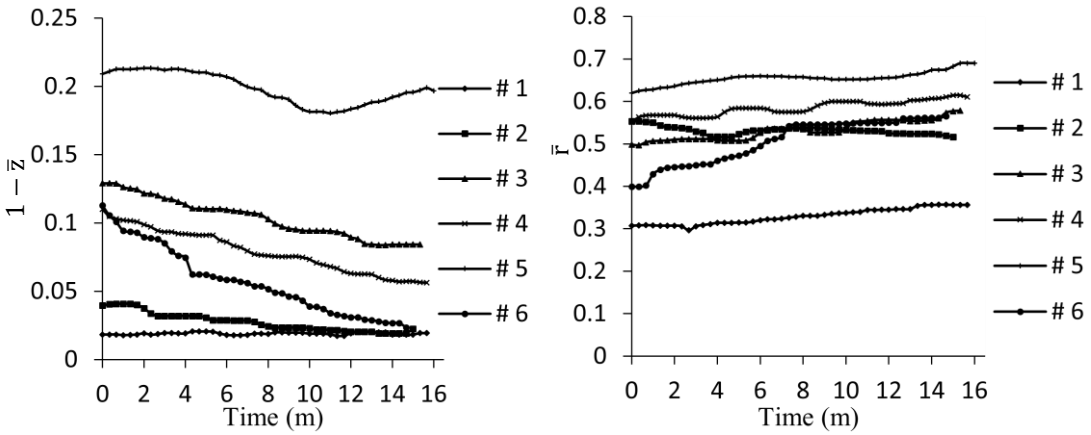

Figure 4.7 Variation of (a) height and (b) radius with time for the six markers particles.

It is seen from Figure 4.6 that the velocity values from the analytical solution and experimental measurements are very close. The qualitative trends are the same and the quantitative differences are small. Most the quantitative differences are less than 6% in Figure 4.6(a) - (e) and less than 12% in Figure 4.6(f). The main factors that may have contributed to the differences during experiments include the wobbling motion of the die due to misalignment of the die axis with the drive shaft. Improvements will be made in the future to minimize experimental errors. Nonetheless, the current comparisons between the analytical solution and experimental measurements show a good agreement, which serves as an evidence for experimental validation of the analytical solution and CFD simulation predictions.

4.5 Summary and Conclusions

In this chapter, a simplified model has been studied and it is to mimic the material flow features during friction extrusion process. The model includes a rotating die under a Newton fluid in a chamber. The Reynolds number is equal to that estimated in the friction extrusion process. Due to the regularity of the problem, an analytical solution has been derived based on some reasonable assumptions. A CFD simulation of the problem also has been performed but without any assumptions. A very good agreement between the analytical solution and the numerical predictions can be observed and the assumptions made in the derivation of the analytical solution are verified. The numerical solution also was compared with experimental measurements made through a DIC system on small solid particles in the fluid. The comparisons show that the velocity qualitative trends are the same and the quantitative differences are small. The good agreement between the analytical solution, the numerical predictions, and experimental measurements serve as an evidence for experimental validation of the analytical solution and CFD simulation predictions.

CHAPTER 5 HEAT TRANSFER MODELING

In this chapter, a heat transfer numerical model has been developed to study the heat flow during the friction extrusion process. The heat transfer model will be employed in a more comprehensive numerical model for further investigations. In this model the heat source is decoupled from friction or plastic deformation and the heat transfer phenomenon during friction extrusion process is investigated by a pure thermal model. As a first step, without material flow, it is more convenient to study the heat transfer phenomenon in friction extrusion process. The pure thermal model, as "pure" implies, means only heat transfer is simulated and the precursor material in the chamber and all tools are treated as solids. Only the equation of the conservation of energy is needed to solve. The goal of the pure thermal model is to obtain temperature fields, to know the temperature distribution, and to determine thermal boundary conditions.

Although the material flow is very strong in the friction extrusion process under the die-precursor interface, the pure thermal model is expected to capture the temperature field reasonably without consideration of material flow. There are three aspects that can account for it. First, the region with strong material flow under the die-precursor interface is small. That can be seen from the cross section of the remnant disk in the chamber after experiment as mentioned in Chapter 2. Second, in the strong material flow region, the tangential velocity is almost dominant due to high rotation speed of the die and the radical velocity is expected relatively small. As a result, the heat transfer due to material flow is mainly

radical. Third, the aluminum alloy 6061 has much higher heat conductivity so that the conduction heat transfer is dominant over the heat convection due to material flow.

To study the heat transfer phenomenon, heat generation source is always of interest. In friction extrusion process, the heat generation comes from two parts, i.e., the friction between the die and the precursor material in the chamber and material plastic deformation. So far, it is very difficult to determine the percentages of these two heat sources during the process and to know how they are distributed. Some simplifications or assumptions must be made. Numerical studies on the similar process, the friction stir welding process, as described in the literature review in Chapter 3, include interface influx on the friction interface, viscous dissipation, and combination of them [92]. The heat generation power is estimated based on yield stress or fitted by comparing experimental measurements. Since friction stir welding is a steady state process except the beginning and ending, by using these methods good approximations can be easily obtained. However, unlike friction stir welding process, friction extrusion process shows apparent transient state features for heat transfer. The heat generation power varies during friction extrusion process. Consequently, difficulties occur when adopting the methods used in friction stir welding to approximate the heat generation rate in friction extrusion process. To avoid such difficulties, the mechanical power during friction extrusion experiment can be used to relate the heat generation power. So in this pure thermal model, the heat generation rate is a function of the mechanical power. The details pertaining the pure thermal model are described in the following subsections.

5.1 Model Description

In order to capture the heat transfer phenomenon in the friction extrusion experiment, the heat transfer model considers all parts involved in friction extrusion process, such as the die, the chamber, the aluminum alloy sample, the back plate and the supporting table. Compared with the chamber and the sample, the die, the back plate and the table have relative larger sizes. Considering the relative large volumes of them and lower conductivities, it is expected that overall temperatures of them don't change much although the heat flows into them continuously. However, the temperature definitely increases drastically in the regions where it is close to the aluminum alloy sample. Apparently, it is not necessary to simulate the whole bodies. The faraway areas can be excluded since the temperature almost retains the same. Thus a lot of computing efforts can be saved. The sizes of the bodies of the die, the back plate, and the table included in the model should be chosen carefully so that they can represent the effect of the whole bodies. Various sizes of these parts are tried and their results are compared. The final sizes are determined if larger sizes would not affect the predictions pronouncedly. In addition, the temperatures of these select parts are not high, the predictions are not sensitive to the boundary conditions on the boundaries of the parts. Other than the mentioned approximations to the die, the back plate and the table, the actual geometrical dimensions of the experimental setup are used in the thermal model.

Similar to non-flow based thermal models for friction stir welding [90], this is a pure thermal model in which the material flow is not modeled. As such, considering the characteristics of the problem, such as the geometry, the governing equation, and the boundary conditions, a two-dimensional axisymmetric model is found appropriate for the

process. Utilization of the axisymmetry saves computing efforts significantly since only half of the cross-sectional area along the axis of symmetry is needed for the geometry.

The finite volume method is used to discretize the computational domain. The mesh is shown in Figure 5.1. The aluminum alloy has a radius of 12.75 mm. The final sizes for the back plate and the table are the same, 50 mm in radius. A grid with a cell size of 0.5 mm is used. The time step is 0.05 second. Convergence analysis has been conducted and the grid used in this work is converged. The commercial code ANSYS FLUENT is used to carry out the computations.

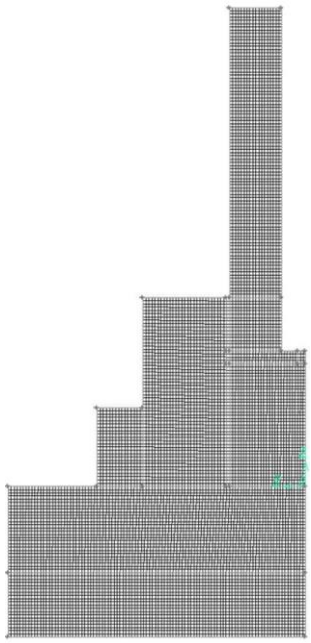

Figure 5.1 The thermal model grid.

Figure 5.2 A cross section of the remnant aluminum alloy sample after etching.

Since this is to study the heat transfer, the most key factor is heat generation. So the heat generation is first discussed. As in the work done by Schmidt et al. [92], three contact conditions are defined: sliding condition that the contact shear stress is smaller than the aluminum sample yield shear stress, sticking condition that the aluminum sample

surface sticks to the moving tool surface segment, and partial sliding/sticking condition that is a mixed state of the former two states. During the friction extrusion process, all these three contact conditions may happen. In the first few seconds, the sliding condition occurs because the yield shear stress of the aluminum sample is larger than the stress under the compression and torque. The z-force applied on the die is smaller in the first few seconds, which also makes it easily slide. The continued friction between the die and the aluminum alloy sample generates heat and temperature near the sliding interface increases fast. The rising temperature causes the decrease of the strength of the aluminum alloy sample locally. At a certain point, the strength lowers down to the friction stress, the second condition, i.e. partial sliding/sticking, occurs. After yield, the material has large plastic deformation. When the material at the interface becomes softer, the degree of sticking increases. Sticking or close sticking may happen when the material is soft enough at high temperature.

Obviously, both friction and plastic deformation happens during the friction extrusion process, and both of them generate heat. The heat generation in terms of friction is a surface heat flux and it is a volume flux for plastic deformation. In the pure thermal models of FSW without consideration of material flow, Chao et al. [92] used trial and error method to find total power input, Khandkar et al. [87] correlated mechanical power to heat generation, and Schmidt and Hattel [93] estimated heat generation only by a surface flux based on an assumption that the shear layer or deformation zone is very thin and uniform. The surface heat flux model works well for FSW. However, in the friction extrusion experiment, after the start of extrusion, the deformation zone or shear layer is not relatively thin. Experimental observations show that at the end of extrusion the thickness of deformation zone was about 4 mm on average compared with the height of sample 19 mm

in a friction extrusion experiment. Figure 5.2 shows a cross section of remnant of the aluminum alloy sample after experiment after etching. The thickness of the deformation area is not thin at all. Thus both a surface flux and a volume flux should be considered to model the heat generation in terms of friction and volume deformation respectively.

However, there are some difficulties if a surface heat flux is used in the numerical modeling, especially when the surface is the interface of two bodies, like the current work. First, it will introduce difficulties to boundary condition settings. When two bodies are in contact, the heat transfers between these two bodies through heat conduction. There may be thermal resistance at the interface. At the interface, it is thermally coupled. So the temperature contours are continuous and there is no jump. If the surface heat flux is used, the conduction heat transfer between the two bodies will be broken and both the two surfaces of the bodies must be assigned heat fluxes. In that case, it's not thermally coupled anymore and the temperature is not continuous. Clearly, the surface heat flux will bring temperature discontinuity in temperature sensitive area. Second, some assumptions are needed for the surface flux. There are two bodies, the die and the aluminum alloy sample, and the contact surfaces are assigned surface fluxes. This means the friction heat generation needs to be split into two parts. However, how to split is unknown and some assumptions must be made. Even more, the percentage of the frictional heat generation is not known. Third, if the surface heat flux is used, the distribution of heat generation rate on the surfaces needed to be determined. Usually, it is assumed that the friction coefficient is uniform. Then the friction heat generation over an infinitesimal interface area dA can be written as

$$dq = \eta P v' dA \tag{5.1}$$

where v' is the relative velocity, η is the friction coefficient, and P is the pressure. Thus, another assumption is needed.

To overcome the shortages and to avoid the difficulties, a volume heating method with compensation of the surface heat flux effect is proposed to approximate the heat generation. Compared with surface heat fluxes, the volume heat source doesn't have the disadvantages listed above. It is proposed that heat generation is represented by a volume heat source in a material layer in the sample under the interface where the material undergoes extensive flow and severe plastic deformation. The height of the layer is determined based on experimental observations of the material flow region in the sample. As described in Chapter 2, a thin marker wire was inserted into the sample in order to investigate material flow in friction extrusion. After the friction extrusion experiment, observations of marker material positions in the remnant of the sample in the chamber revealed that the depth of the material flow region in the remnant is about 4.5 mm at one third of the sample radius from the center and it is smaller near the edge of the sample. As an approximation, and for simplicity, a material layer next to the interface with a uniform height of 4 mm is taken as the layer with a volume heating source.

One common limitation of non-flow based thermal models, such as the present model and those in the literature for the related process of friction stir welding, is that the spatial distribution of the heat source must be approximated based on certain simplifications and idealizations. At this time, due to the lack of information from the friction extrusion literature, the heat source distribution in the present study is assumed based on considerations from the literature for friction stir welding and on observations of material flow patterns in friction extrusion process experiments, as discussed earlier.

First, it is noted that the radial distribution of frictional surface heat flux is often approximated by a linear distribution in the friction stir welding literature, resulting from the product between a shear stress created by a uniform tool pressure and a tangential velocity created by rigid tool rotation. For simplicity, and as a first order approximation, this linear distribution in the radial direction is adopted in the present study in the volume heat source method, since the volume heat source is in a region immediately adjacent to the die-sample interface.

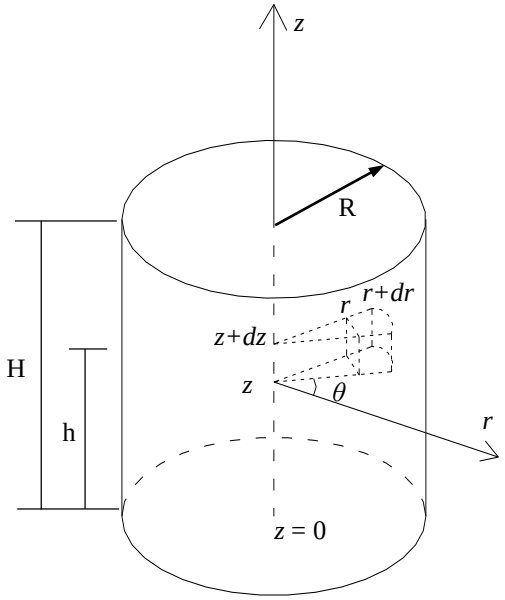

Figure 5.3 The sample geometry and coordinates.

Second, in the vertical direction (which is the axial direction of the cylindrical sample), it is expected that plastic deformation is greater closer to the die-sample interface, thus more heat is expected to be generated closer to the interface. In addition, the friction heat generation occurs at the interface. For simplification again, a linear distribution along the vertical direction is assumed for the volume heat source.

Based on the above simplifications, the heat generation rate in the volume heat source method can be expressed as below

$$q = m(z - h)r \tag{5.2}$$

where *m* is a power-related quantity to be determined, *q* is the volumetric heat generation rate, and *h* is the height of the sample without heat source (see Figure 5.3 for a schematic of the sample geometry and the coordinate system).

The total heat generation power can be obtained by integration over the volume heating layer from $z = h$ to $z = H$ (see Figure 5.3):

$$Q_{total} = \int_0^{2\pi} \int_0^R \int_h^H q \cdot rdzdrd\theta = \int_0^{2\pi} \int_0^R \int_h^H mr(z - h) \cdot rdzdrd\theta = \frac{1}{3} m\pi (H - h)^2 R^3 \tag{5.3}$$

In the current thermal model, Q_{total} is set to equal to the mechanical power input in the friction extrusion experiment, which was recorded in the experiment as a function of time.

From equation (5.3), the quantity *m* can be determined, which can be substituted into equation (5.2). Finally, the volumetric heat generation rate per unit volume is given by

$$q = \frac{3Q_{total}}{\pi (H-h)^2 R^3} r(z - h) \tag{5.4}$$

This expression is implemented into the code ANSYS FLUENT through a user defined function.

In the model it is assumed that all of the mechanical work is dissipated in the billet, i.e. the aluminum alloy sample, thereby contributing to heating of the billet. This is justified based on the following:

1. The extrusion apparatus does not deform plastically during the process, all deformation, hence heating, occurs in the billet.

2. The primary mechanism of storage of deformation energy in metals is the production of dislocations. In a highly deformed material, the maximum expected dislocation density is on the order of $10^{16}/m^2$. The maximum possible total stored deformation energy in the billet is then, the product of the billet volume, the dislocation density, and the dislocation line energy. For the present situation, this equates to approximately 77 J while the total energy input during the simulation is on the order of 80 KJ.
3. Evidently, the maximum possible stored deformation energy is a small fraction of the mechanical work supplied. Additionally, previous work has demonstrated that the extruded wire and the remaining billet material are in a fully recrystallized condition indicating that the stored dislocation energy will be much less than the maximum.

Therefore, for the present experiment (and likely most any other friction extrusion experiment) it is justified to assume that all of the mechanical work contributes to heating.

5.2 Governing Equations

Numerical simulations are using numerical methods to solve governing equations under certain boundary conditions. The considerable development of numerical methods enables accurate predictions about field variables, such as stress, strain, velocity, temperature, material path lines, etc., if boundary conditions are known or estimated properly. In numerical modeling, the description of motion is chosen depending on the problem solved. The governing equations may be not same for a different choice. For heat transfer problem, if there is not material flow, the heat is transferred in solids or fluids in the form of diffusion or conduction. The current pure thermal model is an example. The

governing equation is the conservation of energy. According to the first law of thermodynamics, the sum of work and heat in a system results in the change of the energy of the system. With indicial notation (i = 1, 2, and 3) the equation can be expressed in Cartesian coordinates as

$$\rho c_p \frac{\partial T}{\partial t} = \frac{\partial}{\partial x_i}\left(k \frac{\partial T}{\partial x_i}\right) + q \tag{5.5}$$

where ρ is density, c_p is the specific heat, k is conductivity, x_i are coordinates, and q is heat generation source given by equation (5.4). For a two-dimensional axisymmetric problem, the transient conduction equation can be written as

$$\frac{1}{r}\frac{\partial}{\partial r}\left(kr \frac{\partial T}{\partial r}\right) + \frac{\partial}{\partial z}\left(k \frac{\partial T}{\partial z}\right) + q = \rho c_p \frac{\partial T}{\partial t} \tag{5.6}$$

where r and z are the coordinates.

5.3 Initial and Boundary Conditions

Numerical simulations are to solve governing equations, which must be satisfied everywhere inside the computational field, combined with some constitutive relations of the materials and certain initial and boundary conditions by numerical methods such as finite element methods and computational fluid dynamic methods. Usually the reliability of the results of numerical simulations depends on the initial and boundary conditions given that the current computer is powerful and numerical methods have obtained good developments. If the initial and boundary conditions imposed in the numerical modeling represent the real ones, the numerical predictions can be very accurate for some problems. So does the heat transfer problem to be solved in current work.

There are three different modes of heat transfer, the conduction, the convection, and the radiation. Heat transfer by conduction arises from temperature gradient in a material or between materials. In the current work, conduction is the mode in the system.

When two solids are put together, heat transfer between them through conduction may not be perfect as in a single body. There is thermal resistance between them due to not perfect contact. The convection is the heat transfer between a solid surface and the adjacent fluid medium. If the fluid is flowing, it is forced convection and the heat transfer is quicker. The heat transfer rate can be expressed by

$$q' = h_c \Delta T \tag{5.7}$$

where q' is the heat transfer rate, h_c is the convection coefficient, and ΔT is the temperature difference between the solid body and the adjacent fluid. The radiation occurs between two objects which are placed in a finite distance apart. As if there is temperature difference between the two objects, there is radiation between them. The heat transfer rate through radiation is given by

$$q' = \epsilon \beta (T_1^4 - T_2^4) \tag{5.8}$$

where ϵ is the emissivity, β is the Stefan-Boltzmann constant, and T_1 and T_2 are the objects' temperatures. In this work, since the estimated radiation rate is very small compared with the mechanical power, the radiation is neglected in the modeling.

At the beginning of the friction extrusion process experiment, the temperature of all parts was the same as the lab room temperature, so the initial condition in the thermal model is set at the lab room temperature of 295 K.

When the temperatures of the extrusion chamber, the die, and the back plate increase, a part of the heat will flow into the air through convective heat transfer on the surfaces which are exposed to the air. In the model, a convection boundary is used to model such heat transfer. The convection coefficient for surfaces which are stationary in the process is 5 W/m^2-K, which is the typical value for natural convection between carbon

steel and air. For the moving surfaces, such as surfaces on the rotating die, two times the typical value is used as an approximation to account for forced convection heat transfer.

In order to model the heat transfer process realistically, the back plate and the table under the back plate are considered in the thermal model, as discussed earlier. Convection boundary condition is also used on the outer surfaces of the back plate and the table. The value used in the model is 10 W/m^2-K. The dimensions of the back plate and the table included in the thermal model are selected after a careful study of their effects. It is found that, if the thickness of the table and the radial length of the back plate and the table in the model are large enough, the model predictions are insensitive to the convection coefficient value on the outer surfaces of the back plate and the table. Thus the assumed convection boundary condition has little effect on the temperature field.

The connections between the sample and the back plate, between the chamber wall and the back plate, and between the back plate and the table are taken to be perfect without any thermal resistance. That is, these parts of the thermal system are considered thermally coupled and in perfect contact. This approximation is reasonable due to the fact that during the extrusion experiment the sample was under high pressure exerted by the extrusion die, and that the chamber wall was tightly clamped on the back plate for prevention of slippage between them.

The situation of contact between the sample and the chamber wall in the friction extrusion experiment is more complicated. In the experiment, the sample and die diameter was slightly smaller than the chamber inner diameter, so there was no friction between the die and the chamber inner wall. However, there was a thin gap between the aluminum alloy sample and the chamber inner wall, which was initially filled with air. The gap with air

could block heat transfer from the sample into the chamber wall. After the start of the extrusion, the temperature and pressure in the sample increased drastically, and then a part of the sample material was forced to flow into the gap according to experimental observations. During the friction extrusion experiment, some material extruded out from the gap was observed. Subsequently, the part of the gap where it was filled with the sample materials made the heat transfer between the sample and the chamber wall easier. When the experiment was finished, the gap was found to be completely filled by the sample material based on experimental observations. The gap is expected to be filled up gradually. However, the exact process through which the gap was filled is unknown and cannot be determined in this pure thermal model. Nevertheless, the time when the gap started to be filled in the experiment can be determined from recorded experimental data.

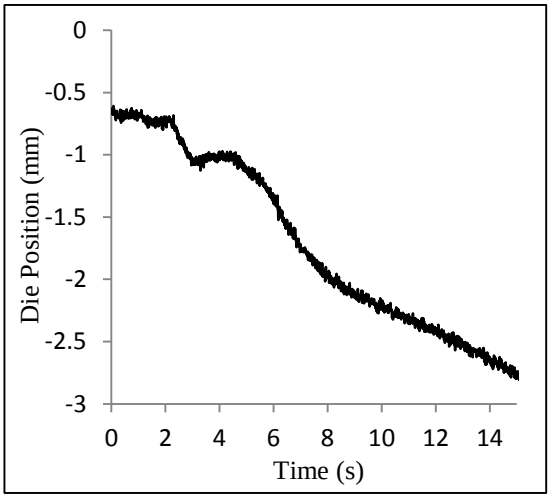

Figure 5.4 Die position.

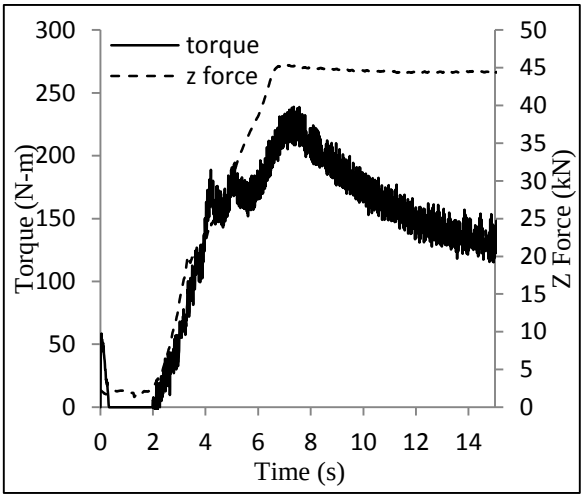

Figure 5.5 Torque and z force.

Figure 5.4 shows the die position as a function of time during the friction extrusion experiment. In the first three seconds, the die moved downward from about 0.25 mm above the top surface of sample. In the next period of t = 3 – 4.7 s, the die almost stayed at the

same position. Then after t = 4.7 s, the die moved downward again. Figure 5.5 illustrates the z force and the torque applied on the die, respectively, during the experiment. The non-zero torque value in the first 0.2 s is meaningless due to a system bug which started to record data from the end of the previous experiment. It is observed that the force and torque both increased with time. In order to determine when the sample began to flow into the initial gap between the sample and the chamber inner wall, an approximate analysis of the stress state (see Figure 5.6) in the sample has been conducted. The normal and shear stresses, σ_z and τ, can be approximated as follows

$$\sigma_z = \frac{z\ force}{A}, \tau = \frac{2 \cdot torque}{\pi R^3} \tag{5.8}$$

where A and R are the cross section area and diameter of the cylinder, respectively.

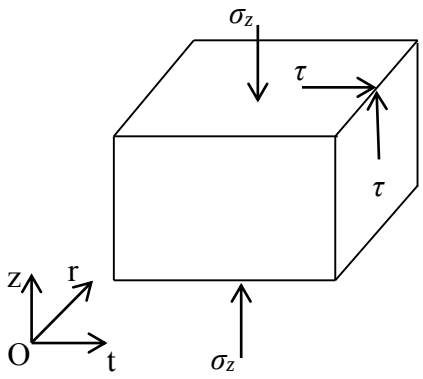

Figure 5.6 Stress state (z-vertical direction, r-radial direction, and t-tangential direction).

Based on the equations and data, the stresses at different times can be estimated. At t = 3 s, the z direction stress was σ_z = -28.3 MPa and the maximum shear stress on the cross section occurred at the edge of the sample cylinder and it was about τ_{max} =18.7 MPa. Thus the maximum effective stress was σ_e = 53.9 MPa. The highest temperature is estimated at

323 K at that moment according to the temperature measurement at point 2, which was 305 K. The yield stress for sample (AA 6061) is more than 200 MPa at 323 K, so that the sample material was not yielded yet at t = 3 s. Accordingly, during the period of t = 0 – 3 s, the die movement did not cause the sample material to flow into the gap since there was no yielding.

At t = 4.7 s, the z direction stress was σ_z = -54.9 MPa and the maximum shear stress on the cross section occurred at the edge of the sample cylinder and it was τ_{max} =55.3 MPa. Thus the maximum effective stress was σ_e = 146.2 MPa. The estimated highest temperature is 573 K based on the temperature measurement at point 2, which was 497K at which the yield stress is less than 138 MPa. At this moment, a part of the sample material began yielding. Thus, it is seen that the die movement began to force the sample material to flow into the gap from t = 4.7 s.

Table 5.1 Material Properties

Name	Material	Density (kg/m^3)	Specific Heat (J/kg-K)	Thermal Conductivity (W/m-K)
Sample	AA 6061	2,700	789.9+0.4959T	115.2+0.1594T
Die	H13 steel	7,800	460	25
Chamber Wall	O1 steel	7,800	460	33
Back Plate	Al6xn steel	7,800	500	13
Table	Carbon Steel	7,800	500	50

Again, since the current thermal model does not consider material flow nor elastic-plastic deformation of the sample material, the exact manner in which the initial gap between the sample and the chamber inner wall was filled cannot be determined. However, based on the above estimates of the stress state, it is approximated in the thermal model

that the gap was filled gradually from t = 4.7 s to the start of extrusion of the wire at t = 10 s.

5.4 Material Properties

The range of temperature variation in the friction extrusion experiment was large, approximately from 295 K to 848 K. The thermal properties of aluminum alloy are sensitive to temperature variation, and thus temperature-dependent thermal properties are considered in the thermal model. The materials and their properties used in the model are listed in Table 1 based on data from reference [97].

5.5 Results and Discussions

5.5.1 Measurements and Validation

In the extrusion experiment, temperature variations were recorded at designated locations using thermal couples. The measured temperature variations with time are plotted in Figure 5.7. For validation purposes, temperature variations at the same locations that are predicted by the thermal model are also shown in Figure 5.7. At t = 0, the die began to rotate and there already was a vertical force of 2.2 kN exerted on the sample. The extrusion of the wire started at about t = 10 second and ended at t = 27.7 s.

Generally, the comparisons show a good agreement between predicted and measured temperature variations with time. Point 2 was in the extrusion die near the die/sample interface. It can be seen from Figure 5.7(a) that the predicted temperature variation at point 2 matches the experimental measurement very well, which indicates that the heat transfer between the die and the sample has been modeled accurately. For the predictions at points 3, 4, and 5, illustrated in Figure 5.7(b), there are small discrepancies with experimental measurements. That might be caused by the uncertain effects of the

initial gap between the sample and the chamber wall. The temperature variation at point 8, shown in Figure 5.7(c), has a more noticeable discrepancy between the predictions and the experimental measurements in the period when the temperature began to rise. The predicted temperature is higher than the measured value during that period. The most possible reason for the mismatch is that the contact between the sample and the back plate was imperfect in the experiment, while it is assumed to be perfect in the thermal model. There may be thermal resistance between the back plate and the sample.

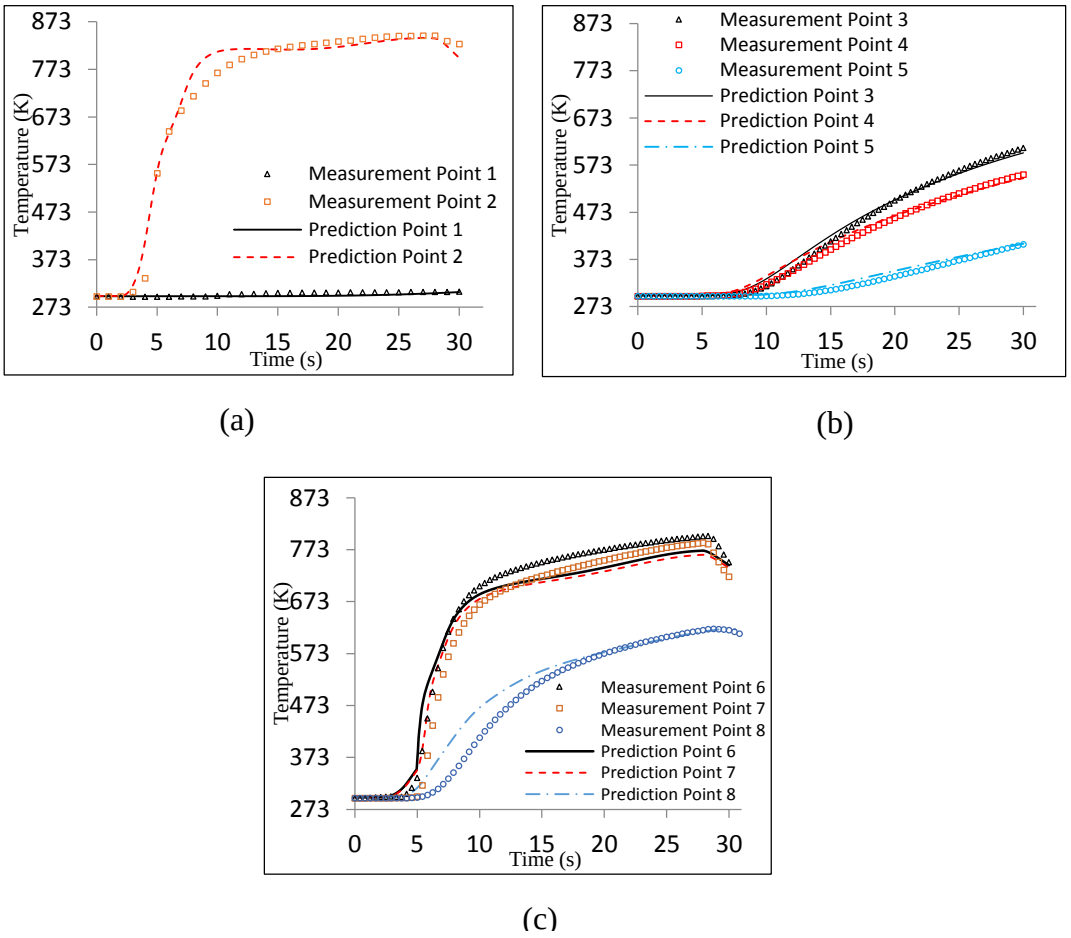

Figure 5.7 Comparisons between temperature predictions without the consideration of the thermal resistance effect and experimental measurements for (a) points 1 and 2, (b) points 3, 4, and 5, (c) points 6, 7, and 8.

In order to confirm the thermal resistance, a simulation with every setting the same except changing the conductivity of the back plate has been conducted. Changing the conductivity of the back plate from a small value to its normal value, from the beginning to the start of extrusion, is to model the thermal resistance. The predicted temperature variations are compared with the experimental measurements again, as shown in Figure 5.8. It is seen that a good agreement can be observed for point 8, indicating the thermal resistance is properly modeled. For other points, the predictions are almost the same as those in the first simulation.

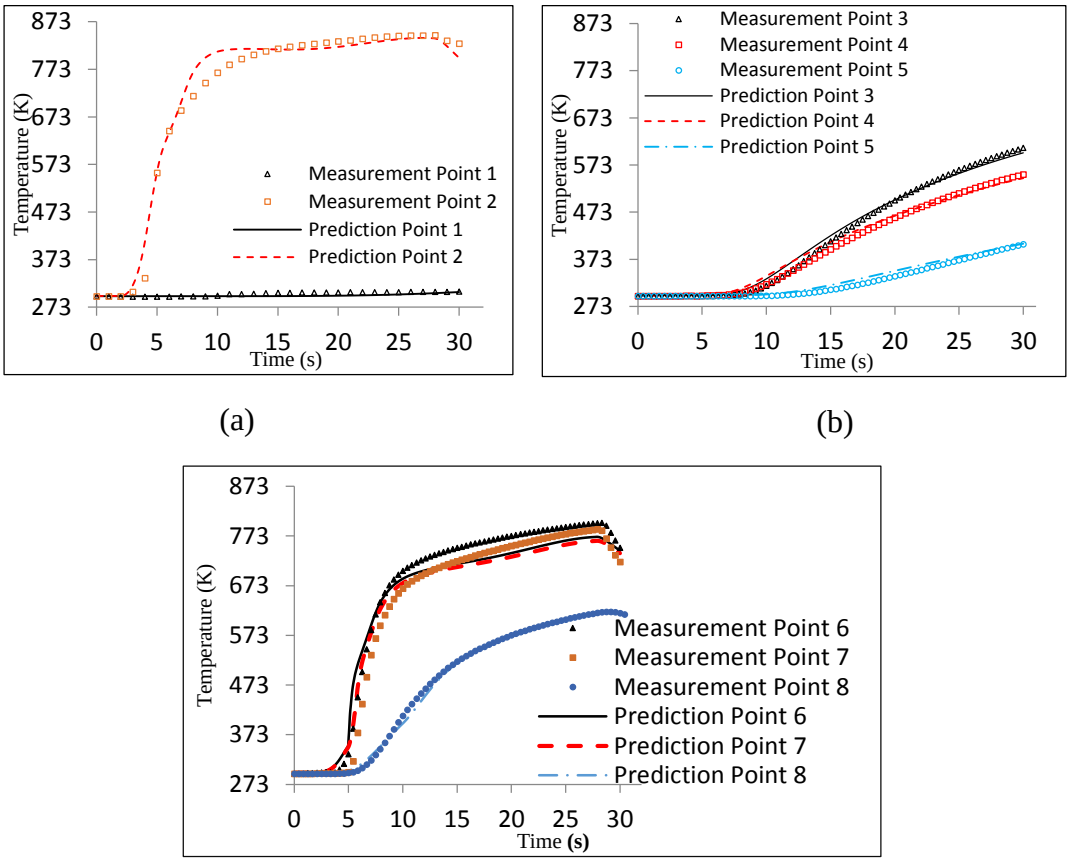

(a) (b)

(c)

Figure 5.8 Comparisons between temperature predictions with the consideration of the thermal resistance effect and experimental measurements for (a) points 1 and 2, (b) points 3, 4, and 5, (c) points 6, 7, and 8.

Overall, from the comparisons above, a very good agreement between numerical predictions and experimental measurements is observed. The good agreement indicates that the heat generation is properly approximated and the temperature field can be reasonably predicted by the pure thermal model. For the rest of this work, the results from the model with thermal resistance effect are used if it is not indicated.

5.5.2 Temperature Field Features

For convenience of discussion, the thermal couple points are divided into three groups according to their locations: (1) group 1 includes points 2, 6, and 7, which are located close to the heat source zone; (2) group 2 includes points 1, 3, 4, and 5, which are farther away from the heat source zone; and (3) group 3 includes only point 8.

In the first three seconds during the experiment, the temperatures at all thermal couple points changed little since the die rotation speed was low and thus the heat generation rate was small. In the next few seconds but before the wire was extruded, the temperature at group 1 points increased drastically. The reason for this phenomenon is that the positions of group 1 points were close to the volumetric heat source zone, leading to a quick temperature rise. The points in group 2 show a slower temperature rise, because they were farther away from the heat source and it took more time to transfer heat to these points. For point 8 in group 3, although it was also far from the heat source zone, the material between point 8 and the heat source zone was aluminum alloy (instead of steel as in the chamber wall), which has a much higher thermal conductivity than steel, so that heat could be carried to point 8 more quickly than to points in group 2 (but slower than to points in group 1 due to the much greater differences in distance).

After 10 seconds, the temperature continued to increase but still in different ways at points in different groups. In group 1 the temperature obviously increases slowly. At the end of extrusion, the temperature at point 2 was very near but never attained the solidus temperature of aluminum alloy 6061, which is physically reasonable. As the temperature increased gradually after the extrusion of wire started, the aluminum alloy became softer near the rotating interface and thus was easier to be extruded out to form a wire. Also, the level of both the friction between the extrusion die and the aluminum alloy and the plastic deformation decreased since the aluminum alloy became softer due to temperature rise. As a result, the total heat generation decreased correspondingly, as shown in Figure 5.9. Heat was conducted away from the heat source zone continually and at the same time the temperature in group 2 increased almost linearly.

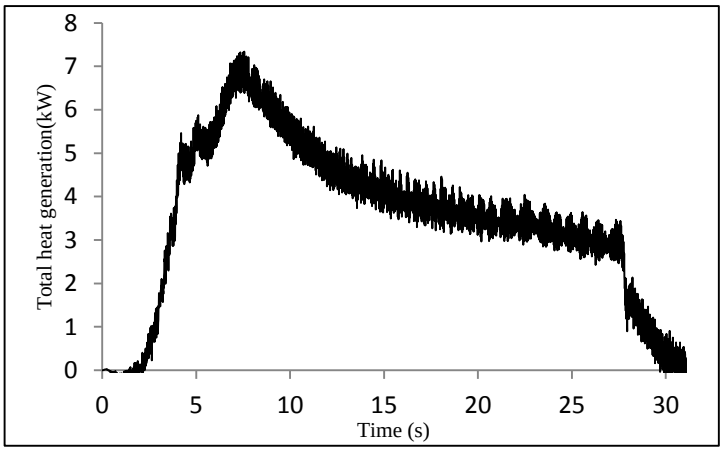

Figure 5.9 Mechanical power in the experiment.

At the end of the extrusion when the die lost contact with the aluminum alloy, the temperature at point 2 began to drop immediately. The loss of contact resulted in decreased heat generation and loss of heat transfer to point 2. At points 6 and 7, because the

temperature was lower than that in the heat source zone and thus there was still heat transfer from the heat source zone to points 6 and 7, the temperature here did not decrease immediately after the end of extrusion but it did decrease later, as shown in Figure 5.8(c). Similarly at other points, the temperature continued to rise because heat was still being transferred from high temperature regions to these points.

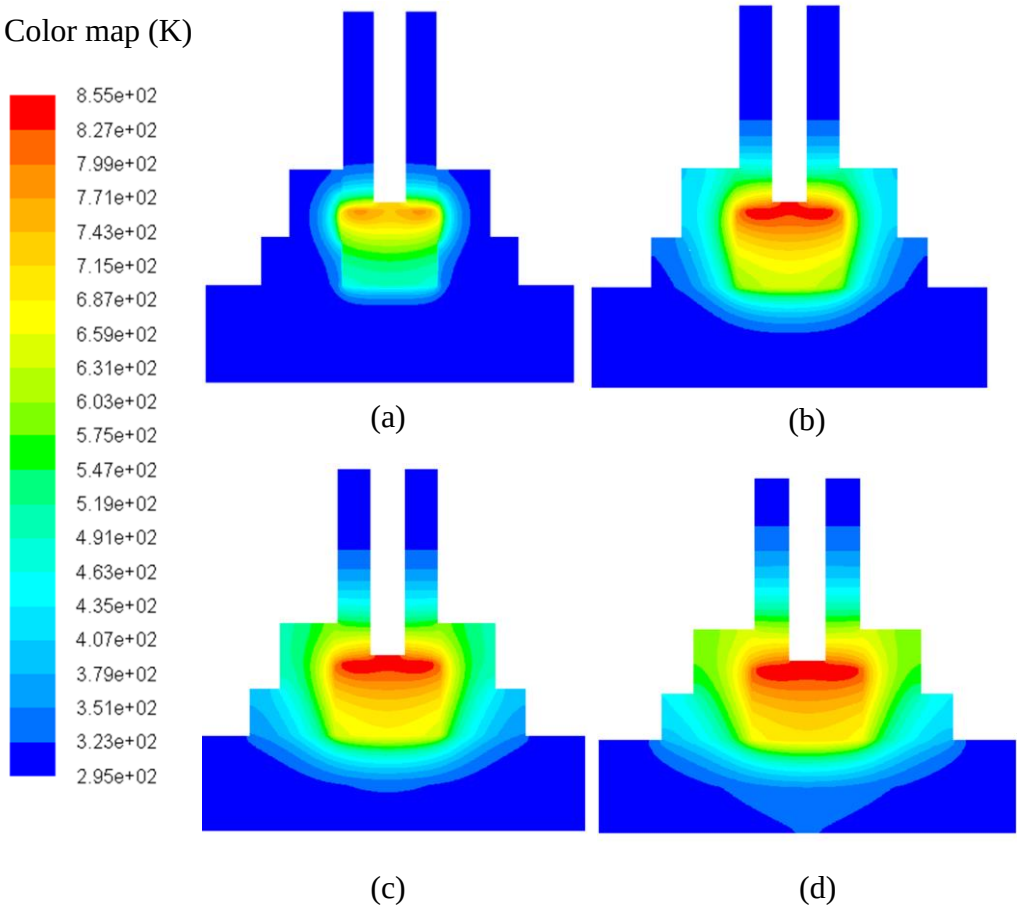

Figure 5.10 Predicted temperature contours at (a) t = 7s, (b) t = 14s, (c) t = 21s, (d) t = 27.7s.

Figure 5.10 presents the contour graphs of the temperature field on the entire cross section of the thermal system (they were created by mirroring the model predictions from one half of the cross section to the other half) at several instants in the friction extrusion

process. Figure 5.10 (a) shows the temperature field at t = 7 s. Apparently, the heat source region had higher temperatures due to the fact that heat generation occurred from there. At this moment, only a part of the initial gap between the sample and the chamber wall was filled with the hot sample material from near the die/sample interface. Consequently, heat was conducted through the partially filled gap into the nearby chamber wall, and as a result the temperature was higher in the region of the chamber wall that is close to partially filled gap. At the same time, the lower part of the gap, which was still unfilled, blocked the heat transfer from the heated sample to the chamber wall, so the temperature was much lower in that part of the chamber wall. Because of the perfect contact between the sample and the back plate in the thermal model, heat flowed into the back plate without obstruction. However, the back plate has a much lower thermal conductivity (see Table 5.1) than the sample (AA 6061), so that heat did not flow deeply and quickly into the back plate and the temperature rise there was limited to the sample-back plate interface region.

Figure 5.10 (b) gives the temperature contours at t = 14 s. At that instant, the gap between the sample and the chamber wall had been filled completely so that heat flow into the chamber wall was not blocked anymore and temperature rise in the chamber wall was now more evident. The temperature near the sample-die interface was pronouncedly high since it is close to the heat generation heat source. The die also has a relatively low thermal conductivity compared with the sample, so that heat transfer into the die did not go very deep and the temperature rise in the die is limited to the sample-die interface region.

Figure 5.10 (c) and (d) show how the temperature field was developed at t = 21 s and 27.7 s, respectively. Obviously, heat flowed from the sample into the chamber wall continuously with ease since the gap between the chamber wall and the sample had been

completely filled. Correspondingly, the temperature in the chamber wall rose continuously. The region below the die/sample interface always had the highest temperatures and the material in this region was the source of the subsequently extruded wire. It is also clearly shown that heat flowed into the die slowly.

From the model predictions, it can be seen that the highest temperature is about 848 K, which occurred at the end of the extrusion and at a location within the heat generation zone. This highest temperature was below the aluminum alloy's solidus temperature of 855 K, so that melting did not occur. It is consistent with experiment observation that there is no defects or voids in the remnant sample that indicate melting.

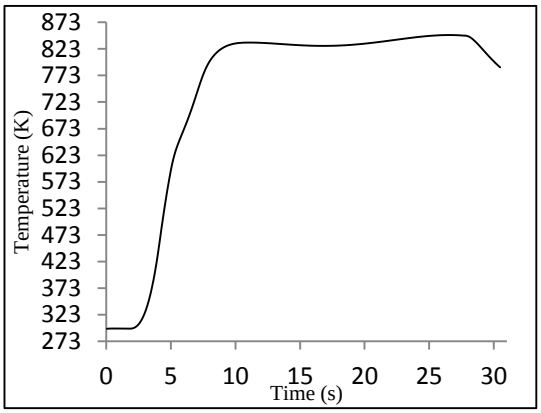

Figure 5.11 The predicted highest temperature variation near the hole.

5.6 Predicted Highest Temperature Variation

The highest temperature that the extruded wire experiences is of great interest since it is expected to play an important role in determining the mechanical properties of the extruded wire. Figure 5.11 depicts the predicted highest temperature variation near the extrusion hole. The predictions show that the temperature at the extrusion hole increases

rapidly and then changes little after the start of wire extrusion, which is very similar to the temperature measured experimentally at point 2. After the start of wire extrusion the temperature at the extrusion hole varies from 833 K to 848 K. At the end of the extrusion, the temperature at the hole is 848 K, which is very close to the solidus temperature of 855 K.

5.7 Summary and Conclusions

A pure thermal model has been developed to study the heat transfer phenomenon during friction extrusion process in this chapter. The heat generation in friction extrusion process is approximated by a volume heating model. A material layer under the die-sample interface is chosen as a heat source zone. The total power input is related to the mechanical power in the experiment. Only heat transfer is simulated and no material flow is considered. All bodies involved in the experiment are modeled in the simulation and some of them have smaller geometry sizes. The gap between the sample and the die is modeled by changing material conductivity.

The temperature predictions from the thermal model agree well with the experimental measurements, thus providing a good validation of the proposed thermal model. From the results of this study, it can be concluded as follows

1. The volume heating method can be used to reasonably represent the heat source in the friction extrusion process.
2. The initial gap between the sample and the chamber wall needs to be modeled in order to properly capture the heat transfer phenomenon.

3. The thermal contact between the billet charge sample and the back plate is not perfect based on comparisons between predictions and experimental measurements, and its complication needs to be studied further.
4. The extruded wire experienced a small range of temperature history during extrusion that varied in a small range somewhat below the solidus temperature.

CHAPTER 6 THERMO-FLUID MODELING OF THE FRICTION EXTRUSION PROCESS

So far, the friction extrusion process has received little attention and development since it was invented until recently. Tang and Reynolds [3] were the first researchers who published studies about friction extrusion process. In their work, they conducted a series of experiments with aluminum alloy chips at several die rotation rates. They tested the extruded wires on several aspects, such as microstructure, hardness and bend ductility. They concluded that defect free and good quality wires can be directly produced by friction extrusion process and limits on the process is related to extrusion temperature. Zhang et al. [129] studied the friction extrusion process on material flow. At first, a simplified model without extrusion was analyzed through analytical solution, numerical simulation and experiments with transparent fluid as presented in Chapter 4. Next a numerical modeling was conducted to study the material flow features. Since no experimental data was available for temperature field at that time, only flow fields were discussed. Zhao et al. [130] performed a physical modeling of friction extrusion process using a transparent fluid and digital image correlation to track the motion of tiny solid particles in the fluid. Zhang et al. [131] investigated the heat transfer phenomenon in friction extrusion process by a pure thermal model as reported in Chapter 5. A volume heating model was proposed to approximate the heat generation during friction extrusion. It was assumed temperature field is affected little by material flow field so the flow field was not considered. The temperature predictions have a very good agreement with experimental measurements. Experimental

studies were presented by Li et al. [132, 133] on friction extrusion process with aluminum alloys. A marker insert technique was used to obtain the material deformation and distribution. However, information about the distribution of marker material in the chamber could hardly be obtained due to invisibility.

The previous studies pertaining to friction extrusion process, either focusing on material flow but without validated temperature field [129], or concentrating on heat transfer without consideration of material flow [131], or presenting experimental measurements and observations only [3, 132, 133], none of them provide an understanding from a comprehensive model that considers both heat transfer and material flow both of which are involved in friction extrusion process. That also leaves a bunch of questions waiting answers, such as (1) will the volume heating model still work if material flow field is considered? (2) what is the material flow field like if validated temperature filed is applied? (3) how the marker material is distributed in the process chamber during the process? and (4) how the material deforms before it is extruded out to form a wire? To answer these questions, a more comprehensive model that includes more details and less simplifications and assumptions is needed.

The objective of this chapter is to develop such a more comprehensive numerical model of friction extrusion process that combines both heat transfer and material flow which exist simultaneously in the process. The relation between temperature field and material flow field during friction extrusion process is complicated. As other processes involving large deformations, like friction stir welding and traditional extrusion process, heat generation comes from both viscous dissipation and friction between workpiece and tools [97, 125, 134]. Before the temperature gets high, little plastic deformation happens

and the heat generation mainly comes from friction. The metal becomes softened when temperature is high due to continued frictional heating and plastic deformation or material flow occurs easily. As long as a part of material sticks to the rotating die, the frictional heating decreases and plastic dissipation increases. The sticking and high temperature result a zone where the material has prominent velocity. As is seen, the temperature field and material flow field are coupled because they affect each other. Ideally, the two phenomena should not be decoupled in numerical simulations. However, at current stage, it is very hard to implement heat transfer and material flow coupling due to some difficulties, such as inaccurate material constitutive models at high temperature and strain rates and some uncertainties about boundary conditions. A better choice is to adopt a thermal model that is an approximation of the heat generation during the process based on analytical solutions combined with some reasonable assumptions. In the study of friction stir welding which shares a lot of similarities with friction extrusion process, it is popular to use pure thermal models to study the heat transfer [87, 90, 92] and to adopt the thermal models in material flow modeling [94, 105, 106, 113, 114, 123]. Good agreements with experimental measurements can be observed for these models. This method is also chosen in the current work and the thermal model in the heat transfer modeling in Chapter 5 is adopted. However, the temperature field will not be the same because the material flow affects heat transfer more or less. The material flow can be modeled in either a solid way or a fluid way. In order to avoid the difficulties caused by large material deformations, the current work uses the CFD method so it is a thermo-fluid model.

6.1 Governing Equations

Since this is a thermo-fluid model, both temperature and velocity fields need to be solved although they are not coupled. For the velocity field, the same continuity equations in Chapter 4 are used and they are given below for completeness.

$$\frac{\partial v_i}{\partial x_i} = 0 \tag{6.1}$$

The Navier-Stokes equations, which are derived from Newton's second law of motion in form of momentum, for transient incompressible fluid flow are written as

$$\rho \frac{\partial v_j}{\partial t} + \rho v_i \frac{\partial v_j}{\partial x_i} = -\frac{\partial P}{\partial x_j} + \frac{\partial}{\partial x_i}\left(\mu \frac{\partial v_j}{\partial x_i}\right) + F_j \tag{6.2}$$

where v_i are velocity component and F_i are body force components.

Since there is material flow, the governing equations are a little different from these for the pure thermal model. The material flow causes heat convection in the fluid. The conservation of energy can be expressed by

$$\rho c_p \left(\frac{\partial T}{\partial t} + v_i \frac{\partial T}{\partial x_i}\right) = \frac{\partial}{\partial x_i}\left(k \frac{\partial T}{\partial x_i}\right) + \Psi + q \tag{6.3}$$

where q is heat generation rate per volume and Ψ is the viscous dissipation due to material flow, a heat generation source. The viscous dissipation function is expressed as follows

$$\Psi = \mu\left[2\left(\frac{\partial v_1}{\partial x_1}\right)^2 + 2\left(\frac{\partial v_2}{\partial x_2}\right)^2 + 2\left(\frac{\partial v_3}{\partial x_3}\right)^2 + \left(\frac{\partial v_1}{\partial x_2} + \frac{\partial v_2}{\partial x_1}\right)^2 + \left(\frac{\partial v_3}{\partial x_2} + \frac{\partial v_2}{\partial x_3}\right)^2 + \left(\frac{\partial v_1}{\partial x_3} + \frac{\partial v_3}{\partial x_1}\right)^2\right] \tag{6.4}$$

From the above equation, it is seen that the viscous heating is directly related with velocity gradients. In friction extrusion process, large velocity gradients happen near the die/sample interface. Thus it is expected that a large proportion of heat generation comes from the vicinity of the interface where strong material flow occurs.

6.2 Constitutive Models

The most familiar aspect of a fluid's properties for us is it can flow with shape changing. Some fluids are easy to flow and some don't. The difference is related to a fluid property called the viscosity, which was first described by Newton. Take an example to explain the viscosity. Consider two parallel plates filled with a fluid between them. Set one plate in motion with respect to the other at a low constant velocity. The force per unit area to keep the motion of the plate is

$$\frac{F}{A} = \tau = \mu \frac{V}{\Delta L} = \mu \dot{\varepsilon} \tag{6.5}$$

where τ is the shear stress in the direction of motion on a fluid surface at a distance ΔL from the moving plate, μ is a proportionality, called the viscosity, and $\dot{\varepsilon}$ is the strain rate or rate of shear in the fluid. For some fluids, such as water and other pure liquids, the viscosity doesn't depend on the strain rate and they are called Newtonian fluids. But some fluids, such as suspensions of solids in liquid and softened metals, are not Newtonian fluids. However, equation (6.5) is still used to characterize their properties with the viscosity as a function of the strain rate. They are called non-Newtonian fluids.

To solve the governing equations, the most important thing is to define the constitutive equations for the materials. For fluid-based modeling, the Eulerian description of motion is used, meaning the material particles go through mesh grids which are fixed in the space. The field variables include velocity and pressure. The viscosity appears in the Navier-Stokes equations so the constitutive equation needed is for the viscosity. It is important to point out that the strain is not available directly in fluid modeling and difficulties emerge if the viscosity is strain dependent. Many researchers have studied the constitutive equations by proposed mathematical models through experimental tests. There

are numbers of different types of mathematical models even for a same material. Suitable constitutive models should be chosen based one the problem to be solved. The following sub-sections will focus on the constitutive models chosen for the numerical simulations in this work.

For a fluid, beside the material properties like density, thermal conductivity, and specific heat, viscosity is indispensable during numerical modeling of flow. For a regular fluid, the viscosity can be measured directly through experiments. But for a solid, usually there is no way to measure it directly. In general, the constitutive equation of a solid is the stress-strain curve obtained from uniaxial tension test. For some aluminum alloys, such as AA6061, show visco-platic characteristics, which are rate-dependent inelastic behavior of solids, and the flow stress is dependent on temperature and strain rates under large deformations. The material flow is in a viscous manner when large deformations occur under visco-plastic conditions and the elastic deformations are negligible compared with total deformations. For a solid under large deformations, correlating the flow stress with the viscosity is one way to simulate the flow of the material.

For a viscous, incompressible fluid, the constitutive relation can be written in the form with index notation (i, j, and k represent x, y, and z coordinates, respectively in three-dimensional Cartesian coordinate system) as follows

$$\sigma_{ij} = -P\delta_{ij} + 2\mu\dot{\varepsilon}_{ij} \tag{6.6}$$

where σ_{ij} are stresses, $P = -\sigma_{ii}/3$ is the mean stress, and $\dot{\varepsilon}_{ij}$ are the strain rate components. From equation (6.6), the strain rates can be written as

$$\dot{\varepsilon}_{ij} = \frac{1}{2\mu} s_{ij} \tag{6.7}$$

where s_{ij} are deviatoric stress components.

For a solid behaving visco-plastic characteristics under large deformation, the constitutive relation can be written [46]

$$\dot{\varepsilon}_{ij} = \frac{1}{\bar{\mu}} < F > \frac{\partial F}{\partial \sigma_{ij}} \tag{6.8}$$

where $\bar{\mu}$ is a constant 'pseudo-viscosity', $F = F(\sigma_{ij})$ is a yield function. When $F = 0$ it is plastic yield condition. $< F >= F$ if $F > 0$ and $< F >= 0$ if $F \leq 0$. If the von Mises criterion is chosen, the yield function becomes

$$F = \sqrt{\frac{1}{2} S_{ij} S_{ij}} - \frac{1}{\sqrt{3}} \sigma_e \tag{6.9}$$

where σ_e is the flow stress obtained from uniaxial test. Then

$$\frac{\partial F}{\partial \sigma_{ij}} = \frac{1}{2} \frac{1}{\sqrt{\frac{1}{2} S_{ij} S_{ij}}} S_{ij} \tag{6.10}$$

If plastic deformations occur, namely $F > 0$, impose equations (6.9) and (6.10) into (6.8) and use (6.7), we can get

$$\frac{1}{\mu} = \frac{1}{\bar{\mu}} \frac{\sqrt{\frac{1}{2} S_{ij} S_{ij}} - \frac{1}{\sqrt{3}} \sigma_e}{\sqrt{\frac{1}{2} S_{ij} S_{ij}}} \tag{6.11}$$

From equation (6.7),

$$\sqrt{\frac{1}{2} S_{ij} S_{ij}} = \mu \sqrt{3} \sqrt{\frac{2}{3} \dot{\varepsilon}_{ij} \dot{\varepsilon}_{ij}} = \sqrt{3} \mu \dot{\bar{\varepsilon}} \tag{6.12}$$

where $\dot{\bar{\varepsilon}}$ is an effective strain rate and its expressed by

$$\dot{\varepsilon}_{ij} = \frac{1}{2} \left(\frac{\partial v_i}{\partial x_j} + \frac{\partial v_j}{\partial x_i} \right) \tag{6.13}$$

where v_i are velocity components. Inserting equation (6.12) into (6.11) and changing the form, an equivalent viscosity is finally obtained

$$\mu = \frac{3 \bar{\mu} \dot{\bar{\varepsilon}} + \sigma_e}{3 \dot{\bar{\varepsilon}}} \tag{6.14}$$

For ideal plastic flow, $\bar{\mu}$ tends to infinity and (6.14) becomes

$$\mu = \frac{\sigma_e}{3\dot{\bar{\varepsilon}}} \tag{6.15}$$

Since the viscosity is strain rate dependent, it is non-Newtonian. The flow stress is correlated with the viscosity and the expression of the viscosity can be obtained after knowing the flow stress.

In a large range of temperature and strain rate, for most metals, the effects of temperature and strain rate to flow stress are not negligible and they must be considered in the design and control of manufacturing processes. Many researchers have studied the temperature and strain rate dependent properties of several materials. Due to numerous challenges encountered in measuring mechanical properties at high temperature and high strain rates, the data base of experimental measurements is limited. Consequently, the best option is to propose trusted constitutive models to do some reasonable extrapolations. Mukai et al. [135] tested the influence of strain rate on flow stress of fine-grained IN905XL aluminum alloys. They concluded that the yield strength for IN905XL is a weak function of strain rate when the strain rate is below 10 s-1 and is a strong function when it is up to 1 ×103 s-1. They also observed negative strain rate sensitivity of the flow stress. Malas and Seetharaman [136] presented a comprehensive methodology for modeling material behavior during hot-deformation processing. Balasubrahmanyam and Prasad [137] investigated the mechanisms of hot deformation in the alloy Ti-5.5Al-1Fe in a temperature range 750 to1150℃ and a strain rate range 0.001 to 100 s-1 by compression tests. Chen et al. [138] did research on the stress-strain behavior of aluminum alloy 6xxx and 7xxx at a wide range of strain rates. They concluded that AA6xxx alloys exhibit no significant rate sensitivity while moderate rate sensitivity for AA7xxx alloys.

Zener and Hollomon designed an experiment in 1944 [100] to validate their proposed equivalence of the effects of changes in strain rate and in temperature upon the stress-strain relation in metals. They found that the stress-strain relation in steels depends on strain rate and temperature only through a single parameter, now called Zener-Hollomon parameter Z,

$$Z = \dot{\varepsilon} \exp\left(\frac{Q}{RT}\right) = A[\sinh(\alpha\sigma)]^n \tag{6.16}$$

where Q is the activation energy, R is the universal Gas constant, and T is the absolute temperature, A, α, and n are material constants. Many people developed this relation and made it widely accepted not only on steels but other BCC and FCC crystalline materials. Later, Sheppard and Wright [99] developed a form of steady state constitutive relationship that is convenient and only needs the Zener-Hollomon parameter, as expressed below

$$\sigma = \frac{1}{\alpha}\ln\{\left(\frac{Z}{A}\right)^{1/n} + \left[\left(\frac{Z}{A}\right)^{2/n} + 1\right]^{1/2}\} \tag{6.17}$$

It is obvious that in this equation the flow stress is only a function of temperature and strain rate and the strain effect is neglected.

This constitutive relationship has been widely used in hot working processes, such as extrusion and rolling, and also was used by aluminum companies for on line control in extrusion and tandem mill rolling. Sheppard [139] applied this relationship to AA2024 and established pressure and speed limitations for varying section shapes. Clode and Sheppard [140] also used this equation to study hot extrusion process and found that pressure requirements, microstructural features, and surface defects, pickup and die lines can be characterized through mathematical formulae and represented within a limit diagram framework. Sheppard and Jackson [141] conducted experiments on a series of aluminum alloys from the 1XXX to the 7XXX and published the constants of the constitutive

relationship. Duan and Sheppard [142] compared the difference of the equation (6.17) and other two constitutive equations in the application of numerical simulations in hot rolling process.

Although there are other forms of constitutive relationships for flow stress, such as the Johnson-Cook model [143], the Zener-Holloman model is chosen for the viscosity in the current work. One reason is that in the fluid modeling the variables don't include strain and the equation (6.17) neglects strain effect. The other one is that it has been widely used in numerical simulations of hot working of aluminum alloys, such as hot extrusion and friction stir welding, which are similar processes as friction extrusion process. Also the equation (6.17) has been studied on aluminum alloys by many researchers and the constants are verified to be reliable. If the flow stress in equation (6.17) is put into equation (6.15), the complete of viscosity can be obtained as follows

$$\mu = \frac{1}{3\dot{\varepsilon}\alpha}\ln\{\left(\frac{Z}{A}\right)^{1/n} + \left[\left(\frac{Z}{A}\right)^{2/n} + 1\right]^{1/2}\} \tag{6.18}$$

In this form, the viscosity is only a function of temperature and strain rate since the constitutive equation of flow stress has no strain effect.

If the equation (6.18) is used for viscosity expression, some artificial modifications should be made to avoid numerical difficulties. Notice that the value of viscosity approaches infinity when the strain rate tends to zero. In friction extrusion process, there exists a large area where deformation is small and the strain rate may be close to zero. To avoid such errors, a minimum value also is set for the strain rate. It is set not smaller than 10-4 s^{-1}. An enough large number, 10^{12} Pa-s, is also chosen by referring to simulations on friction stir welding [97]. Beyond this value, the viscosity is set to equal to it.

The material constants in equation (6.18) for aluminum alloy 6061 can be found in the literature [141]. The values for the constants are listed in Table 6.1.

Table 6.1 Parameters for flow stress (from [141])

Metal	α (MPa^{-1})	n	Q (J-mol^{-1})	G	ln A (s^{-1})
AA6061	0.045	3.55	145,000	8.314	19.3

6.3 Model Description

As indicated before, to study the friction extrusion process with the combination of both heat transfer and material flow field, a three dimensional CFD model has been developed. The model includes all parts in the experiment, such as the die, the chamber wall, the back plate, and the table. Only limited parts of the die, back plate, and table are modeled in the simulation and their sizes used in the model are chosen so that they represent them well. The other parts have actual geometrical dimensions of the experimental setup. The finite volume method is used to discretize the computational domain. In the modeling, the precursor material is treated as a non-Newtonian fluid and the other parts are considered as rigid solids. A cross section of a converged mesh is shown in Figure 6.1. The minimum size of the mesh is located at boundary layers which are close to the interfaces between solids and fluid and its size is 0.05 mm and the maximum cell size is 1.2 mm. The commercial code ANSYS FLUENT is used for the computation.

As stated above, the heat transfer and material flow are modeled not in a fully coupled way and the thermal model in Chapter 5 is adopted in the current modeling. It uses a small layer of the aluminum alloy sample under the interface between the sample and the rotating die as the heat generation source to approximate the heat generation during the friction extrusion process. A uniform height of 4 mm for the layer is taken based on

experimental observations of marker material deformation in the remnant precursor at the end of the experiment. The total power input in the model is correlated to the mechanical power recorded in the experiment based on the fact that almost all mechanical power was converted into heat. The heat generation rate per volume in the layer is assumed to be linear both along vertical and radial directions, as described in three-dimensional Cartesian coordinate system below

$$q = \frac{3Q_{total}}{\pi(H-h)^2R^3}(z-h)\sqrt{x^2+y^2} \tag{6.19}$$

where q is the heat generation rate per volume, Q_{total} is the power input equal to the mechanical power in experiment, H is the height of the precursor sample, h is the height of the sample minus the volume heating layer, and R is the radius of the sample. This heat source is implemented in ANSYS FLUENT through a user defined function.

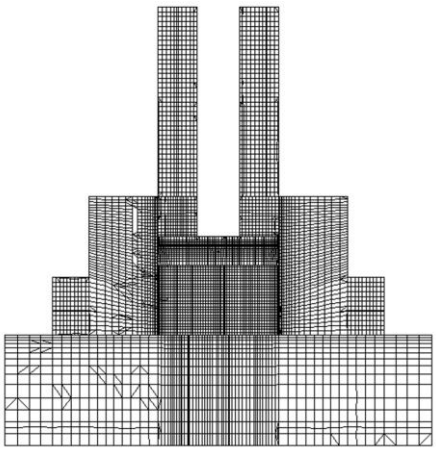

Figure 6.1 A cross-section of the converged grid.

One of the advantages of numerical modeling is that it can provide some predictions of interest which are difficult to obtain experimentally. One goal of the current modeling is to investigate the distribution of the marker material in the experiment and thus to try to

understand the material flow pattern. However, since the Eulerian description of motion is used in this simulation, it is very difficult to track the material flow directly. Alternatively, tracking released solid particles in the fluid can achieve the goal. In this model, several massless solid particles with a 10^{-3} mm diameter are used as markers released in the precursor material which is considered as a fluid in the chamber. The particles are initially positioned on the ZX plane with different radii. Because these particles are massless they don't affect the interested simulation predictions (e.g. velocity and temperature fields). Followed with nearby fluid, the particles whose trajectories can be tracked represent the fluid material flow.

In the friction extrusion process experiment, the die moved down besides rotating to push the precursor material in the chamber out through the extrusion hole so the extrusion process was carried out. The displacement of the die is shown in Figure 5.4. In the modeling, the movement of the die is simulated as input. As the die moves down, the volume of the fluid in the chamber decreases since a part of it is extruded out. The dynamic meshing technique in FLUENT is used to handle the change of the fluid computational domain. To keep the boundary layer near the interface between the die and precursor material and to avoid computation difficulties, the whole fluid computational domain moves down with the same vertical velocity as the die while the bottom layers of mesh disappear gradually. Correspondingly, the volume heating zone moves down to keep it on top of the fluid.

6.4 Initial and Boundary Conditions

The thermal initial and boundary conditions are the same as those used for the pure thermal model in Chapter 5 because the same friction extrusion process experiment is used.

The gap and the thermal resistance are treated in the same way, i.e. changing the conductivity.

The current model simulates the process of extrusion which is caused by the vertical motion of the die. The die moves down at a speed obtained from the die positions recorded during the experiment, as shown in Figure 5.5. As a result, the wire extrusion rate in the simulation is consistent with the experiment.

For fluid based numerical modeling, the contact behavior between fluids and solids must be defined. However, the real contact condition between the die and aluminum alloy in the friction extrusion experiment may vary during the process and it is currently not known. For the processes which have characteristics similar to friction extrusion, such as the friction stir welding and extrusion, several researchers have studied the contact condition between tools and workpieces. Valberg and Malvik [134] showed by experiments that in extrusion process both sticking and slipping conditions existed on the die. Doude et al.[144] tried to study the influence of tool shoulder contact conditions on material flow during friction stir welding. Some numerical modeling work [96, 115, 145] was to investigate the partial sticking/slipping phenomenon during friction stir welding. Other people adopted fully sticking condition in CFD modeling of friction stir welding and obtained reasonable predictions [96, 97, 103]. In the present work, both fully sticking and partial slipping/sticking conditions are studied.

6.5 Results and Discussions

6.5.1 Thermal Validation

As described in Chapter 2, the temperature at several different positions in the friction extrusion experiment was recorded. The measured temperature variations with

time are compared with numerical predictions as shown in Figure 6.2. In general, a good agreement between the experimental measurements and the predictions is observed.

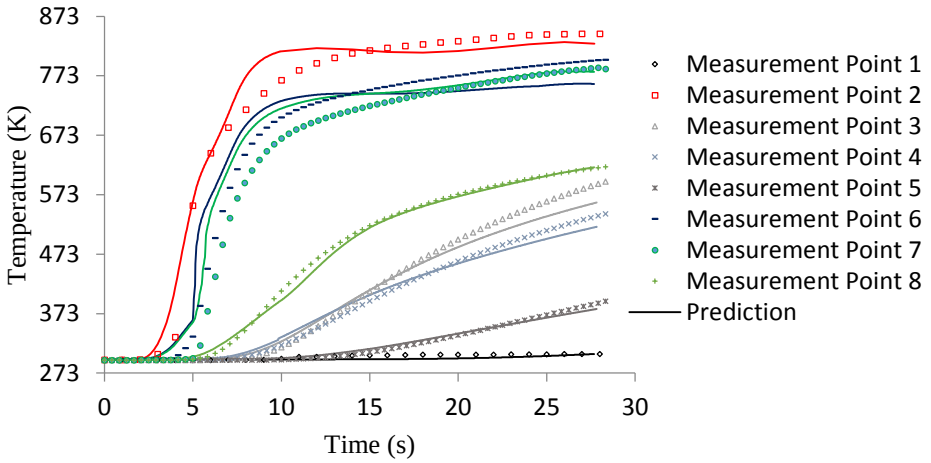

Figure 6.2 Comparisons between temperature predictions of the thermo-fluid model and experimental measurements.

For comparisons, the comparisons presented in Chapter 5 between the temperature predictions in the pure thermal model and the same experimental measurements are shown in a separate figure Figure 6.3. Since the experimental measurements are the same, differences of the temperature predictions between the pure thermal model and the thermo-fluid model can be observed from the comparisons. It is seen that there are unnoticeable differences for the temperature at point 1, 3, 4, and 5, which are on the outer surfaces, far from the heat source zone. The temperatures at rest points have mild changes after t = 10 s. The changes come from mainly from the influence of material flow and movement of the heat generation zone (moving down pushed by the die). The material flow introduces convection heat transfer in the material and the movement of the heating zone results in variations of the distances from the heat source to the temperature measurement points. The temperature at sensitive points (point 2, 6, and 7) which are closer to the heat source zone have larger changes. For point 8, the difference is very small.

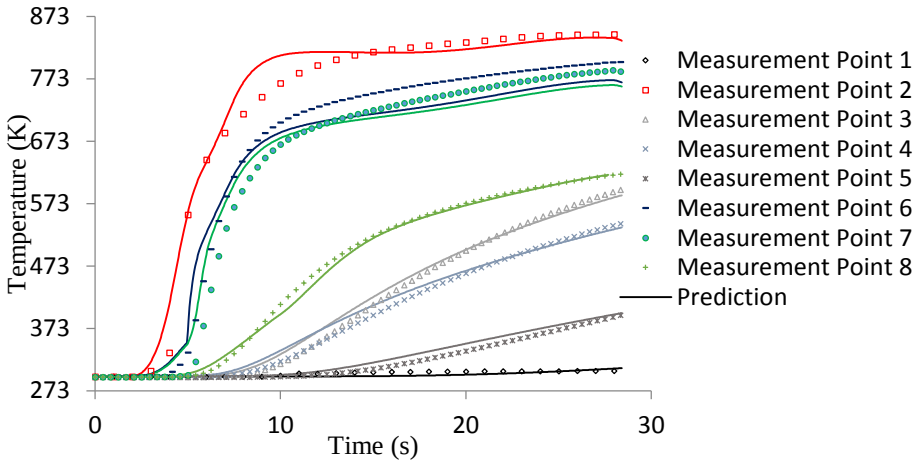

Figure 6.3 Comparisons between temperature predictions of the pure thermal model and experimental measurements.

It is shown from the comparisons above that (1) the temperature field can be reasonably predicted by using the pure thermal model in the current decoupled thermo-fluid model, (2) thus the method used in friction stir welding, applying thermal models in fluid modeling, also works in modeling of friction extrusion process, and (3) the material flow has very limited influence on the heat transfer phenomenon.

6.5.2 Material Flow Validation

Interpolation

As described in section 6.4, some massless solid particles are released in the precursor material which is a fluid in the modeling. These particles can be tracked and their trajectory paths can be recorded during the simulation. In the modeling only some of particles are extruded out of the chamber and the distribution of them on the extruded wire can be compared with experimental measurements. In the experiment, the traces of the marker material can be observed clearly on the extruded wire cross sections although it was distorted and stretched since the marker material is a continuum. However, in the

simulation, the number of the solid particles is finite and it is not enough to have a better view effect when comparing them with experimental observations on wire cross sections. To have better comparisons, interpolations of the predictions about the particles positions on extruded wire cross sections are necessary to obtain more data points.

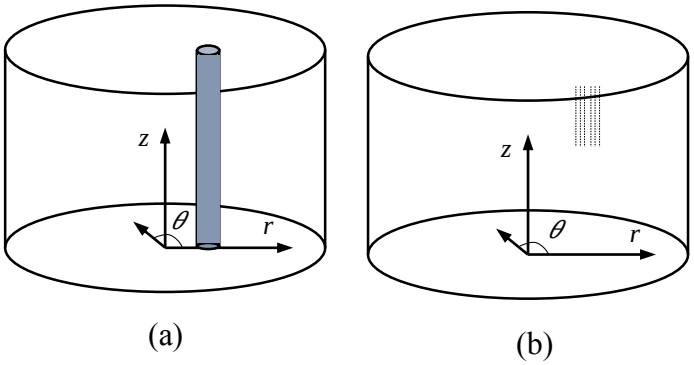

Figure 6.4 Schematics of (a) aluminum alloy sample with the marker wire and (b) particles in simulation.

Figure 6.4 shows schematics of the initial positions of the marker material in the experiment and a part of solid particles in the simulation. They are analyzed in a same cylindrical coordinate system. Interests only focus on the particles which are initially placed in the same region occupied by the marker material. There are 13 columns of particles with radius from 2.93 - 5.57 mm and 25 rows with height from 15 - 18 mm on the *z-r* plane. In total, there are 325 particles. The region where these particles are placed is called particle region. The goal is to obtain any data point in the whole marker material region in the height range of 15 - 18 mm from these particles. Two reasonable assumptions are made to do the interpolation. First, it is assumed that the radii of the particles to the center axis keep unchanged after they reach the exit extrusion hole. Second, based on the axisymmetric geometry, it is assumed that particles, which have the same initial heights, have same path line shapes in the space. Based on the two assumptions, for any particle in

the particle region, the angle and time when it reaches the exit hole can be obtained by interpolation.

(a) (b) (c)

Figure 6.5 Marker distributions on wire cross sections in experiment at time (a) t = 13.0 s (b) t = 16.9 s (c) t = 18.8 s.

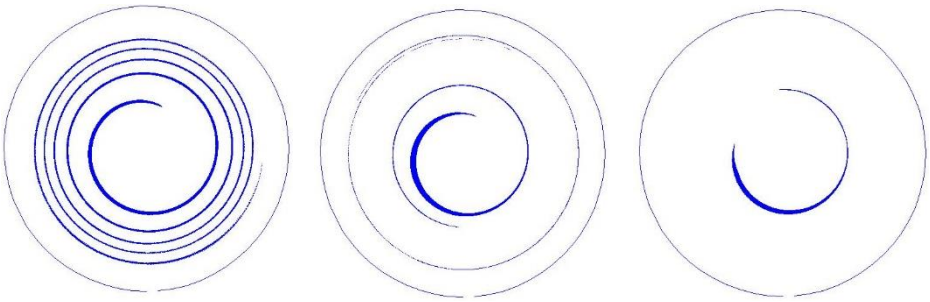

(a) (b) (c)

Figure 6.6 Predicted marker distributions on wire cross sections with sticking factor 0.3 at time (a) t = 13.0 s (b) t = 16.9 s (c) t = 18.8 s.

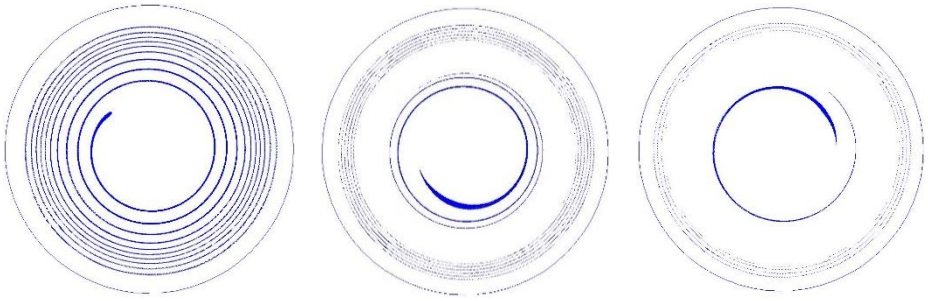

(a) (b) (c)

Figure 6.7 Predicted marker distributions on wire cross sections with sticking factor 0.6 at time (a) t = 13.0 s (b) t = 16.9 s (c) t = 18.8 s.

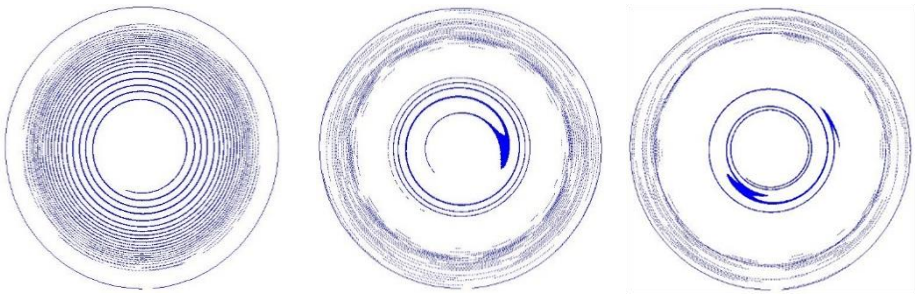

(a) (b) (c)

Figure 6.8 Predicted marker distributions on wire cross sections with sticking factor 1.0 at time (a) t = 13.0 s (b) t = 16.9 s (c) t = 18.8 s.

In the modeling, the positions of the particles at every moment are recorded. For each particle that is extruded out, the time t and the angle θ when it reaches the exit hole and the initial coordinates, including radius r and height z, can be obtained. Then two series of data points with respect to (r, z, θ) and (r, z, t), respectively, are available to do the interpolation. The objective of the interpolation is to find the time and angle of any particle in the particle region when it reaches the exit hole based on the available particle data. The interpolation work is done by my co-worker Mr. Xiao Li. As many as thousands of data points can be obtained through the interpolation. The time when a particle reaches the exit hole determines its longitudinal position in the wire since the extrusion rate is known. As a result, the particles and the marker material on same wire cross sections can be compared.

Comparisons

As mentioned earlier, in this model, different contact conditions have been tried. Here a sticking factor is defined. A sticking factor indicates the degree of the sticking of the material to the tool. For example, a sticking factor of 0.3 means the rotating speed of the fluid on the fluid-solid interface is 30% of the tool rotating speed. In the current

simulations, 0.3, 0.6, and 1.0 are used to for the sticking factor. Figure 6.5 shows the marker material distributions during the friction extrusion experiment on extruded wire cross sections. The marker material shows a dark color after chemical etching. The rest is aluminum alloy 6061. The predicted marker material distributions on the extruded wire cross sections with different sticking factor values are shown in Figure 6.6, Figure 6.7, and Figure 6.8, respectively. From the comparisons of the numerical predictions about the marker distribution, the marker forms more revolutions of spirals in the simulation with bigger sticking factor. The can be explained by the fact that the higher sticking factor means higher rotating speed for the fluid on the fluid-solid interface, resulting in more strong stirring. However, the experimental observations show the marker material has more revolutions of spirals on extruded wire cross sections. The predictions with sticking factor 1.0 as shown in Figure 6.8 are closest to the experimental observations, implying that the sticking factor 1.0 is the best for material flow prediction. Comparing the numerical predictions and experimental observations, it can be seen that they share some features in common, such as (a) the markers form continuous spirals on extruded wire cross sections and (b) the revolutions of the spirals on the cross sections decrease as extrusion continues. However, some differences exist between the simulation and experimental measurements. The discrepancies are mainly due to some assumptions made in the modeling. Nevertheless, the qualitative comparisons indicate that the material flow trends can be captured.

6.5.3 Computed Temperature Field

The predicted temperature fields with different instants are shown Figure 6.9. For comparisons, the predicted temperature fields in the pure thermal model are also displayed, as seen in Figure 6.10. It is seen predictions are very similar. The temperature variation

trends and magnitude are very close. The features of the temperature fields are not discussed here since they are discussed in Chapter 5.

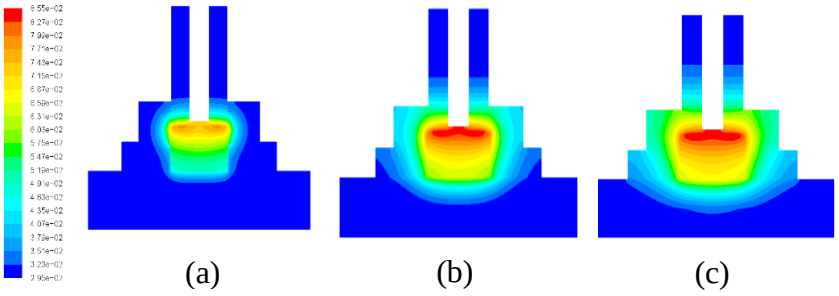

Figure 6.9 Predicted temperature contours at (a) t = 7s, (b) t = 14s, (c) t = 21s.

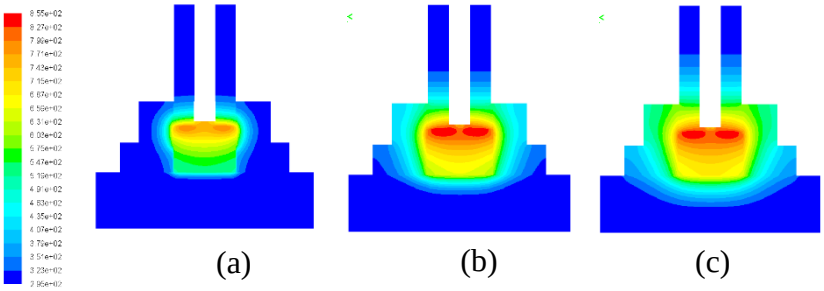

Figure 6.10 Predicted temperature contours at (a) t = 7 s, (b) t = 14 s, (c) t = 21 s.

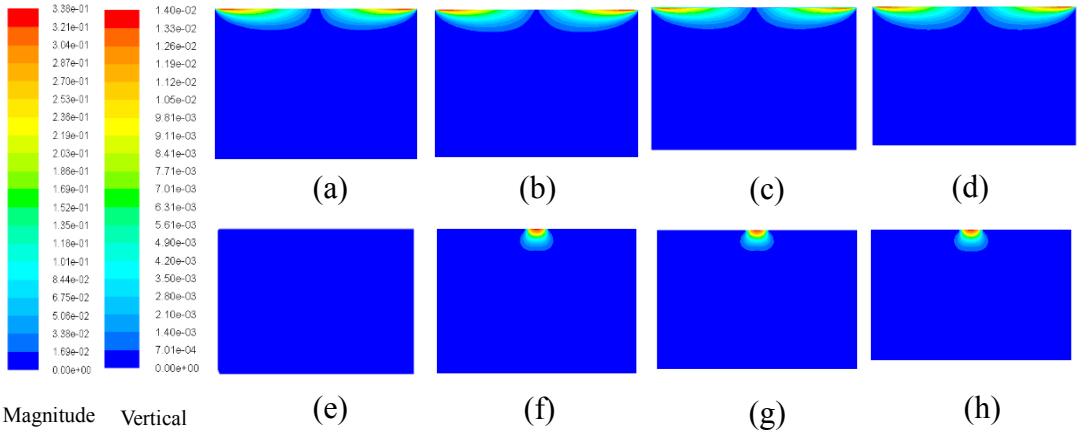

Figure 6.11 Predicted velocity contours at (a) t = 10 s, (b) t = 15 s, (c) t = 19 s, (d) t = 24 s, (e) t = 10 s, (f) t = 15 s, (g) t = 19 s, (h) t = 24 s.

6.5.4 Predicted Flow Fields

Figure 6.11 depicts the computed velocity contours on a longitudinal section of the precursor sample at different instants. Before wire extrusion, as shown in Figure 6.11 (a), a small region under the die-precursor sample interface has obviously higher velocity. In the center of the region, the velocity is close to zero due to the lower die rotating speed in the center. Since there is no die vertical movement or no wire extrusion at this moment, there is only tangential velocity. The velocity drops drastically when the distance from the interface increases except near the extrusion hole. The velocity has a peak near the middle of the radius at same heights. At the corner between the top surface and lateral surface, the velocity changes from low to high and thus the gradient is high. That's because the fluid at the top surface has high tangential velocity near the corner while the velocity is zero on the lateral surface due to non-slip condition used. The velocity contrast results in such velocity field in the corner. Figure 6.11 (b) - (d) show resultant velocity fields during wire extrusion at t = 15 s, 19 s and 24 s, respectively. Compared with Figure 6.11 (a), the contour plots have no obvious difference except in the region near the extrusion hole. Under the extrusion hole, there is vertical velocity due to extrusion and the total velocity is noticeable. Since the extrusion rate is constant, the velocity at this area doesn't change much. Although that the temperature in the region beneath the interface between die and the aluminum rises after the start of wire extrusion as discussed in the last section, the velocity field seems unchanged. The explanation for this is that the viscosity doesn't change much in a small range of temperature and thus the velocity field is little affected. This also can explain that the wire extrusion rate almost is constant. Figure 6.11 (e) – (h) show the vertical velocity contours at t = 10 s, 15 s, 19 s and 24 s, respectively. As the resultant velocity contours, the

vertical velocity contours at different times after start of wire extrusion look like the same. A small region around the extrusion hole had relatively higher vertical velocity, indicating that the vertical velocity is dominant in that area. The predicted velocity fields show that the stir zone, where the material is experiencing large deformation, keeps almost the same shape after the start of wire extrusion, since the velocity field doesn't change much.

Another important flow field variable is strain rate, which reflects the change of deformation of the material, since it is known that it affects material recrystallization and can be used to estimate the material microstructure [146]. In other material processes, like friction stir welding, extrusion and rolling of alloys, researchers tried to establish relationships between the strain rate and the material grain size or subgrain size. References [146-148] studied the relationship between grain size and strain rate for AZ31 magnesium alloy and others [86, 149, 150] investigated the relationships between subgrain size and strain rate. Due to lack of grain size measurements in this work, the relationship between grain or subgrain size and strain rate is not discussed and only the predicted strain rate fields at different times are presented. Figure 6.12 shows the strain rate fields at various moments after start of extrusion. Only some select contours are shown. The strain rate is less than 1 /s in the region below the 1 /s contour and it is larger than 100 /s in the area beyond the 100 /s contour. As the velocity fields, the relative larger strain rates occur in a small region under the interface between the die and aluminum alloy. In general, the strain rate fields look like almost the same also as the velocity fields do. The maximum value area is at the corner between the top surface and lateral surface of the aluminum alloy sample. That is not different to understand since that the velocity gradient is highest at the corner can be seen in the velocity fields as shown in Figure 6.11. The iso-valued strain rate

contours also converge at the corner. The maximum value of strain rate in the modeling is larger than 100 /s, which is larger than the values reported in some studies of friction stir welding [86, 151].

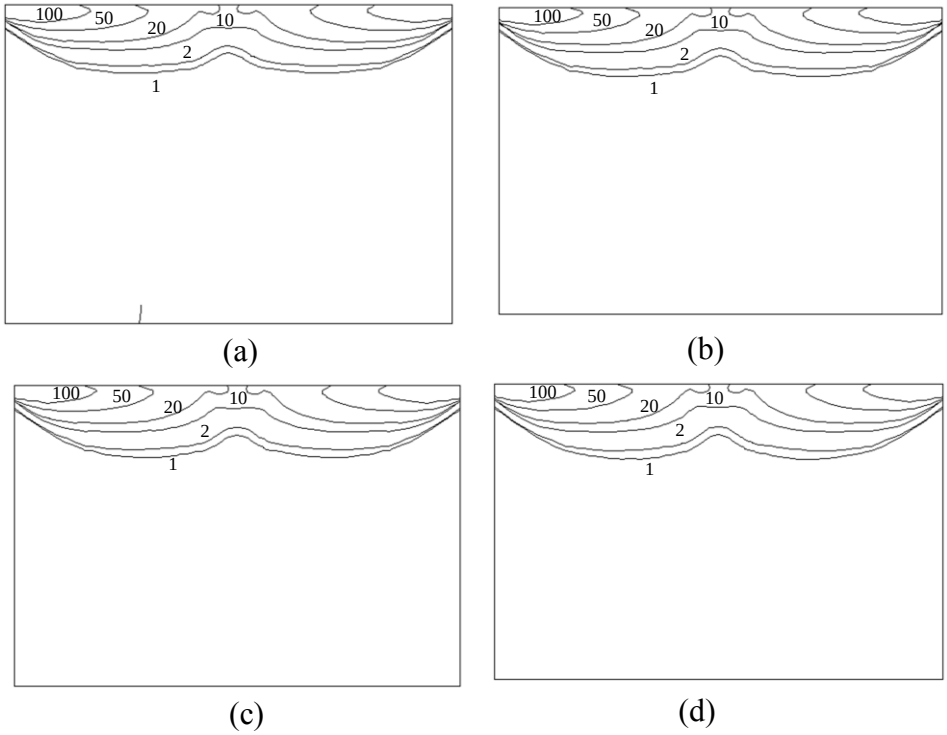

Figure 6.12 Strain rate fields (unit s^{-1}) at (a) t = 11 s (b) t = 16 s (c) t = 20 s (d) t = 24 s.

Viscosity is a property that is related to flow stress of the material and that also determines the fluidity of the material. Computed viscosity field cross sections at different moments are shown in Figure 6.13. For brief, only some selected value contours are displayed and only the fluid in chamber is chosen. Since the extrusion of wire results reduction of the volume of the fluid, the height of the fluid domain decreases with time. The contours shape is like a bowl with a convex center. Figure 6.13 (a) shows the contours at time t = 11 s when the extrusion just starts. As seen, the viscosity is lower near the die/sample interface, especially at the two upper corners and it increases gradually as it is

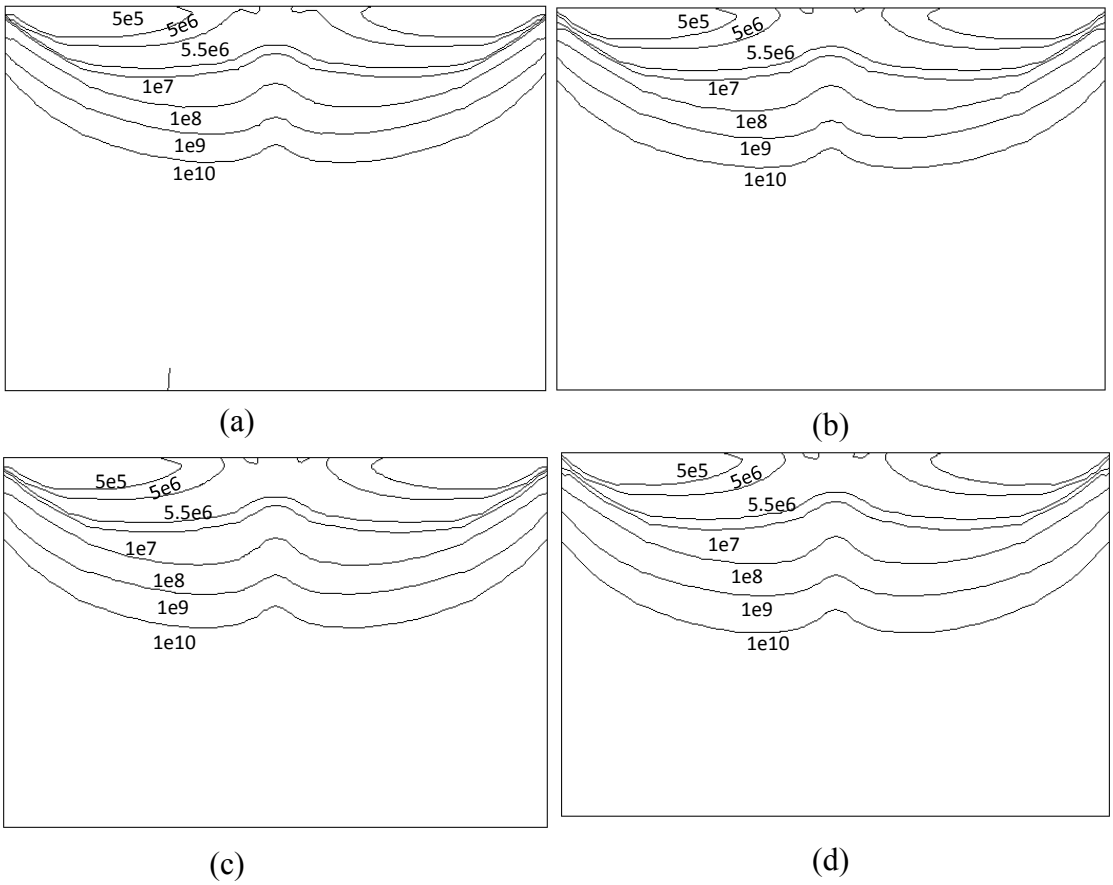

Figure 6.13 Viscosity fields (unit Pa-s) at time (a) t = 11 s (b) t = 15 s (c) t = 19 s (d) t = 22 s.

far from the interface vertically. The region below the 1e7 Pa-s contour has larger viscosity. The features of viscosity distribution can be explained from the temperature fields and strain rate fields. High temperature softens the material in the chamber so the viscosity is smaller in higher temperature regions. The temperature in the region near the interface is higher and the strain rate at the central area is relatively small, together resulting in such shapes of the viscosity contours. The viscosity contours of the same values at different moments as shown in Figure 6.13 (a)-(d) indicate that the contours move down slowly. Nandan et al. [105] reported a cutoff viscosity of 5.0e6 Pa-s (above which no significant

material flow occurs) based on experimental observations on AA6061 to find the characteristic shape of the thermo-mechanically affected zone in a CFD model. The viscosity contour of this value is also shown in Figure 6.13. It is seen that the thermo-mechanically affected zone almost keep the same shape and same location relative to the surface. In general, the viscosity field varies mildly after the start of extrusion.

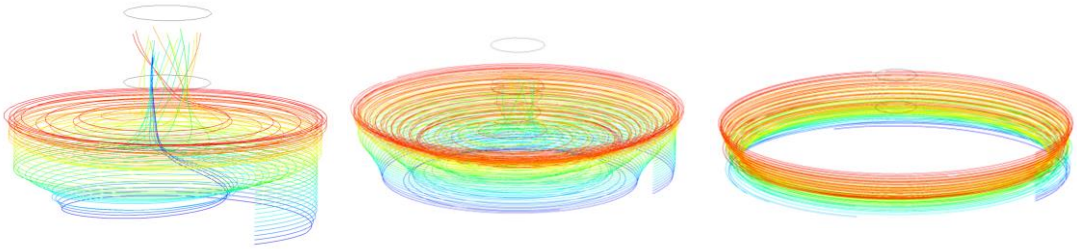

(a) (b) (c)

Figure 6.14 Path lines with initial positions at (a) r = 4.3 mm (b) r = 7.2 mm (c) r = 10.4 mm from the center.

6.5.5 Material Flow Features

In the modeling, the particle markers released in the precursor material flow with it and leave continuous trajectory paths. Since the particles are massless, they fallow the nearby material all the time and thus their trajectory paths represent the nearby material paths. Studying the paths of particle markers can help understand how the precursor material in the chamber flows and how the extruded wire is formed. It is worth to note that numerical modeling is able to provide vivid visualization that is not available in experiment. Figure 6.14 depicts the path lines of the particle markers with different initial positions in the simulation. The initial heights of these path lines range from 15 mm to 18 mm. Every path line has a unique color. For a better view, the figures don't have the same scale. Figure 6.14 (a) shows a group of path lines which originate from one third of sample radius from

the center. All of these path lines go through the extrusion hole, indicating that the material there is extruded out of the chamber to form the wire. Before reaching the extrusion hole, all path lines have experienced spiral shapes which feature decreasing radii and increasing heights. For those path lines who have higher initial heights, their spirals have more rotations. The spirals are the consequence of the rotating die which is stuck by the material at the die-sample interface. Near the interface, material has larger tangential velocity and thus experiences more rotations. This can explain those path lines with more spirals. The path lines with lower initial heights have more obvious height increase. The decreasing radii of spirals show the material flows toward the center and the increasing heights indicate that the material has vertical velocity. All of these imply that there is material in the central region being pushed spirally upward the extrusion hole. Figure 6.14 (b) shows path lines of particles which are released at positions with a distance 7.2mm from the center (The sample radius is 12.5 mm). Only some of the path lines which have lower initial positons reach the extrusion hole, meaning that the material in that region with lower heights flows out of the chamber to compose the extruded wire while those with higher heights stay in the chamber all the time during the process. The path lines with lower initial heights show the material there also is pushed to both the center and the extrusion hole spirally. The spiral shapes of the particles with higher initial heights are different. Since they stay in the chamber all the time and in the higher velocity region they have experienced more number of spirals. During the friction extrusion process, the die moves down gradually, pushing the material just under it down. As a result, the heights of these particles decrease slowly. Figure 6.14 (c) show the path lines whose initial positions are 10.4 mm away from the center. Apparently, none of the particles pass the extrusion hole and no

material there goes out of the chamber. The number of spirals is obviously less due to the region has small velocity. Likewise, the radii of the path lines with lower initial heights decrease but with slight variation. Path lines in Figure 6.14 (b) and (c) show that there exists a dead zone as in traditional extrusion process where the material can never be extruded out of the chamber.

6.5.6 Summary and Conclusions

This chapter has presented a three-dimensional thermo-fluid model in order to provide a comprehensive understanding of the friction extrusion process. Both heat transfer and material flow are modeled in this model. The volume heat model in Chapter 5 is used for heat transfer modeling and the thermal resistance between the sample and the back plate is modeled by changing the conductivity of the back plate. The temperature predictions have been compared with experimental measurements and the results from the pure thermal model.

The sample is considered as a non-Newtonian fluid and the CFD method is used to simulate the material flow. The viscosity of the fluid is a function of strain rate and temperature. To investigate the material flow pattern and provide data to compare with experimental measurements, some massless solid particles are used in the fluid to track the nearby fluid. Different contact conditions between the die and the sample have been tried and three values are used for the sticking factor.

The comparisons show the temperature predictions have a good agreement with experimental measurements and the predicted temperature variations are similar with those in the pure thermal model. The predicted distribution of the particles on extruded wire cross sections also have the same trends with experimental observations. Some findings are

concluded as follows.

1. The material flow has unnoticeable effect on temperature field and the uncoupled heat transfer and material flow model also works for friction extrusion process.
2. The flow field variables, i.e. velocity, strain rate, and viscosity, almost keep the same during after the start of extrusion although the temperature field changes all the time.
3. The particles path lines show that material in the central zone of the process chamber is pushed spirally towards the extrusion hole to form the extruded wire; then the material near the central zone moves in to fill the space in the central region; and material in the upper corner below the die-aluminum alloy interface and away from the extrusion hole forms the dead zone - the material stays in the chamber and never get extruded.

CHAPTER 7 SUMMARY AND RECOMMENDATION

7.1 Summary

The friction extrusion process has been studied successfully through numerical simulations in this dissertation. This work includes a flow visualization study by a physical model with transparent fluid and tools, a pure thermal model that focuses on heat transfer phenomenon, and a three-dimensional model which takes both heat transfer and material flow into consideration to provide a comprehensive understanding of the friction extrusion process.

First, a physical model with a Newtonian fluid was studied to mimic the friction extrusion process. The flow visualization study is to capture the material feature during friction extrusion process. It is a simplified model that only has tool rotation and there is no extrusion part. The model consists of a viscous Newtonian fluid, a chamber wall, and a back plate. The fluid and the tools are transparent so that experimental observations and measurements can be achieved easily. The Reynold number is equal to that approximated in friction extrusion process and it indicates a laminar flow. Due to the regular shapes of the fluid domain geometry and boundary conditions, an analytical solution about the flow field can be developed. Some assumptions, such as axisymmetric problem and zero velocity in radial and vertical directions, were made to enable the analytical solution attained. A three-dimensional CFD simulation of the simplified model was also performed. No assumption was made for the numerical modeling. Differences between the analytical solution and the numerical solution are very small, below 2%. The analytical solution was

also compared with experimental measurements implemented by a DIC system on tiny particles in the fluid. A good agreement can be observed, serving as an evidence for experimental validation of the analytical solution and CFD simulation predictions.

Next, a pure thermal model was developed to investigate the heat transfer phenomenon during friction extrusion process. The heat generation approximation is the crucial when modeling the temperature field. A volume heating model has been proposed based on the characteristics of the friction extrusion process. The heat generation produced by friction between the die and aluminum alloy sample and the plastic deformation under the interface between the die and the sample is represented by a layer under the die-sample interface. The heat generation rate is assumed linearly distributed along vertical and radial directions. No frictional heat generation that is in the form of surface flux was included in the model since it is compensated in the volume heating model. The total power input into the system is related to the mechanical power during the friction extrusion experiment and it is assumed all mechanical power is transferred to heat.

The numerical model includes all parts involved in the friction extrusion experiment, such as the die, the chamber wall, the back plate, the support table, and the aluminum alloy sample. Only parts of the die, the back plate, and the table are included and their sizes are chosen to represent these bodies. The material flow is not modeled in the pure thermal model so all the bodied are treated as solids. As a result, only conduction equation is needed to solve for the temperature field. The boundary conditions have been carefully handled. The gap between the die and the aluminum sample is modeled by changing the conductivity and how it is filled was estimated.

The temperature predictions have a good agreement with the experimental measurements at several points, indicating that the volume heating model can be used to reasonably represent the heat generation during the friction extrusion process. The numerical results show the heat transfer phenomenon is a transient process and the temperature field is changing all the time. However, the temperature under the extrusion hole doesn't change much after the start of extrusion. Since the material under the extrusion hole forms the wire, the thermal history of the extruded wire can be estimated. It's seen although it is transient heat transfer, the highest temperature that the wire experiences changes small. The numerical results also show there is thermal resistance between the aluminum sample and the back plate.

A three-dimensional thermo-fluid model also has been presented to provide a comprehensive understanding of the friction extrusion process. Both heat transfer and material phenomena are modeled and more information can be obtained from the model. The volume heating model is used for the heat generation source and the assumption made in the pure thermal model, which is the material flow has small influence to the heat transfer during friction extrusion process, can be tested in the thermo-fluid model. The thermal initial and boundary conditions are the same as the pure thermal mode except the contact between the aluminum alloy sample and the back plate. The thermal resistance is simulated by changing the conductivity of the back plate. The predicted temperature results show that the material flow has unnoticeable effect on temperature field and the uncoupled heat transfer and material flow model works for friction extrusion process.

The Eulerian description of motion is used to simulate the material flow due to extreme deformation and distortion of the material. The aluminum alloy sample is treated

as a non-Newtonian fluid given that the flow stress is strain rate and temperature dependent. The Zener-Holloman parameter is adopted to describe the constitutive equation. Thus the fluid viscosity is a function of strain rat and temperature. The tools are seemed as rigid solids. The geometry sizes of the bodies are same as those in the pure thermal model. For the contact condition between the rotating die and the aluminum alloy sample which is treated as a fluid, different values, i.e. 0.3, 0.6, and 1.0, have been tried for the sticking factor. Massless solid particles are released in the fluid in the simulation as tracers to track the material flow paths. Since the particles don't affect the temperature and fluid fields, they can represent the material flow. The distribution of the particles on the extruded wire cross sections was compared with experimental measurements. The qualitative comparisons show that the distribution trends and features can be captured by the thermo-fluid model. The numerical model provides information that is not available in experiment, such as the velocity, viscosity, and strain rate fields. The predicted flow fields almost keep the same after the start of extrusion although the temperature field changes. The path lines of the particles show that the material in the central zone of the process chamber is pushed spirally towards to extrusion hole to form the wire; then the material near the central zone moves to fill the space in the central region; and there is a dead zone in the upper corner where the material stays in the chamber.

7.2 Recommendations

The current studies about the friction extrusion process have successfully established numerical models which are able to capture the characteristics of the heat transfer and material flow phenomena. The numerical simulations are aimed to understand the mechanisms occurred during the friction extrusion process and to help optimize the

experimental designs. Currently, there exists little literature for the friction extrusion process and the present work is only a first step to studying the friction extrusion process. There are several open questions and further studies are needed to develop the friction extrusion process.

One recommendation for further studies is to figure out if the friction extrusion process can reach steady state and when it reaches steady state. In this work, the experiment process was not long enough due to equipment restrictions so it was transient. Even though the temperature field is transient, the simulations show the flow fields don't change much. If the process operation is long enough, theoretically it will become steady state.

The current study only focused on one combination of the experimental parameters, namely the die rotating speed and the pushing force applied on the die, which can produce good quality wires. Parametric studies using the numerical models reported in this dissertation are recommended. Parametric studies can find out how the parameters influences the temperature field and flow field. This is very helpful for the experimental designs.

Different die shapes may be tried. In this work, the surface of the die that contacts the aluminum alloy sample is flat. The thermo-fluid model can be used to simulate the processes with other die surfaces, such scrolled shape. A dead zone was observed in the simulations and a cone-shaped surface may avoid the dead zone and improve the extrusion efficiency.

Only the CFD model was used in this dissertation to simulate the friction extrusion process. The advantage of this model is that the extreme deformation and distortion can be easily handled. However, the disadvantage is that the contact condition between the die

and the aluminum alloy sample must be defined. The contact condition is an important issue to study the friction extrusion process since it affects the stirring largely. It may be calculated by a finite element based model. The ALE finite element formulation is a good choice to deal with the mesh deformation and distortion.

Since the extruded wire is very long relative the sample and the ALE mesh always keeps its original topology, the wire is not recommended to be included in the ALE simulation of friction extrusion process. Eulerian surface can be used for the extrusion hole as an outlet. Because the material in the chamber keeps regular shape, the distortion of mesh can be easily taken care by the ALE technique. For the friction between the die and the aluminum alloy sample, the modified Coulomb's law can be employed. The Zener-Holloman constitutive equation for the aluminum alloys has been widely used in the numerical simulations for processes involved large strain rate and high temperature. If this constitutive equation is used in ALE modeling, a user subroutine may be needed for it.

REFERENCES

1. Thomas, W.M., E.D. Nicholas, and S.B. Jones, US Patent # 5,262,123. 1993.

2. http://www.uspto.gov/web/offices/com/sol/og/2002/week04/patexpi.htm.

3. Tang, W. and A.P. Reynolds, Production of wire via friction extrusion of aluminum alloy machining chips. Journal of Materials Processing Technology, 2010. **210**(15): p. 2231-7.

4. Gronostajski, J. and A. Matuszak, Recycling of metals by plastic deformation: an example of recycling of aluminium and its alloys chips. Journal of Materials Processing Technology, 1999. **92-93**: p. 35-41.

5. Ding, J., Thermo-mechanical analysis of wire and arc additive manufacturing process. 2012, Cranfield University: U.K.

6. http://www.nasa.gov/topics/technology/features/ebf3.html.

7. Lange, K. and K. Pöhlandt, Handbook of metal forming. 1985: McGraw-Hill.

8. Malvern, L.E., Introduction to the Mechanics of a Continuous Medium. 1969: Prentice-Hall.

9. Dieter, G.E., H.A. Kuhn, and S.L. Semiatin, Handbook of Workability and Process Design. 2003: A S M International.

10. Hibbitt, H.D., P.V. Marcal, and J.R. Rice, A finite element formulation for problems of large strain and large displacement. International Journal of Solids and Structures, 1970. **6**(8): p. 1069-1086.

11. McMeeking, R.M. and J.R. Rice, Finite-element formulations for problems of large elastic-plastic deformation. International Journal of Solids and Structures, 1975. **11**(5): p. 601-16.

12. Belytschko, T., W.K. Liu, and B. Moran, Nonlinear finite elements for continua and structures. 2000: Wiley.

13. Bathe, K.J., E.L. Wilson, and E. Ramm, Finite element formulations for large deformation dynamic analysis. International Journal for Numerical Methods in Engineering, 1975. **9**(2): p. 353-86.

14. Wifi, A.S., An incremental complete solution of the stretch-forming and deep-drawing of a circular blank using a hemispherical punch. International Journal of Mechanical Sciences, 1976. **18**(1): p. 23-31.

15. Lee, E.H., R.L. Mallett, and W.H. Yang, Stress and deformation analysis of the metal extrusion process. Computer Methods in Applied Mechanics and Engineering, 1977. **10**(3): p. 339-53.

16. Odell, E.I., A Study of Wall Ironing by the Finite Element Technique. Journal of Engineering for Industry, 1978. **100**(1): p. 31-36.

17. Wang, N.M. and B. Budiansky, Analysis of sheet metal stamping by a finite-element method. Transactions of the ASME. Journal of Applied Mechanics, 1978. **45**(1): p. 73-82.

18. Gotoh, M., A finite element analysis of general deformation of sheet metals. International Journal for Numerical Methods in Engineering, 1974. **8**(4): p. 731-741.

19. Oh, S.I. and S. Kobayashi, Finite element analysis of plane-strain sheet bending. International Journal of Mechanical Sciences, 1980. **22**(9): p. 583-594.

20. Wifi, A.S., Finite element correction matrices in metal forming analysis (with application to hydrostatic bulging of a circular sheet). International Journal of Mechanical Sciences, 1982. **24**(7): p. 393-406.

21. Yamada, Y., A. Wifi, and T. Hirakawa. Analysis of large deformation and stress in metal forming processes by the finite element method. in Metal Forming Plasticity\ Proc. Conf.\, Tutzing, Germany, Aug.-Sept. 1978. 1979.

22. Nagtegaal, J.C. and J.E. De Jong, Some computational aspects of elastic-plastic large strain analysis. International Journal for Numerical Methods in Engineering, 1981. **17**(1): p. 15-41.

23. Kudo, H. and S. Matsubara, JOINT EXAMINATION PROJECT OF VALIDITY OF VARIOUS NUMERICAL METHODS FOR THE ANALYSIS OF METAL FORMING PROCESSES. NASA Conference Publication, 1979: p. 378-403.

24. Rao, S.S. and A. Kumar, Finite element analysis of cold strip rolling. International Journal of Machine Tool Design and Research, 1977. **17**(3): p. 159-168.

25. Argyris, J.H. and J.S. Doltsinis, On the large strain inelastic analysis in natural formulation part I: Quasistatic problems. Computer Methods in Applied Mechanics and Engineering, 1979. **20**(2): p. 213-251.

26. Argyris, J.H. and J.S. Doltsinis, On the large strain inelastic analysis in natural formulation part II. Dynamic problems. Computer Methods in Applied Mechanics and Engineering, 1980. **21**(1): p. 91-126.

27. Nagtegaal, J.C. and N. Rebelo, On the development of a general purpose finite element program for analysis of forming processes. International Journal for Numerical Methods in Engineering, 1988. **25**(1): p. 113-131.

28. Strenkowski, J.S. and K.-J. Moon, Finite Element Prediction of Chip Geometry and Tool/Workpiece Temperature Distributions in Orthogonal Metal Cutting. Journal of Engineering for Industry, 1990. **112**(4): p. 313-318.

29. Voyiadjis, G.Z. and M. Foroozesh, A finite strain, total Lagrangian finite element solution for metal extrusion problems. Computer Methods in Applied Mechanics and Engineering, 1991. **86**(3): p. 337-70.

30. Jung-Ho, C. and K. Noboru, An analysis of metal forming processes using large deformation elastic-plastic formulations. Computer Methods in Applied Mechanics and Engineering, 1985. **49**(1): p. 71-108.

31. Kobayashi, S., A review on the finite-element method and metal forming process modeling. Journal of Applied Metalworking, 1982. **2**(3): p. 163-169.

32. Lee, C.H. and S. Kobayashi, New Solutions to Rigid-Plastic Deformation Problems Using a Matrix Method. Journal of Engineering for Industry, 1973. **95**(3): p. 865-873.

33. Zienkiewicz, O.C. and P.N. Godbole, A penalty function approach to problems of plastic flow of metals with large surface deformations. Journal of Strain Analysis, 1975. **10**(3): p. 180-3.

34. Lung, M. and O. Mahrenholtz, FINITE ELEMENT PROCEDURE FOR ANALYSIS OF METAL FORMING PROCESSES. Transactions of the Canadian Society for Mechanical Engineering, 1973. **2**(1): p. 31-36.

35. Kobayashi, S., RIGID-PLASTIC FINITE ELEMENT ANALYSIS OF AXISYMMETRIC METAL FORMING PROCESSES. 1977: p. 49-65.

36. Chen, C.C. and S. Kobayashi, RIGID PLASTIC FINITE ELEMENT ANALYSIS OF RING COMPRESSION. American Society of Mechanical Engineers, Applied Mechanics Division, AMD, 1978. **28**: p. 163-174.

37. Gotoh, M. and F. Ishisé, A finite element analysis of rigid-plastic deformation of the flange in a deep-drawing process based on a fourth-degree yield function. International Journal of Mechanical Sciences, 1978. **20**(7): p. 423-435.

38. Gotoh, M., A finite element analysis of the rigid-plastic deformation of the flange in a deep-drawing process based on a fourth-degree yield function—II. International Journal of Mechanical Sciences, 1980. **22**(6): p. 367-377.

39. Mori, K., K. Osakada, and T. Oda, Simulation of plane-strain rolling by the rigid-plastic finite element method. International Journal of Mechanical Sciences, 1982. **24**(9): p. 519-27.

40. Kim, Y.J. and D.Y. Yang, A formulation for rigid-plastic finite element method considering work-hardening effect. International Journal of Mechanical Sciences, 1985. **27**(7–8): p. 487-495.

41. Yoon, J.H. and D.Y. Yang, Rigid-plastic finite element analysis of three-dimensional forging by considering friction on continuous curved dies with initial guess generation. International Journal of Mechanical Sciences, 1988. **30**(12): p. 887-898.

42. De Saxce, G. and Z.Q. Feng, New Inequality and Functional for Contact with Friction: The Implicit Standard Material Approach∗. Mechanics of Structures and Machines, 1991. **19**(3): p. 301-325.

43. Feng, Z.-Q., 2D or 3D frictional contact algorithms and applications in a large deformation context. Communications in Numerical Methods in Engineering, 1995. **11**(5): p. 409-416.

44. Feng, Z.Q. and G. De Saxce, Rigid-plastic implicit integration scheme for analysis of metal forming. European Journal of Mechanics, A/Solids, 1996. **15**(1): p. 51-66.

45. Zienkiewicz, O.C. and I.C. Cormeau, Visco-plasticity-plasticity and creep in elastic solids-a unified numerical solution approach. International Journal for Numerical Methods in Engineering, 1974. **8**(4): p. 821-45.

46. Zienkiewicz, O.C. and P.N. Godbole, Flow of plastic and visco-plastic solids with special reference to extrusion and forming processes. International Journal for Numerical Methods in Engineering, 1974. **8**(1): p. 3-16.

47. Zienkiewicz, O.C., P.C. Jain, and E. Onate, Flow of solids during forming and extrusion: some aspects of numerical solutions. International Journal of Solids and Structures, 1978. **24**(1): p. 15-38.

48. Zienkiewicz, O.C., E. Onate, and J.C. Heinrich, A general formulation for coupled thermal flow of metals using finite elements. International Journal for Numerical Methods in Engineering, 1981. **17**(10): p. 1497-514.

49. Dawson, P.R., Viscoplastic finite element analysis of steady-state forming processes including strain history and stress flux dependence. 1978. Medium: X; Size: Pages: 26.

50. Tomita, Y. and R. Sowerby, An approximate analysis for studying the deformation mechanics of rate sensitive materials. International Journal of Mechanical Sciences, 1978. **20**(6): p. 361-371.

51. Price, J.W.H. and J.M. Alexander, Specimen geometries predicted by computer model of high deformation forging. International Journal of Mechanical Sciences, 1979. **21**(7): p. 417-430.

52. Tayal, A.K. and R. Natarajan, Extrusion of rate-sensitive materials using a viscoplastic constitutive equation and the finite element method. International Journal of Mechanical Sciences, 1981. **23**(2): p. 89-98.

53. Cheng, J.-H. and N. Kikuchi, A mesh re-zoning technique for finite element simulations of metal forming processes. International Journal for Numerical Methods in Engineering, 1986. **23**(2): p. 219-228.

54. Cheng, J.-H., Automatic adaptive remeshing for finite element simulation of forming processes. International Journal for Numerical Methods in Engineering, 1988. **26**(1): p. 1-18.

55. Petersen, S.B. and P.A.F. Martins, FINITE ELEMENT REMESHING: A METAL FORMING APPROACH FOR QUADRILATERAL MESH GENERATION AND REFINEMENT. International Journal for Numerical Methods in Engineering, 1997. **40**(8): p. 1449-1464.

56. PavanaChand, C. and R. KrishnaKumar, Remeshing issues in the finite element analysis of metal forming problems. Journal of Materials Processing Technology, 1998. **75**(1–3): p. 63-74.

57. Hattangady, N.V., M.S. Shephard, and A.B. Chaudhary, Towards realistic automated 3D modelling of metal forming problems. Engineering with Computers, 1999. **15**(4): p. 356-74.

58. Hamel, V., et al., Finite element modeling of clinch forming with automatic remeshing. Computers & Structures, 2000. **77**(2): p. 185-200.

59. Xing, H.L., S. Wang, and A. Makinouchi, An adaptive mesh h-refinement algorithm for the finite-element modeling of sheet forming. Journal of Materials Processing Technology, 1999. **91**(1–3): p. 183-190.

60. George, P.L., H. Borouchaki, and P. Laug, An efficient algorithm for 3D adaptive meshing. Advances in Engineering Software, 2002. **33**(7–10): p. 377-387.

61. Fernandes, J.L.M. and P.A.F. Martins, All-hexahedral remeshing for the finite element analysis of metal forming processes. Finite Elements in Analysis and Design, 2007. **43**(8): p. 666-679.

62. Donea, J., et al., Arbitrary Lagrangian–Eulerian Methods, in Encyclopedia of Computational Mechanics. 2004, John Wiley & Sons, Ltd.

63. Noh, W.F., CEL: A time-dependent, two-space-dimensional, Coupled Eulerian-Lagrange code, in Methods in Computational Physics. 1964, Academic Press. p. 117-179.

64. Belytschko, T.B. and J.M. Kennedy, COMPUTER MODELS FOR SUBASSEMBLY SIMULATION. Nuclear Engineering and Design, 1978. **49**(1-2): p. 17-38.

65. Hughes, T.J.R., W.K. Liu, and T.K. Zimmermann, Lagrangian-Eulerian finite element formulation for incompressible viscous flows. Computer Methods in Applied Mechanics and Engineering, 1981. **29**(3): p. 329-349.

66. Wing Kam, L. and C. Hsiu Guo. A method of computation for fluid structure interaction. in Symposium on Advances and Trends in Structures and Dynamics, 22-25 Oct. 1984. 1985. UK.

67. Casadei, F., et al., Transient fluid–structure interaction algorithms for large industrial applications. Computer Methods in Applied Mechanics and Engineering, 2001. **190**(24–25): p. 3081-3110.

68. Haber, R.B., A mixed Eulerian-Lagrangian displacement model for large-deformation analysis in solid mechanics. Computer Methods in Applied Mechanics and Engineering, 1984. **43**(3): p. 277-92.

69. Liu, W.K., T. Belytschko, and H. Chang, An arbitrary Lagrangian-Eulerian finite element method for path-dependent materials. Computer Methods in Applied Mechanics and Engineering, 1986. **58**(2): p. 227-45.

70. Schreurs, P.J.G., F.E. Veldpaus, and W.A.M. Brekelmans, Simulation of forming processes, using the arbitrary eulerian-lagrangian formulation. Computer Methods in Applied Mechanics and Engineering, 1986. **58**(1): p. 19-36.

71. Ghosh, S. and N. Kikuchi, An arbitrary Lagrangian-Eulerian finite element method for large deformation analysis of elastic-viscoplastic solids. Computer Methods in Applied Mechanics and Engineering, 1991. **86**(2): p. 127-188.

72. Benson, D.J., An efficient, accurate, simple ale method for nonlinear finite element programs. Computer Methods in Applied Mechanics and Engineering, 1989. **72**(3): p. 305-350.

73. Wang, J. and M.S. Gadala, Formulation and survey of ALE method in nonlinear solid mechanics. Finite Elements in Analysis and Design, 1997. **24**(4): p. 253-269.

74. Gadala, M.S. and J. Wang, A practical procedure for mesh motion in arbitrary Lagrangian-Eulerian method. Engineering with Computers, 1998. **14**(3): p. 223-34.

75. Gadalaa, M.S., M.R. Movahhedy, and J. Wang, On the mesh motion for ALE modeling of metal forming processes. Finite Elements in Analysis and Design, 2002. **38**(5): p. 435-59.

76. Gadala, M.S., Recent trends in ALE formulation and its applications in solid mechanics. Computer Methods in Applied Mechanics and Engineering, 2004. **193**(39-41 SPEC. ISS.): p. 4247-4275.

77. Couch, R., et al. Application of ALE techniques to metal forming simulations. in Proceedings of the 1993 ASME Winter Annual Meeting, November 28, 1993 - December 3, 1993. 1993. New Orleans, LA, USA: Publ by ASME.

78. Gadala, M.S. and J. Wang, ALE formulation and its application in solid mechanics. Computer Methods in Applied Mechanics and Engineering, 1998. **167**(1-2): p. 33-55.

79. Gadala, M.S. and J. Wang, Simulation of metal forming processes with finite element methods. International Journal for Numerical Methods in Engineering, 1999. **44**(10): p. 1397-1428.

80. Olovsson, L., L. Nilsson, and K. Simonsson, An ALE formulation for the solution of two-dimensional metal cutting problems. Computers & Structures, 1999. **72**(4–5): p. 497-507.

81. Aymone, J.L.F., E. Bittencourt, and G.J. Creus, Simulation of 3D metal-forming using an arbitrary Lagrangian–Eulerian finite element method. Journal of Materials Processing Technology, 2001. **110**(2): p. 218-232.

82. Boman, R., et al., Application of the Arbitrary Lagrangian Eulerian formulation to the numerical simulation of cold roll forming process. Journal of Materials Processing Technology, 2006. **177**(1–3): p. 621-625.

83. Davey, K. and M.J. Ward, A practical method for finite element ring rolling simulation using the ALE flow formulation. International Journal of Mechanical Sciences, 2002. **44**(1): p. 165-190.

84. Davey, K. and M.J. Ward, An ALE approach for finite element ring-rolling simulation of profiled rings. Journal of Materials Processing Technology, 2003. **139**(1–3): p. 559-566.

85. Gould, J.E. and Z. Feng, Heat flow model for friction stir welding of aluminum alloys. Journal of Materials Processing and Manufacturing Science, 1998. **7**(2): p. 185-194.

86. Frigaard, Grong, and O.T. Midling, A process model for friction stir welding of age hardening aluminum alloys. Metallurgical and Materials Transactions A: Physical Metallurgy and Materials Science, 2001. **32**(5): p. 1189-1200.

87. Khandkar, M.Z.H., J.A. Khan, and A.P. Reynolds. A thermal model of the friction stir welding process. in 2002 ASME International Mechanical Engineering Congress and Exposition, November 17, 2002 - November 22, 2002. 2002. New Orleans, LA, United states: American Society of Mechanical Engineers.

88. Khandkar, M.Z.H., J.A. Khan, and A.P. Reynolds, Prediction of temperature distribution and thermal history during friction stir welding: input torque based model. Science and Technology of Welding and Joining, 2003. **8**(3): p. 165-174.

89. Chao, Y.J. and X. Qi, Thermal and thermo-mechanical modeling of friction stir welding of aluminum alloy 6061-T6. Journal of Materials Processing and Manufacturing Science, 1998. **7**(2): p. 215-233.

90. Chao, Y.J., X. Qi, and W. Tang, Heat transfer in friction stir welding - Experimental and numerical studies. Journal of Manufacturing Science and Engineering, Transactions of the ASME, 2003. **125**(1): p. 138-145.

91. Song, M. and R. Kovacevic, Thermal modeling of friction stir welding in a moving coordinate system and its validation. International Journal of Machine Tools and Manufacture, 2003. **43**(6): p. 605-615.

92. Schmidt, H., J. Hattel, and J. Wert, An analytical model for the heat generation in friction stir welding. Modelling and Simulation in Materials Science and Engineering, 2004. **12**(1): p. 143-57.

93. Schmidt, H.B. and J.H. Hattel, Thermal modelling of friction stir welding. Scripta Materialia, 2008. **58**(5): p. 332-337.

94. Hilgert, J., et al., Thermal models for bobbin tool friction stir welding. Journal of Materials Processing Technology, 2011. **211**(2): p. 197-204.

95. Ulysse, P., Three-dimensional modeling of the friction stir-welding process. International Journal of Machine Tools and Manufacture, 2002. **42**(14): p. 1549-1557.

96. Colegrove, P.A. and H.R. Shercliff, 3-Dimensional CFD modelling of flow round a threaded friction stir welding tool profile. Journal of Materials Processing Technology, 2005. **169**(2): p. 320-7.

97. Seidel, T.U., The development of a friction stir welding process model using computational fluid dynamics. 2002, University of South Carolina.

98. Medhi, T., et al., Thermal modelling and effect of process parameters in friction stir welding. Materials Today: Proceedings, 2015. **2**(4–5): p. 3178-3187.

99. Sheppard, T. and D.S. Wright, Determination of flow stress: Part 1 constitutive equation for aluminium alloys at elevated temperatures. Metals Technology, 1979. **6**(1): p. 215-223.

100. Zener, C. and J.H. Hollomon, Effect of Strain Rate Upon Plastic Flow of Steel. Journal of Applied Physics, 1944. **15**(1): p. 22-32.

101. Seidel, T.U. and A.P. Reynolds, Two-dimensional friction stir welding process model based on fluid mechanics. Science and Technology of Welding and Joining, 2003. **8**(3): p. 175-183.

102. Colegrove, P.A. and H.R. Shercliff, Experimental and numerical analysis of aluminium alloy 7075-T7351 friction stir welds. Science and Technology of Welding and Joining, 2003. **8**(5): p. 360-368.

103. Colegrove, P.A. and H.R. Shercliff, CFD modelling of friction stir welding of thick plate 7449 aluminium alloy. Science and Technology of Welding and Joining, 2007. **11**(4): p. 429-41.

104. Long, T. and A.P. Reynolds, Parametric studies of friction stir welding by commercial fluid dynamics simulation. Science and Technology of Welding and Joining, 2007. **11**(2): p. 200-8.

105. Nandan, R., G.G. Roy, and T. Debroy, Numerical simulation of three dimensional heat transfer and plastic flow during friction stir welding. Metallurgical and Materials Transactions A: Physical Metallurgy and Materials Science, 2006. **37**(4): p. 1247-1259.

106. Nandan, R., et al., Numerical modelling of 3D plastic flow and heat transfer during friction stir welding of stainless steel. Science and Technology of Welding and Joining, 2006. **11**(5): p. 526-37.

107. Nandan, R., et al., Three-dimensional heat and material flow during friction stir welding of mild steel. Acta Materialia, 2007. **55**(3): p. 883-895.

108. Atharifar, H., L. Dechao, and R. Kovacevic, Numerical and Experimental Investigations on the Loads Carried by the Tool During Friction Stir Welding. Journal of Materials Engineering and Performance, 2009. **18**(4): p. 339-50.

109. Cox, C., et al., Modeling the control of an elevated tool temperature and the affects on axial force during friction stir welding. Materials and Manufacturing Processes, 2010. **25**(11): p. 1278-1282.

110. Aljoaba, S., et al., Modeling the Effects of Coolant Application in Friction Stir Processing on Material Microstructure Using 3D CFD Analysis. Journal of Materials Engineering and Performance, 2012. **21**(7): p. 1141-50.

111. Hasan, A.F., C.J. Bennett, and P.H. Shipway, A numerical comparison of the flow behaviour in Friction Stir Welding (FSW) using unworn and worn tool geometries. Materials & Design, 2015. **87**: p. 1037-1046.

112. Su, H., et al., Numerical modeling for the effect of pin profiles on thermal and material flow characteristics in friction stir welding. Materials & Design, 2015. **77**: p. 114-125.

113. Xu, S., et al., Finite element simulation of material flow in friction stir welding. Science and Technology of Welding and Joining, 2001. **6**(3): p. 191-193.

114. Deng, X. and S. Xu, Two-Dimensional Finite Element Simulation of Material Flow in the Friction Stir Welding Process. Journal of Manufacturing Processes, 2004. **6**(2): p. 125-133.

115. Schmidt, H. and J. Hattel, A local model for the thermomechanical conditions in friction stir welding. Modelling and Simulation in Materials Science and Engineering, 2005. **13**(1): p. 77-93.

116. Assidi, M., et al., Friction model for friction stir welding process simulation: Calibrations from welding experiments. International Journal of Machine Tools and Manufacture, 2010. **50**(2): p. 143-155.

117. van der Stelt, A.A., et al. Comparison of ALE finite element method and adaptive smoothed finite element method for the numerical simulation of friction stir welding. in 14th International Esaform Conference on Material Forming: Esaform 2011, 27-29 April 2011. 2011. USA: American Institute of Physics.

118. Liu, X., S. Lan, and J. Ni, Thermal Mechanical Modeling of the Plunge Stage During Friction-Stir Welding of Dissimilar Al 6061 to TRIP 780 Steel. Journal of Manufacturing Science and Engineering, 2015. **137**(5): p. 051017-051017.

119. Zhang, H.W., Z. Zhang, and J.T. Chen, 3D modeling of material flow in friction stir welding under different process parameters. Journal of Materials Processing Technology, 2007. **183**(1): p. 62-70.

120. Grujicic, M., et al., Fully coupled thermomechanical finite element analysis of material evolution during friction-stir welding of AA5083. Proceedings of the Institution of Mechanical Engineers, Part B (Journal of Engineering Manufacture), 2010. **224**(B4): p. 609-25.

121. Chiumenti, M., et al., Numerical modeling of friction stir welding processes. Computer Methods in Applied Mechanics and Engineering, 2013. **254**: p. 353-369.

122. Pan, W., et al., A new smoothed particle hydrodynamics non-Newtonian model for friction stir welding: Process modeling and simulation of microstructure evolution in a magnesium alloy. International Journal of Plasticity, 2013. **48**: p. 189-204.

123. Grujicic, M., et al., Computational Analysis of Material Flow During Friction Stir Welding of AA5059 Aluminum Alloys. Journal of Materials Engineering and Performance, 2012. **21**(9): p. 1824-40.

124. Neto, D.M. and P. Neto, Numerical modeling of friction stir welding process: a literature review. International Journal of Advanced Manufacturing Technology, 2013. **65**(1-4): p. 115-26.

125. He, X., F. Gu, and A. Ball, A review of numerical analysis of friction stir welding. Progress in Materials Science, 2014. **65**: p. 1-66.

126. Sinnott, R.K., Chemical Engineering Design: Chemical Engineering. 2005: Elsevier Science.

127. Abramowitz, M. and I.A. Stegun, Handbook of Mathematical Functions: With Formulas, Graphs, and Mathematical Tables. 1964: Dover Publications.

128. Versteeg, H.K. and W. Malalasekera, An Introduction to Computational Fluid Dynamics: The Finite Volume Method. 2007: Pearson Education Limited.

129. Zhang, H., et al., Investigation of material flow during friction extrusion process. International Journal of Mechanical Sciences, 2014. **85**: p. 130-141.

130. Zhao, X., et al., Stereo image based motion measurements in fluids: experimental validation and application in friction extrusion. Experimental Mechanics, 2015. **55**(1): p. 177-200.

131. Zhang, H., et al., Heat transfer modeling of the friction extrusion process. Journal of Materials Processing Technology, 2015. **221**: p. 21-30.

132. Li, X., W. Tang, and A.P. Reynolds, Material Flow and Texture in Friction Extruded Wire, in Friction Stir Welding and Processing VII. 2013, John Wiley & Sons, Inc. p. 339-347.

133. Li, X., et al., Strain and texture in friction extrusion of aluminum wire. Journal of Materials Processing Technology, 2016. **229**: p. 191-198.

134. Valberg, H. and T. Malvik, An experimental investigation of the material flow inside the bearing channel in aluminium extrusion. International Journal of Materials and Product Technology, 1994. **9**(4-6): p. 428-463.

135. Mukai, T., K. Ishikawa, and K. Higashi, Influence of strain rate on the mechanical properties in fine-grained aluminum alloys. Materials Science and Engineering: A, 1995. **204**(1–2): p. 12-18.

136. Malas, J.C. and V. Seetharaman, Using material behavior models to develop process control strategies. JOM, 1992. **44**(6): p. 8-13.

137. Balasubrahmanyam, V.V. and Y.V.R.K. Prasad, Hot deformation mechanisms in Ti-5.5Al-1Fe alloy. Journal of Materials Engineering and Performance, 2001. **10**(6): p. 731-9.

138. Lin, Y.C., et al., Constitutive descriptions for hot compressed 2124-T851 aluminum alloy over a wide range of temperature and strain rate. Computational Materials Science, 2010. **50**(1): p. 227-233.

139. Sheppard, T., Extrusion of AA 2024 alloy. Materials Science and Technology, 1993. **9**(5): p. 430-440.

140. Clade, M.P. and T. Sheppard, Extrusion limit diagrams containing structural and topological information for AA 6063 aluminium alloy. Materials Science and Technology, 1993. **9**(4): p. 313-318.

141. Sheppard, T. and A. Jackson, Constitutive equations for use in prediction of flow stress during extrusion of aluminium alloys. Materials Science and Technology, 1997. **13**(3): p. 203-209.

142. Duan, X. and T. Sheppard, The influence of the constitutive equation on the simulation of a hot rolling process. Journal of Materials Processing Technology, 2004. **150**(1–2): p. 100-106.

143. Lesuer, D.R., G.J. Kay, and M.M. LeBlanc. Modeling large strain, high rate deformation in metals. in Modelling the Performance of Engineering Structural Materials II. Proceedings of a Symposium, 4-8 Nov. 2001. 2001. Warrendale, PA, USA: TMS - Miner. Metals & Mater. Soc.

144. Doude, H.R., J.A. Schneider, and A.C. Nunes, Influence of the Tool Shoulder Contact Conditions on the Material Flow During Friction Stir Welding. Metallurgical and Materials Transactions A, 2014. **45**(10): p. 4411-22.

145. Wang, H., P.A. Colegrove, and J.F. dos Santos, Numerical investigation of the tool contact condition during friction stir welding of aerospace aluminium alloy. Computational Materials Science, 2013. **71**: p. 101-108.

146. Chang, C.I., C.J. Lee, and J.C. Huang, Relationship between grain size and Zener–Holloman parameter during friction stir processing in AZ31 Mg alloys. Scripta Materialia, 2004. **51**(6): p. 509-514.

147. Wang, Y.N., et al. Influence from extrusion parameters on high strain rate and low temperature superplasticity of AZ series Mg-based alloys. in THERMEC'2003. International Conference on Processing and Manufacturing of Advanced Materials, 7-11 July 2003. 2003. Switzerland: Trans Tech Publications.

148. Ammouri, A.H., et al., Relating grain size to the Zener–Hollomon parameter for twin-roll-cast AZ31B alloy refined by friction stir processing. Journal of Materials Processing Technology, 2015. **222**: p. 301-306.

149. Duan, X. and T. Sheppard. Influence of forming parameters on the final subgrain size during hot rolling of aluminium alloys. 2002. Elsevier Ltd.

150. Robson, J.D. and L. Campbell, Model for grain evolution during friction stir welding of aluminium alloys. Science and Technology of Welding and Joining, 2010. **15**(2): p. 171-176.

151. Morisada, Y., T. Imaizumi, and H. Fujii, Determination of strain rate in Friction Stir Welding by three-dimensional visualization of material flow using X-ray radiography. Scripta Materialia, 2015. **106**: p. 57-60.

APPENDIX A USER DEFINED FUNCTIONS

Viscosity

The viscosity of AA6061 is implemented by a user defined function. It is a function of temperature and strain rate. The strain rate is not smaller than 10^{-4} /s and the viscosity is not larger than 10^{12} /s. The user defined function is written in C and to be complied by FLUENT.

```
# include "udf.h"
DEFINE_PROPERTY(visco6061, c, t)
{
real visco;
real tp;
real s_rate = C_STRAIN_RATE_MAG(c,t);
real a;
real n;
real q;
real r;
real b;
real z;
a = 4.5e-8;
n = 3.55;
q = 145000.0;
```

```
r = 8.314;
b=exp(19.3);
tp = C_T(c, t);
if( s_rate <= 1.0e-4) s_rate = 1.0e-4;
z = s_rate * exp(q / (r * tp));
visco=1 / (3 * a * s_rate) * log(pow((z / b),1.0 / n)+pow((pow((z / b), 2.0 / n)+1), 0.5));
if(visco >=1.0e12)  visco=1.0e12;
return visco;
}
```

Rotating Speed

The rotating speed of the die increases from zero to 300 rpm and the increase is controlled by a user defined function as follows.

The following is for x-direction.

```
# include "udf.h"
DEFINE_PROFILE(v_x, t,i)
{
face_t f;
real x[ND_ND];
real xx, yy,r;
real theta;
real tm;
real w;
real vx;
```

```
tm=CURRENT_TIME;
if (tm>=0 && tm<=4.7)
w=0;
else if (tm>4.7 && tm<8.7)
w=(tm-4.7)*7.855*0.6;
else
w=31.42*0.6;
vx=0;
begin_f_loop(f,t)
{
F_CENTROID(x,f,t);
xx=x[0];
yy=x[1];
r=sqrt(xx*xx+yy*yy);
if (xx!=0) theta=atan(fabs(yy)/fabs(xx));
if(yy>0 && xx!=0)
vx=-w*r*sin(theta);
else if(yy>0&&xx==0)
vx=-w*r;
else if (yy==0)
vx=0;
else if(yy<0 && xx!=0)
vx=w*r*sin(theta);
```

```
else
vx=w*r;
F_PROFILE(f,t,i)=vx;
}
end_f_loop(f,t)
}
```

The following is for y-direction.

```
# include "udf.h"
DEFINE_PROFILE(v_y, t,i)
{
face_t f;
real x[ND_ND];
real xx, yy,r;
real theta;
real tm;
real w;
real vy;
vy=0;
tm=CURRENT_TIME;
if (tm>=0 && tm<=4.7)
w=0;
else if (tm>4.7 && tm<8.7)
```

```
w=(tm-4.7)*7.855*0.6;
else
w=31.42*0.6;
begin_f_loop(f,t)
{
F_CENTROID(x,f,t);
xx=x[0];
yy=x[1];
r=sqrt(xx*xx+yy*yy);
if (xx!=0) theta=atan(fabs(yy)/fabs(xx));
if(xx>0)
vy=w*r*cos(theta);
else if (xx==0)
vy=0;
else
vy=-w*r*cos(theta);
F_PROFILE(f,t,i)=vy;
}
end_f_loop(f,t)
}
```

Moving Mesh

The reduction of the volume of the fluid computational domain is by moving the domain and the dynamic meshing. The user defined function for the motion is as follows.

```
#include"udf.h"


DEFINE_CG_MOTION(dyn,dt,cg_vel,cg_omega,time,dtime)
{
cg_vel[0]=0;
cg_vel[1]=0;
NV_S(cg_omega,=,0.0);
if(time >10 && time <=24.5)
cg_vel[2]=-1.12e-4;
else if(time>24.5 && time<28)
cg_vel[2]=-1.85e-5;
else
cg_vel[2]=0;
}
```

Simulation of the Gap

The gap between the chamber wall and the aluminum alloy sample is simulated by changing the conductivity of the gap region. The following is the user defined function.

```
# include "udf.h"
DEFINE_PROPERTY(cond,c,t)
{
real tm;
real tp;
real cond;
```

```
real h1;
real h2;
real x[ND_ND];
real xx,yy,rr,zz;
tm=CURRENT_TIME;
tp=C_T(c,t);
F_CENTROID(x,c,t);
xx=x[0];
yy=x[1];
zz=x[2];
rr=sqrt(xx*xx+yy*yy);
if (rr>=0.01275)
{if(tm>0 && tm<5)
cond=2;
else if( tm>=5 && tm<=10)
{
h1=0.019+0.00204*(tm-5);
h2=0.018-0.0036*(tm-5);
if(zz>h2 && zz<h1)
cond=115+0.1594*tp;
else
cond=2;
}
```

```
else
cond=115+0.1594*tp;
}
else
cond=35;
return cond;
}
```

Heat Source

The heat generation rate in the volume heating layer is linear along both radial and vertical directions. The mechanical power curve correlated to the heat generation rate is fitted by polynomials. The user defined function for it is as follows

```
#include "udf.h"
DEFINE_SOURCE(qua,c,t,ds,eqn)
{
real x[ND_ND];
real xx;
real yy;
real zz;
real r;
real h;
real w;
real source;
real tm;
```

```
real alpha;
real dd;

real a1, b1,c1,d1;
real a2, b2,c2,d2,e2;
real a3, b3,c3,d3;
real a4,b4,c4,d4;
real t1,t2,t3,t4,t5;
alpha=1;
a1=0.0816;
b1=0.0159;
c1=-0.3628;
d1=0.1097;
a2=-0.1429;
b2=3.2986;
c2=-28.03;
d2=104.49;
e2=-139.71;
a3=-0.001;
b3=0.064;
c3=-1.4098;
d3=14.183;
a4=-0.0268;
```

```
b4=2.5283;
c4=-79.602;
d4=837.77;
t1=0;
t2=4;
t3=7.5;
t4=27.7;
t5=31;
tm=CURRENT_TIME;
F_CENTROID(x,c,t);
xx=x[0];
yy=x[1];
zz=x[2];
r=sqrt(xx*xx+yy*yy);
if(tm>=0 && tm<=10)
dd=0;
else if(tm >10 && tm <=24.5)
dd=(tm-10)*1.12e-4;
else
dd=1.624e-3;
h=zz-0.015+dd;
if(tm>t1 && tm<=t2)
{
```

```
w=(a1*pow(tm,3)+b1*pow(tm,2)+c1*pow(tm,1)+d1)*1000;
if(w<=0) w=0;
}
else if ( tm> t2 && tm <= t3)
w=(a2*pow(tm,4)+b2*pow(tm,3)+c2*pow(tm,2)+d2*pow(tm,1)+e2)*1000;
else if( tm> t3 && tm<=t4)
w=(a3*pow(tm,3)+b3*pow(tm,2)+c3*pow(tm,1)+d3)*1000;
else if( tm> t4 && tm<=t5)
w=(a4*pow(tm,3)+b4*pow(tm,2)+c4*pow(tm,1)+d4)*1000;
else
w=0;
if( h>0)
source = alpha*w*r*h*3/98125*1e15;
else
source=0;
return source;
}
```